Karlsruher Institut für Technologie

IEKP-KA/2011-4

Untersuchung der Einzel-Top-Quark-Produktion mit dem CMS-Experiment

Jens Hansen

DIPLOMARBEIT

VON

JENS HANSEN

An der Fakultät für Physik
Institut für Experimentelle Kernphysik

Referent:	Prof. Dr. T. Müller
Korreferent:	Prof. Dr. M. Feindt

15. März 2012

Zusammenfassung

Hätte der verzweifelte Heinrich Faust aus der gleichnamigen Tragödie Johann Wolfgang von Goethes in der Teilchenphysik geforscht, wäre er wohl seinem Wunsch, zu erkennen *"Was die Welt im innersten zusammenhält"*, auch ohne die Kunst der Magie sehr nahe gewesen. Er wäre zumindest nicht der erste Mensch gewesen, der sich mit dem Erforschen der kleinsten Bausteine beschäftigt hätte. Bereits der Grieche Demokrit prägte den Begriff der unteilbaren kleinsten Einheit (*atomos*) im fünften Jahrhundert vor Christus. Das letzte Jahrhundert der Neuzeit brachte dann die nötigen technischen Fortschritte um selbst das als "unteilbar" postulierte Atom zu spalten. Mit den heutigen experimentellen Möglichkeiten stößt die Menschheit das Tor zu Dimensionen auf, die es ermöglichen nicht nur die Bestandteile der Welt sondern des ganzen Universums zu erklären.

Die Experimente, die typischerweise in der Teilchenphysik zur Erforschung von Materie und Kräften angewendet werden, basieren auf den von Ernest Rutherford erstmals 1909 durchgeführten Streuexperimenten [1]. In heutiger Zeit verwendet man häufig Collider-Experimente an Stelle von Fixed-target-Experimenten. Am derzeit größten teilchenphysikalischen Experiment, dem Large Hadron Collider (LHC) am CERN, werden Protonen aufeinander geschossen und die Fragmente der Kollisionen mit Detektoren aufgezeichnet und ausgewertet. Ziel dieser Untersuchungen ist es, das Standardmodell der Teilchenphysik zu testen und darüber hinaus weitere Teilchen oder Phänomene zu entdecken.

Seit den 1960er Jahren bildet das Standardmodell der Teilchenphysik die theoretische Grundlage für die Erklärung von Elementarteilchen und fundamentalen Wechselwirkungen. Die Beschreibung der starken, der schwachen und der elektromagnetischen Kraft ist im Rahmen einer Quantenfeldtheorie gelungen und postuliert a priori Charakteristiken von Teilchen und Natur, die überprüft und gemessen werden können. Zu diesen Teilchen gehören die Eichbosonen, die als Austauschteilchen Kräfte vermitteln. Eine Vermessung der Zerfallsbreite des Z-Bosons bedingt drei Generationen mit jeweils einem (leichten) Neutrino und einem geladenen Lepton. Parallel dazu sind jeweils zwei Quarks, aufgeteilt in drei Generationen, gefunden worden.

Das zuletzt entdeckte Teilchen des Standardmodells ist das Top-Quark, das 1995 am Tevatron-Beschleuniger bei einer Schwerpunktenergie von $s = \sqrt{1.8}$ TeV erzeugt und von den Experimenten CDF und DØ nachgewiesen wurde [2, 3]. Mit einer Masse von $m_t = (173.2 \pm 0.9)$ GeV/c^2 [4] ist es das mit Abstand schwerste

Elementarteilchen. Die hohe Masse führt zu einer so kurzen Lebensdauer des Top-Quarks, dass es keine gebundenen Zustände eingehen kann und fast instantan in ein W-Boson und ein b-Quark zerfällt. Top-Quarks werden bevorzugt über die starke Wechselwirkung in Paaren erzeugt, können jedoch ebenfalls einzeln über die schwache Wechselwirkung produziert werden. Letzt genannter Produktionsprozess ist von den Experimenten CDF und DØ bei einer Schwerpunktenergie von $s = \sqrt{1.96}$ TeV 2009 nachgewiesen worden [5, 6]. Die Einzel-Top-Quark Produktion erlaubt die direkte Bestimmung des CKM-Matrix-Elementes $|V_{tb}|$ und lässt damit Rückschlüsse auf die Existenz einer möglichen vierten Generation von Quarks zu.

Die elektroschwache Produktion einzelner Top-Quarks kann in drei Mechanismen unterschieden werden: t-Kanal, s-Kanal und assoziierter tW-Produktion. Von diesen drei Erzeugungsprozessen hat der t-Kanal den größten Wirkungsquerschnitt am LHC und ist somit der erfolgversprechenste Kanal zur Beobachtung einzelner Top-Quarks. In dieser Diplomarbeit wird die Messung des Wirkungsquerschnittes dieses Kanals und die Bestimmung des CKM-Matrix-Elements $|V_{tb}|$ vorgestellt. Die dafür verwendeten Daten wurden mit dem CMS Experiment in pp-Kollisionen bei einer Schwerpunktenergie von $s = \sqrt{7}$ TeV aufgenommen. Im speziellen wurden nur solche Ereignisse betrachtet, bei denen das Top-Quark gemäß der Zerfallskette $t \to Wb \to e\nu b$ zerfällt und somit ein isoliertes Elektron im Endzustand beinhalten. Des weiteren zeichnen sich die Ereignisse durch einen Jet aus, der von einem in Vorwärtsrichtung gestreuten leichten Quark stammt, durch fehlende transversale Energie (MET), auf Grund des nicht detektierbaren Neutrinos aus dem W-Boson Zerfall und durch mindestens ein b-Quark Jet. Ausgehend von der Tatsache, dass Quarks nicht als freie Teilchen existieren können, bildet ein Teilchenbündel, dessen Anordnung eine kegelförmige, vom Interaktionspunkt der Kollision ausgehende, Struktur bildet, ein Objekt, das als Jet bezeichnet wird. Kann man einem Jet durch Anwendung eines Algorithmus (b tagging) die Zuordnung zu einem b-Quark nachweisen, wird dieser Jet als b-Quark Jet bezeichnet.

Für die Untersuchungen wurden erstmals Signal-Ereignisse verwendet, die mit dem Monte-Carlo Generator POWHEG simuliert worden sind. Dieser stellt eine Berechnung in nächstführende Ordnung (NLO) bereit. Um die selektierten Datenereignisse auswerten zu können wurden auch Simulationen von Untergrundprozessen betrachtet. Dazu gehören insbesondere die Vektorboson-Produktion und Top-Quark-Paar-Produktion mit großen Wirkungsquerschnitten und ähnlichem kinematischen Verhalten wie die Signalereignisse. Ein großer Beitrag von QCD-Multi-Jet-Ereignissen kann durch einen Selektionsschnitt in der transversalen fehlenden Energie (MET) reduziert werden. Die Modellierung dieses Untergrunds wird nicht aus simulierten Ereignissen gewonnen, sondern eine Selektion mit einem invertierten Isolationsschnitt des Elektrons auf Datenereignissen stellt die Ereignisse bereit. Ein Fit an die selektierten Daten und den bekannten Untergrundereignissen in der MET Verteilung lässt eine quantitative Approximation dieses Untergrundprozesses zu.

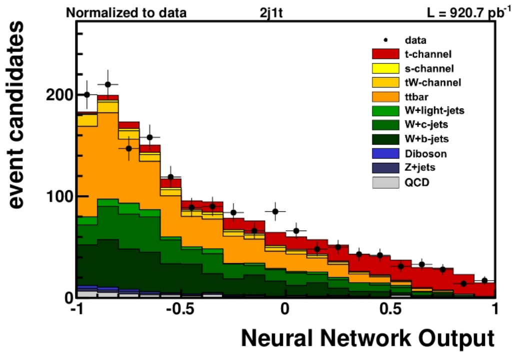

Abbildung 0.1.: Ausgabe des Neuronalen Netzwerkes im signalangereicherten Analysekanal mit zwei Jets. Signalereignisse sind in rot dargestellt und tendieren zu hohen Diskriminatorwerten. Untergrundereignisse haben vorzugsweise einen kleinen Ausgabewert.

Innerhalb der Selektion wird zwischen sechs Analysekanälen unterschieden. Das größte Signal-zu-Untergrund-Verhältnis ($S/B \sim 18\%$) ist im Analysekanal mit einem b-Quark Jet und einem weiteren Jet erreicht (2 Jets mit 1 b-tag Jet; 2j1t). Die Selektion von einem b-Quark Jet und zwei weiteren Jets (3j1t) wird ebenfalls als Analysekanal mit angereicherten Signalereignissen ($S/B \sim 7\%$) bezeichnet. Desweiteren gibt es zwei Analysekanäle, in denen Ereignisse mit zwei bzw. drei Jets selektiert werden, die aber explizit keine b-Quark Jets sind (2j0t und 3j0t). Diese Selektion ermöglicht eine Auswahl von W+Jets angereicherten Ereignissen. Im Falle von zwei bzw. drei b-Quark Jets werden Analysekanäle ausgewählt, die vom Untergrund der Top-Quark-Paar-Produktion dominiert sind (2j2t und 3j2t). Die vier Analysekanäle mit vermehrten Untergrundereignissen sollen helfen die Untergrundraten zu kontrollieren.

Die Messung des Wirkungsquerschnitts der Einzel-Top-Quark-Produktion wird mit Hilfe einer multivariaten Analysemethode durchgeführt. Dazu lernt ein Neuronales Netzwerk die Verteilungen für Signal- und Untergrundprozesse in verschiedenen kinematischen Variablen. Eine beliebige Anzahl an Eingabevariablen wird durch Verknüpfungen, die mit einem Gewicht versehen sind, auf einen Ausgabewert zwischen -1 und $+1$ reduziert. Der Algorithmus eines Neuronalen Netzwerkes passt während des Trainingprozesses die Gewichte der Verknüpfung zwischen den Neuronen so an, dass Untergrundereignisse einen kleinen Ausgabewert und Signalereignisse einen großen Ausgabewert erhalten. Nach dem Training kann die Ausgabe als Diskriminator zwischen Signal- und Untergrundereignissen interpretiert werden und das Netzwerk auf selektierte Daten angewendet werden. Die Ausgabe für den Analysekanal mit dem höchsten Signalanteil ist in Fig. 0.1 gezeigt.

Für die statistische Auswertung wird eine Methode basierend auf dem Bayes'schen Wahrscheinlichkeitsbegriff verwendet. Mit dem Statistikwerkzeug THETA [7] wird

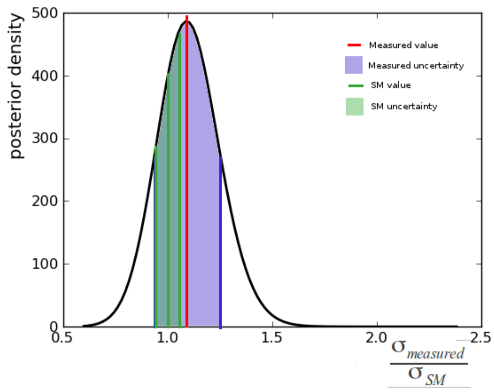

Abbildung 0.2.: Die posterior-Verteilung von β_1 mit $\pm 1\sigma$ Konfidentsintervallen (blau). In grün ist die Standardmodellvorhersage und deren Unsicherheit gekennzeichnet.

eine statistische Anpassungsmethode an alle sechs Netzwerkausgaben aus den jeweiligen Analysekanälen durchgeführt. Als freier Parameter dient $\beta_1 = \frac{\nu}{\nu^{\text{exp}}}$ mit der geschätzten Anzahl der Ereignisse ν und der erwarteten Anzahl der Ereignisse ν^{exp} in jedem Fitsektor. Ein Wert für $\beta_1 = 1$ repräsentiert die Standardmodelerwartung. Zusätzlich betrachtet die statistische Auswertung systematische Unsicherheiten indem Nuisance-Parameter für jede Art von Unsicherheit eingeführt werden. Für einen Datensatz von $\mathcal{L} = 920.7\,\text{pb}^{-1}$ ergibt sich ein Wert von:

$$\beta_1 = 1.0935^{+0.1642}_{-0.1346}\,. \tag{0.1}$$

Die posterior-Verteilung von β_1 wird in Fig. 0.2 gezeigt. Damit kann für den Wirkungsquerschnitt der Einzel-Top-Quark-Produktion im t-Kanal folgendes Ergebnis berechnet werden.

$$\sigma_{\text{measured}} = \sigma_{\text{theory}} \cdot \beta_1 = 70.64^{+10.60}_{-8.69}\,\text{pb}\,. \tag{0.2}$$

Innerhalb der systematischen und statistischen Unsicherheiten wird die Standardmodellvorhersage von $\sigma_{\text{theory}} = 64.6^{+3.5}_{-3.2}\,\text{pb}$ bestätigt. Unter der Vorraussetzung, dass die Matrix-Elemente $|V_{td}|$ und $|V_{ts}|$ viel kleiner sind als $|V_{tb}|$, kann $|V_{tb}|^2$ über das Verhältnis von gemessenem und theoretischem Wirkungsquerschnitt berechnet werden:

$$|V_{tb}|^2 = \frac{\sigma_{\text{measured}}}{\sigma_{\text{theory}}} = 1.09^{+0.17}_{-0.14} \tag{0.3}$$

Die Unsicherheit auf $|V_{tb}|$ ergibt sich aus dem Gaußschen Fehlerfortpflanzunsgesetz mit den Unsicherheiten auf den gemessenen und theoretischen Wirkungsquerschnitt.

Study of Single top quark Production at the CMS Experiment

DIPLOMA THESIS

OF

JENS HANSEN

At the Department of Physics
Institut für Experimentelle Kernphysik

Advisor:	Prof. Dr. T. Müller
Second advisor:	Prof. Dr. M. Feindt

March 15, 2012

Contents

Introduction **5**

1. Theory **7**
- 1.1. Standard Model of Particle Physics . . . 7
- 1.2. Top Quark Physics . . . 11

2. Experiment **19**
- 2.1. Large Hadron Collider . . . 19
- 2.2. Compact Muon Solenoid (CMS) . . . 21

3. Generation, Simulation and Reconstruction of Single Top Quark Production **31**
- 3.1. Generation of Events . . . 31
- 3.2. Monte Carlo Generators . . . 33
- 3.3. Detector Simulation . . . 35
- 3.4. Signal Modeling . . . 35
- 3.5. Reconstruction of Events . . . 35
  - 3.5.1. *b* Tagging . . . 42

4. Event Selection **47**
- 4.1. Background Processes . . . 47
  - 4.1.1. Top Quark Production as Background . . . 47
  - 4.1.2. Vector Boson Production . . . 49
  - 4.1.3. Diboson Production . . . 51
  - 4.1.4. QCD Multijet Production . . . 51
- 4.2. Analyzed Data Sample . . . 52
- 4.3. Event Selection . . . 54
  - 4.3.1. Trigger . . . 55
  - 4.3.2. Primary Vertex (PV) . . . 56
  - 4.3.3. Electron Selection . . . 56
  - 4.3.4. Jet Selection . . . 57
  - 4.3.5. Missing Transverse Energy Cut . . . 57
  - 4.3.6. *b* Tagging . . . 57
  - 4.3.7. QCD Estimation from Data . . . 57
- 4.4. Corrections to Monte Carlo Events . . . 61
  - 4.4.1. Pile-up Reweighting . . . 61
  - 4.4.2. Simulation of Triggers . . . 61

4.4.3. Jet Energy Resolution . . . 62
4.4.4. b Tagging Scale Factors and Efficiency . . . 62
4.4.5. Event Yield . . . 64
4.5. Top Quark Reconstruction . . . 64

5. Neural Network Analysis 67
5.1. Neural Networks . . . 67
5.2. NeuroBayes . . . 67
5.3. Training . . . 69
5.4. Preprocessing . . . 70
5.5. Input Variables . . . 70
5.5.1. Light Quark η . . . 72
5.5.2. Reconstructed Top Quark Mass $M_{l\nu b}$ . . . 72
5.5.3. Invariant Dijet Mass . . . 73
5.5.4. Polarization Variable $\cos\Theta$ . . . 73
5.5.5. Transverse W Boson Mass . . . 73
5.5.6. Scalar Sum of Transverse Energies H_{T} . . . 74
5.5.7. Angle difference between hardest jet and MET $\Delta\phi_{\mathrm{jet1,MET}}$ . . 74
5.6. Training Results . . . 78

6. Signal Extraction and Cross Section Measurement 83
6.1. Statistical Method . . . 83
6.2. Systematic Uncertainties . . . 84
6.2.1. Jet Energy Resolution (JER) . . . 86
6.2.2. Jet Energy Scale (JES) . . . 86
6.2.3. b Tagging Scale Factor . . . 86
6.2.4. Factorization and Renormalization Scale Uncertainty . . . 87
6.2.5. Trigger Turn-on Uncertainty . . . 87
6.2.6. Background Normalization . . . 88
6.2.7. Luminosity . . . 90
6.2.8. PDF and Matching Threshold Uncertainty . . . 90
6.3. Results . . . 90
6.3.1. Cross Section . . . 91
6.3.2. CKM Matrix Element V_{tb} . . . 92

Summary and Outlook 95

A. Input Variables 2-Jet Network 99

B. Input Variables 3-Jet Network 105

List of Figures 115

List of Tables 117

Bibliography **119**

Introduction

Since two years the Large Hadron Collider (LHC) accelerates and collides protons with such a success that even the most optimistic predictions have been beaten. With a center-of-mass energy of $\sqrt{s} = 7\,\text{TeV}$, particle physics studies have reached a new energy level. The Compact Muon Solonoid (CMS) detector records data with great performance and accuracy. The large amount of recorded data allows a precise measurement of Standard Model (SM) predictions at an energy, which has never been achieved before.

The SM, introduced in the 1960s, describes the fundamental modules of matter and its interactions with astonishing precision. It includes the three fundamental forces, namely the strong, the weak and the electromagnetic force and characterizes the gauge bosons, which act as mediators. The SM predicts twelve fermions, grouped into six leptons and six quarks. The quarks act via all three forces, while the leptons cannot act via the strong force. In 1995 the Tevatron collider discovered the top quark, which is the heaviest fermion in the SM [2, 3]. The most precise measurement of the top quark mass leads to a value of $m_t = (173.2 \pm 0.9)$ GeV/c^2 [4]. Due to the large mass, the life time of the top quark is so short, that no bound states with other quarks are possible. With a mass close to the scale of electroweak symmetry breaking the top quark is predestined to test the SM at high energies and to search for hints of new physics.

The dominant production channel for top quarks is the pair production. Beside that, the electroweak production of single top quarks has been discovered in 2009 by the CDF and DØ experiments [5, 6]. The electroweak production of single top quarks allows a direct measurement of the CKM matrix element V_{tb} due to the Wtb vertex in the Feynman diagrams of these processes. The V_{tb} value is an important input to several Beyond Standard Model theories, which assumes a fourth generation of matter. A precise measurement of V_{tb} can exclude or indirectly detect such new physics. Since the top quark cannot form any bound states with other particles the spin information of the top quark is directly transmitted to its decay products. Therewith, a test of the V-A structure of the W boson coupling is possible.

There are three electroweak single top quark production modes in the SM. The t-channel, the s-channel and the associated production (tW). This analysis focuses on the t-channel production mode, which has the largest cross section among the three channels. In addition, only those events are taken into account, which contain an isolated electron from the decay chain $t \to Wb \to e\nu b$.

A measurement with a muon instead of an electron has been published in [8] and determined a cross section for the single top quark t-channel production of $\sigma_\mu = 83.6 \pm 29.8\,(\text{sys.+stat.}) \pm 3.3\,(\text{lumi.})\,\text{pb}$. For this analysis a selection requiring missing transverse energy and one isolated electron is applied. For a subsequent estimation of signal and background events the analysis contains six channels, differing in the number of selected jets and the number of b tagged jets.

This analysis contains a Neural Network based signal cross section extraction. The combination of several kinematic variables increases the discrimination power between signal and background events compared to a single separating variable. The trained Neural Network is applied on data events, recorded with the CMS detector in pp collisions during 2011. The integrated luminosity of the evaluated data set is $\mathcal{L} = 920.7\,\text{pb}^{-1}$. A statistical determination of the single top quark t-channel cross section with systematic and statistical uncertainties is done with a Bayesian approach.

In the first chapter the theory of the SM is introduced containing a detailed description of the production and properties of the top quark. In the second chapter the Large Hadron Collider and the CMS detector are presented. Chapter three contains the description of the simulation of events, the simulation of the detector and the reconstruction of objects in each event. The event selection applied to increase the signal over background ratio is introduced in chapter four. The Neural Network approach is explained in the fifth chapter. Finally the Bayesian method to extract the signal cross section and to describe the matrix element V_{tb} is given in the last chapter.

1. Theory

1.1. Standard Model of Particle Physics

The standard model of elementary particles (SM) describes the interactions of three elementary forces, the strong nuclear force, the weak nuclear force and the electromagnetic force. The forth known elementary force is gravitation, which is described by the theory of General Relativity [9]. Up to these days, no combination of all four forces to a general overarching theory could be achieved.

The great success of the SM is based on the connection of quantum field theory and special relativity. The dynamics of a system of particles is described via a function called Lagrangian. The interactions of particles are the results of local symmetries, so called gauge symmetries: $SU(3)_C \times SU(2)_L \times U(1)_Y$. Based on Noether's theorem [10] each symmetry leads to a conserved quantity. The gauge symmetries conserve the quantities color charge (C), weak isospin (L) and weak hyper charge (Y). Each of these quantities yields to a quantum number for particles. A fourth quantum number called spin splits the constituents of the SM into two sets of particles. Particles with half integer spin form the group of matter constituents, called fermions. In contrast the particles which carry an integer spin are called bosons and act as mediators for the interactions between particles.

Fermions

Fermions are subject to the Pauli principle, which forbids that two fermions occupy the same state, namely the same set of quantum numbers. The SM has two classes of fermions, quarks and leptons. Both classes have six constituents, which can be assigned to three generations. Tab. 1.1 shows the hierarchy and properties of all fermions in the SM. An up and a down type quark in the same generation form a ispin dublett. Whereas, quarks with the same electric charge and same weak isospin differ only in the mass to each other. Higher generation imply a higher mass. This regularity is valid for leptons as well. Furthermore, the neutrinos are massless in the SM, however experiments in the past have shown that neutrinos oscillate between flavors, which indicates that they have non vanishing masses [11]. Neutrinos interact only via the weak force, while charged leptons can take also part in the electromagnetic interaction. Quarks are the only fermions with color charge, hence only they take part in strong interactions. Up quarks and down quarks form protons (uud) and neutrons (udd), which for their part form, together with electrons, atoms and therewith structures of matter. The electron neutrino plays an important role in the decay of atoms. Via the weak nuclear force a neutron transforms into a proton while emitting an electron and an electron anti-neutrino. All four particles of the first generation influence the 'every-day-life', the other two generations particles are unstable and decay in lower generation particles, hence they have to be produced in experiments to study nature.

Table 1.1.: The fermions in the Standard Model, their hierarchy and properties. They are grouped pairwise in three generations forming isospin doublets. The down type quarks are the weak interaction eigenstates, which differ from the mass eigenstates.

Fermions	Generation 1	2	3	Electric Charge [e]	Weak Isospin	Color
Quarks	u	c	t	$+2/3$	$+1/2$	red green blue
	d'	s'	b'	$-1/3$	$-1/2$	
Leptons	ν_e	ν_μ	ν_τ	0	$+1/2$	–
	e	μ	τ	-1	$-1/2$	

Bosons

The members of the second class of particles in the SM are the gauge bosons. They are the mediators of the forces. The photon (γ) is a massless particle and couples to electric charge, hence it mediates the electromagnetic force. The other massless boson of the SM is the gluon. It carries both a color charge and an anti-color charge. With the three different colors of the SM (red, green and blue), there are eight physically different possibilities for gluons. The gauge bosons of the weak interaction are the Z and W bosons. Both are massive particles (see Tab. 1.2), their difference is the electric charge. While W bosons exist with electric charge (W^+, W^-), the Z boson is an electrically neutral particle. All discovered gauge bosons have a spin of 1. An overview of all gauge bosons in the SM with their electric charge and mass is given in Tab. 1.2 [12].

Table 1.2.: Overview of the gauge bosons in the standard model with their electric charge and mass [12]. Electric charge is given in units of the elementary charge e.

Name	Symbol	Force	Electric Charge [e]	Mass [GeV/c^2]
Photon	γ	electromagnetic	0	0
W bosons	$W^\pm$	weak	± 1	80.4
Z boson	Z	weak	0	91.2
Gluon	g	strong	0	0

Higgs Mechanism

A fundamental conflict of the SM is the fact that W and Z bosons are massive. By construction of the theory, a mass term for bosons in the Lagrangian would violate local gauge symmetry. Consider that symmetry as so important, theorist have developed the Higgs mechanism. The introduction provides mass terms for gauge bosons and fermions and is reached via the spontaneous symmetry breaking. A new field, called Higgs field, interacts with other fields and with itself and gives gauge bosons and fermions their mass. For global symmetries, symmetry breaking would lead to massless Goldstone bosons, where for local symmetry breaking the mass for these Goldstone bosons can be canceled with mathematical gauge transformations. Instead the Goldstone modes of the Higgs field leads to longitudinal polarization states of gauge bosons and generate thereby their mass. The photon however has only transverse polarization states and stays massless. Hence one degree of freedom of the Higgs field can be observed as a massive particle, the Higgs boson. The detection of the Higgs boson is still unsuccessful and its discovery is one of the main goals for current collider experiments. It's observation would be the missing piece in the puzzle of massive bosons in the SM. The last measurement of the Higgs boson mass is done in [13], which excludes a mass region for its present in the range $127 - 600\,\mathrm{GeV}$ at 95% confident level.

Also the masses of fermions can be introduced by the Higgs fields. Via so called Yukawa interactions the quarks interact with the Higgs field. This leads to the situation, that the mass eigenstates of the quarks are not the same as the eigenstates of the weak interaction. The relation between both eigenstates is given by the so called Cabbibo-Kobayashi-Maskawa (CKM) matrix [14, 15]:

$$\begin{pmatrix} d' \\ s' \\ b' \end{pmatrix} = \begin{pmatrix} V_{ud} & V_{us} & V_{ub} \\ V_{cd} & V_{cs} & V_{cb} \\ V_{td} & V_{ts} & V_{tb} \end{pmatrix} \begin{pmatrix} d \\ s \\ b \end{pmatrix} \tag{1.1}$$

In case of three generations in the SM the CKM matrix is a unitary 3×3 matrix and transforms the mass eigenstates of the down type quarks (d, s, b) into their weak eigenstates (d', s', b'). To validate the SM, and hence the unitarity, many measurements of the CKM matrix elements have been done by different experiments and a global fit to all data under SM constraints has been performed. In Eq. (1.2) the magnitudes of the matrix elements are shown [12].

$$V_{CKM} = \begin{pmatrix} 0.97428 \pm 0.00015 & 0.2253 \pm 0.0007 & \left(3.47^{+0.16}_{-0.12}\right) \cdot 10^{-3} \\ 0.2252 \pm 0.0007 & 0.97345^{+0.00015}_{-0.00016} & \left(4.10^{+0.11}_{-0.07}\right) \cdot 10^{-2} \\ \left(8.62^{+0.26}_{-0.20}\right) \cdot 10^{-3} & \left(4.03^{+0.11}_{-0.07}\right) \cdot 10^{-2} & 0.999152^{+0.000030}_{-0.000045} \end{pmatrix} \tag{1.2}$$

Because the diagonal matrix elements are close to one, transitions between quarks in the same generation are favored. Transitions between quarks of different generations are 'CKM suppressed' due to the small magnitude of these elements. Indirect measurements of $|V_{tb}| \approx 1$ suggest that the top quark decays almost exclusively into a b quark.

Hard scattering

In order to observe interactions between elementary particles elaborated experiments are needed to study particle collisions at high energies. A measure describing the rate for a certain process to happen is called cross section. It is usually given in the unit barn, where one barn is $10^{-28}\mathrm{m}^{-2}$. Fermi's Golden Rule gives the mathematical background for the calculation of the transition rate between an initial state and a final state of a quantum mechanical system. It mainly evaluates the Lorentz-invariant matrix element $\mathcal{M}$ of a particular process and integrates over the phase space of the final state configuration. Mathematically the description of transitions between different quantum states is done by perturbation theory, where the coupling strength α_i is treated as perturbation. The series should be dominated by the leading-order (LO) term. The matrix element $\mathcal{M}$ contains information about the kinematics of the incoming and outgoing particles, the exchanged gauge bosons and about the interaction between both. Every mathematical term of the interaction can be represented by a certain graphical symbol. Combining these graphical symbols leads to so-called Feynman diagrams, which illustrate complicated physical processes in simple schematic pictures. In Fig. 1.1 some diagrams are shown exemplarily.

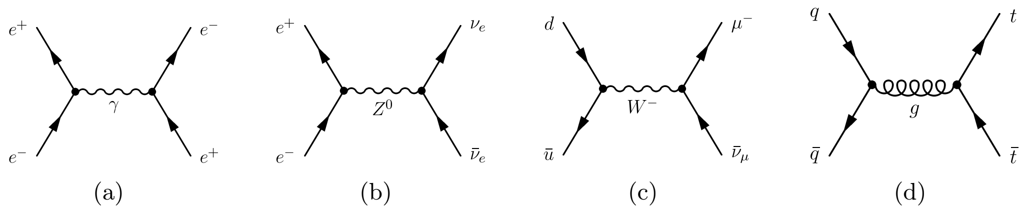

Figure 1.1.: Each diagram illustrates the annihilation of fermions into a virtual gauge boson and a subsequent fermion pair-production. (a) shows the electron-positron annihilation into a photon and represents the electromagnetic force. Process (b) has the same initial state but the weak force is mediated via a Z boson. In (c) two quarks scatter via the charged weak force and in (d) two quarks annihilate via the strong force.

Protons are not elementary particles, as they are a composition of quarks and gluons, the so-called partons. A proton is a complex of two up quarks and one down quark. These are called valence quarks and they are bound inside the proton through virtual gluon exchange. Furthermore, gluons can split into quark-antiquark pairs, the so-called sea quarks. Each parton i carries a fraction x_i of the entire momentum of the proton. For each parton this momentum is described by a parton distribution function (PDF) $f_i\left(x_i, \mu^2\right)$. This function depends on the scale ($\mu = Q^2$) of the momentum transfer of the interaction and can not be calculated analytically but can be derived from fits to measured processes like deep inelastic scattering (DIS) or Drell-Yan. In Fig. 1.2 the CTEQ6L1 PDF [16] is exemplarily depicted.

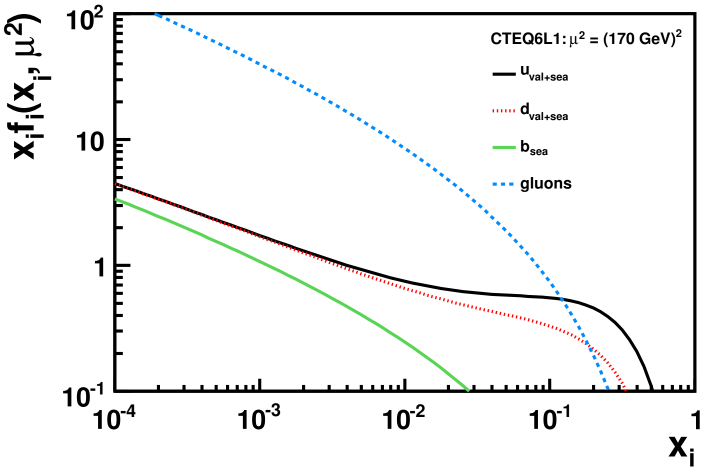

Figure 1.2.: The CTEQ6L1 PDF of up, down, bottom quarks and gluons in a proton. For up and down quarks the valence and sea distribution is illustrated. The scale is set to $\mu^2 = \left(170\,\mathrm{GeV}/c^2\right)^2$

The cross section calculation for hadron collisions is based on the factorization theorem, i. e. the cross section $\hat{\sigma}$ of the initial partons ij (for i and j q,$\bar{q}$ and g are possible) has to be folded with the PDFs of the incoming hadrons pp, for a proton-proton collision. In Eq. (1.3) this calculation is shown, where μ_R^2 is the renormalization scale of QCD and μ_F^2 the factorization scale which can be understood as the scale that separates the long- from the short-distance physics. $\hat{s}$ is the square of the center-of-mass energy of two colliding protons with momentum p_A and p_B: $\hat{s} = x_i x_j \left(p_A + p_B\right)^2$. If both incoming hadrons have the same energy E, $\hat{s}$ reduces to $\hat{s} = 4x_i x_j E^2$.

$$\sigma\left(AB \rightarrow cd + X\right) = \sum_{i,j} \int dx_i dx_j f_{i,A}\left(x_i, \mu_F^2\right) f_{j,B}\left(x_j, \mu_F^2\right) \cdot \hat{\sigma}\left(ij \rightarrow cd; \hat{s}, \mu_R^2, \mu_F^2\right) \tag{1.3}$$

1.2. Top Quark Physics

The top quark observation in 1995 at the Tevatron collider at Fermilab by the CDF [2] and DØ [3] collaborations was the end of a long puzzling search for the sixth quark. One had observed the bottom quark already in 1977 with a mass of $m_b \approx 4.2\,\mathrm{GeV}/c^2$ and knew that there had to be a sixth quark to complete at least the third generation of color charged fermions. The mass of the top quark has been measured by the Tevatron Electroweak Working group to $m_t = (173.2 \pm 0.9)\ \mathrm{GeV}/c^2$ [4], which is comparable with the mass of a tungsten atom. Meanwhile top quarks also have been observed at the LHC at CERN by the CMS and ATLAS collaborations [8, 17, 18].

Two important properties of the top quark are directly related to its large mass. Firstly, the lifetime of the top quark $\tau \sim 10^{-25}s$ is shorter than the typical time scale for QCD interactions ($1/\Lambda_{QCD} \sim 10^{-23}s$) [12]. This leads to a top quark decay before it can hadronize and form bound states with other quarks. Therefore the spin information and polarization of the top quark directly propagates through the W boson to its decay products. Secondly the top quark mass is close to the vacuum expectation value of the Higgs field ($v = 246\,\mathrm{GeV}$) and gives an estimation for the Yukawa coupling $g_Y = \frac{m_t}{v/\sqrt{2}} \approx 1$. This may hint at an important role of the top quark in electroweak symmetry breaking.

Top Quark Pair Production

The most dominant production mode of top quarks is the top quark pair production via the strong interaction. Therein quarks are produced in pairs due to flavor conservation. The top quark pair production via the electroweak interaction and interaction through a Z boson or photon exchange is negligible compared to the gluon exchange in hadron collisions [19]. In Fig. 1.3 the Feynman diagrams of these channels are depicted. One can distinguish in leading order between quark anti-quark annihilation, shown in Fig. 1.3(a), or gluon-gluon fusion, given in Fig. 1.3(b), Fig. 1.3(c) and Fig. 1.3(d), processes.

For $t\bar{t}$ creation the center-of-mass energy of the colliding partons has to fulfill at least $\hat{s} = 4m_t^2$, which leads, together with the approximation $x_i \approx x_j$, to a value for $x \approx \frac{2m_t}{\sqrt{s}}$. The center-of-mass energy at the LHC of $\sqrt{s} = 7\,\mathrm{TeV}$ leads to $x \approx 0.049$. At this value one can see from Fig. 1.2 that the PDF is dominated by gluons. The fraction of quarks in the PDF is very low for such a value of x. Hence, around 80% of all top quark pairs are produced through gluon fusion and around 20% by quark anti-quark annihilation.

The recent appoximative NNLO calculation for the cross section of top quark pair production is [20]:

$$\sigma\left(m_t = 173\,\mathrm{GeV}/c^2, \sqrt{s} = 7\,\mathrm{TeV}\right) = 165^{+4+9}_{-8-9}\,\mathrm{pb} \tag{1.4}$$

The first uncertainty in Eq. (1.4) describes the influence of the scale variation by a factor of 2 around $\mu = m_t$. The second uncertainty arises from PDF (MSTW2008 [21]) uncertainties.

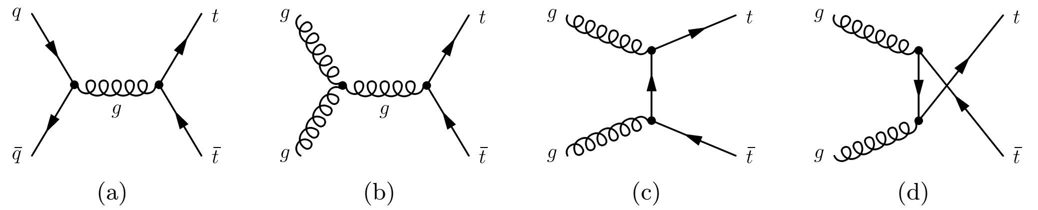

Figure 1.3.: LO Feynman diagrams for the top quark pair production via quark anti-quark annihilation (a) and via gluon-gluon fusion (b), (c) and (d).

Single Top Quark Production

Next to the dominating top quark pair production it is possible to produce single top quarks via the electroweak interaction. This production process was discovered 2009 by the CDF and DØ experiments [5, 6]. There are three production modes for this kind of top quark production. All three channels are shown in Fig. 1.4 at leading order. All processes include a Wtb vertex and therewith a vertex where the CKM matrix element V_{tb} directly occurs. This allows a direct measurement of the magnitude of $|V_{tb}|$. If one looks at the virtuality Q^2 of the W boson in all three processes, one can classify these modes.

- s-channel production (timelike virtuality Fig. 1.4(a))
- t-channel production (spacelike virtuality Fig. 1.4(b))
- tW-channel production (on-shell W boson Fig. 1.4(c) and Fig. 1.4(d))

Production channels with a Wts or Wtd vertex instead of the Wtb vertex are strongly suppressed in the SM due to the small off-diagonal CKM matrix elements (Eq. (1.2)). In the following all three channels with single top quark production via the Wtb vertex will be discussed in detail. The order is chosen according to the cross section for the processes at the LHC.

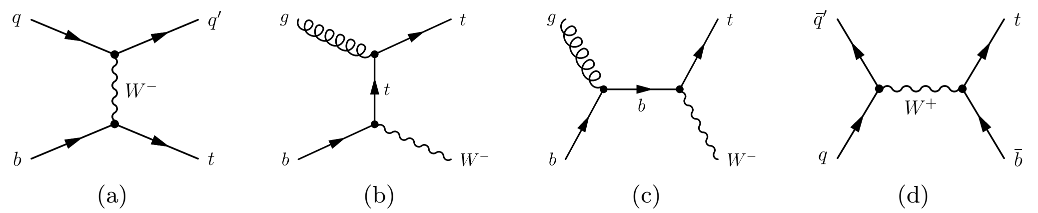

Figure 1.4.: LO Feynman diagrams for the electroweak production of single top quarks via the t-channel (a), the associated tW production (b) and (c) and the s-channel (d).

t-channel production

In the t-channel production mode, a b quark from the proton quark-sea electroweakly interacts with a light quark via W boson exchange. Both quarks change their flavor, hence the b quark becomes the top quark. It depends on the model for the proton quark-sea if a b quark is already included in the sea ($2 \rightarrow 2$ process, Fig. 1.5(b), Fig. 1.5(c) and Fig. 1.5(d)) or a gluon splits into a $b\bar{b}$ pair and provides the b quarks for the interaction ($2 \rightarrow 3$ process, Fig. 1.5(a)).

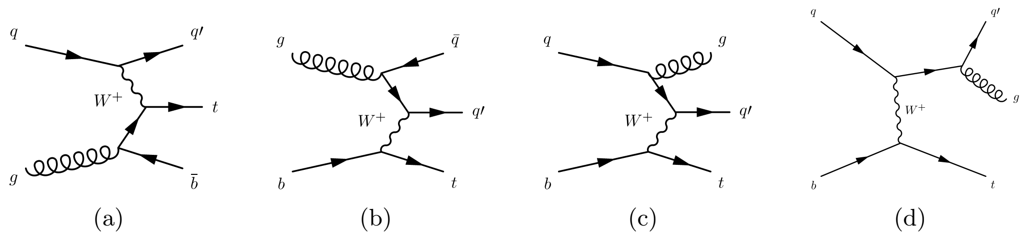

Figure 1.5.: NLO Feynman diagrams for the t-channel production of single top quarks. (a) and (b) show the gluon splitting into $b\bar{b}$ in the initial state. (c) and (d) show a gluon radiation from the light quark in the final state.

The b quark in the final state for the $2 \rightarrow 3$ process is called the spectator b quark (or second b quark). If this b quark has an own PDF as in the five flavor scheme (5FS), the $2 \rightarrow 2$ process becomes the LO Born process. Opposed to that, the four flavor scheme (4FS) does not have an own PDF for the b quark. Hence, a b quark in the proton can only appear as $b\bar{b}$ pair from gluon splitting. In this approach the $2 \rightarrow 3$ process is the leading order process.

In proton-proton collisions top and anti-top quarks are produced with different rates. Top quarks contribute roughly twice the rate than anti-top quarks, due to the valence quark content of the proton (uud). The cross sections for the different processes reflect this behavior: $\sigma_t \approx 2\sigma_{\bar{t}}$. An NNLO calculation using this method with MSTW2008 PDF [21] at a center-of-mass energy of 7 TeV yields [22]:

$$\sigma\left(m_t = 173\,\mathrm{GeV}/c^2, \sqrt{s} = 7\,\mathrm{TeV}, t + \bar{t}\right) = 64.6^{+3.4}_{-3.2}\,\mathrm{pb} \qquad (1.5)$$

The quoted uncertainties in Eq. (1.5) account for scale and PDF which includes uncertainties of the coupling strength α_s.

Associated production (tW)

The second most abundant single top quark production mode at the LHC is the tW mode, where a top quark is produced in association with a real or close to real W boson. Fig. 1.6 shows NLO Feynman diagrams for this channel.

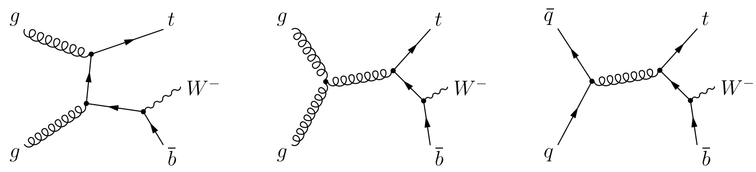

Figure 1.6.: Feynman diagrams of tW-channel single top quark production with NLO calculation.

The final states of these channels are the same as the ones for LO top quark pair production. This leads to interferences between these two processes and makes it impossible to differ associated single top quark production from top quark pair production. A study of the impact of this interference is done in reference [23]. In general there are two methods to estimate the effect of interference. One can subtract the overlap in the phase space by introducing a term which subtracts the $t\bar{t}$ contribution (diagram subtraction method) or one removes the diagrams shown in Fig. 1.6 from the NLO tW cross section calculation at all (diagram removal method). Both methods lead to the same rate and kinematic distributions within the scale variation method. In this analysis the diagram removal method is used as default, when nothing different is mentioned.
There is no difference in the initial state for t or $\bar{t}$, hence there is no different cross section for top quark production and anti-top quark production ($\sigma_t = \sigma_{\bar{t}}$). An NNLO cross section calculation is done in [24] and leads to:

$$\sigma\left(m_t = 173\,\mathrm{GeV}/c^2, \sqrt{s} = 7\,\mathrm{TeV},\right) = 7.8 \pm 0.2^{+0.5}_{-0.6}\,\mathrm{pb} \tag{1.6}$$

The first given uncertainty in Eq. (1.6) describes the scale variation by a factor of 2 around $\mu = m_t$. The second uncertainty in Eq. (1.6) stems from the variation of the PDF parameters (MSTW2008 [21]).

s-channel production

A quark and an anti-quark annihilate and produce a time-like W boson (Fig. 1.4(d)). Since there are no valence anti-quarks in the protons, the anti-quark has to be a sea quark of one of the protons. This explains not only the strong suppression of this production channel but also the different cross sections for top quark and anti-top quark production in this channel. Fig. 1.7 shows some NLO Feynman diagrams for real corrections.

An approximative NNLO cross section calculation for s-channel production of

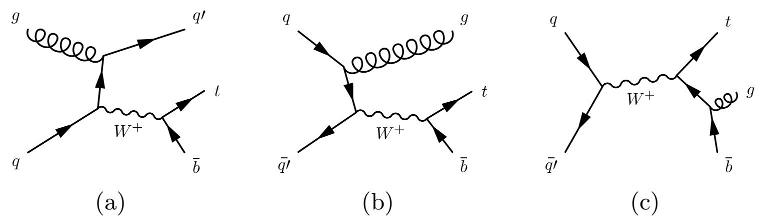

Figure 1.7.: Some Feynman diagrams of s-channel single top quark production with NLO calculation. (a) shows the initial state gluon splitting, where (b) shows the gluon radiation in the initial and (c) in the final state.

single top and anti-top quark [20] is shown in Eq. (1.7).

$$\begin{aligned}\sigma\left(m_t = 173\,\mathrm{GeV}/c^2, \sqrt{s} = 7\,\mathrm{TeV}, t\right) &= 3.17 \pm 0.06^{+0.13}_{-0.10}\mathrm{pb} \\ \sigma\left(m_{\bar{t}} = 173\,\mathrm{GeV}/c^2, \sqrt{s} = 7\,\mathrm{TeV}, \bar{t}\right) &= 1.42 \pm 0.01^{+0.06}_{-0.07}\mathrm{pb}\end{aligned} \tag{1.7}$$

The uncertainties in Eq. (1.7) describe the variation by a factor of 2 around $\mu = m_t$ and variation of the PDF parameters (MSTW2008 [21]).

Top Quark Decay and Spin Polarization

The above-mentioned short lifetime and large mass of the top quark leads to a decay via the electroweak interaction. Due to the CKM matrix element $V_{tb} \approx 1$, the top quark decays in almost 100% of the cases into a real W boson and a b quark. Decay modes involving an s or d quark are strongly CKM-suppressed by the small CKM off-diagonal elements V_{ts} and V_{td} (Eq. (1.2)).
The different final states are classified by the decay of the W boson. In the case of a hadronically decay the W boson decays into two light quarks, $W \to q'\bar{q}$, or it decays leptonically, $W^{\pm} \to \ell^{\pm}\nu_{\ell}$. The branching ratios of both decay classes are 67.6% and 32.3%. The leptonical decay stands out due to the easy detection of the charged lepton (e or μ) and will be discussed and used for the measurement in this analysis.

An additional consequence of the short top quark lifetime is the conservation of the spin information. Due to the fact that no hadronization are possible on that short timescale, top quarks decay in the same spin state as they were produced. An angular correlation in the decay of the top quark is given by the differential distribution of the decay angle Θ in Eq. (1.8) and is reasoned by the V-A coupling of the W boson to the top quark.

$$\frac{1}{\Gamma}\frac{d\Gamma}{d\cos\Theta} = \frac{1}{2}\left(1 + A_{\uparrow\downarrow}\cos\Theta\right) \text{ with } A_{\uparrow\downarrow} = \frac{N_{\uparrow} - N_{\downarrow}}{N_{\uparrow} + N_{\downarrow}} \tag{1.8}$$

$A_{\uparrow\downarrow}$ in Eq. (1.8) is called spin asymmetry. To evaluate this value one has to count the number of top quarks produced with spin up ($N_{\uparrow}$) and the number of top quarks produced with spin down ($N_\downarrow$). Γ in Eq. (1.8) represents the decay width. To extract the most significant Θ distribution, a spin basis has to be chosen where the spin asymmetry is maximized, meaning the top quark is mostly produced with either spin up or spin down. The angle Θ is the angle between the charged lepton from the top quark decay and the spin axis of the top quark in the top quark rest frame. The top quark rest frame is chosen because its easily accessible in experiments. As shown in reference [25] the direction of the down type quark is a natural spin axis. The top quarks are 100% spin up polarized in this direction. Since also the reconstruction of the down type quark jet is not perfect in the experiment, it is necessary to choose the direction which is most likely correct. This could be realized when one takes the direction of the hardest, non b-tagged, jet, called spectator jet, as spin axis (see Sec. 4). This choice leads to 95% polarization of spin up top quarks in proton-proton collisions at 14 TeV. In case of anti-top quark production it is more likely that the down type quark is in the initial state. Hence, the choice mentioned above would be wrong. However, momentum transfer via the t-channel deflects the incoming quark just slightly and the momentum vectors are nearly parallel between spectator jet and initial light quark. All in all about 93% of the anti-top quarks are produced with spin down in this spectator basis [25, 26].

In Fig. 1.8 the distribution of the polarization angle Θ for different center-of-mass energies obtained by Monte Carlo simulations with MadEvent [27] is shown. The independence of the different center-of-mass energies and further influences have been studied in [26].

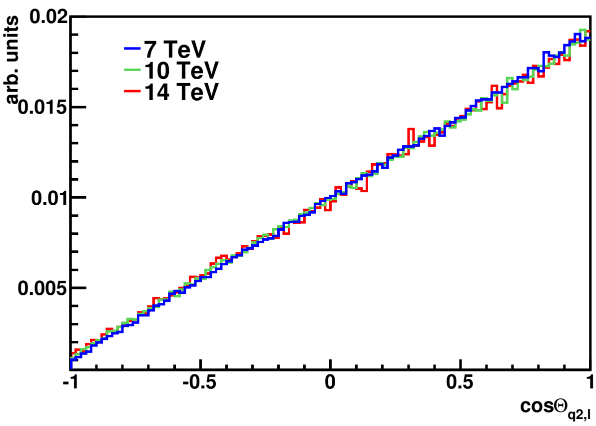

Figure 1.8.: Distribution of the cosine of the polarization angle Θ for single top t-channel events at different center-of-mass energies. Θ is the angle between the charged lepton from the top quark decay and the light quark, measured in the top quark rest frame. The events were simulated with MadEvent [27].

2. Experiment

Most of the particles of the SM are not part of the everyday life. All visible matter is made out of protons and neutrons, including up and down quarks, and electrons. They form atoms, which arrange matter in our sense of understanding. These are all first family particles, which are stable as contrasted with higher family particles that decay into particles of the first generation. To produce massive particles of a higher generation one needs such an energy to produce at least the mass of the new particles. This is possible in collider experiments which accalerate and collide particles and provide energy for the production of other particles.

At collider experiments the luminosity L is an important quantity, which mirrors the technical conditions of the beam and therewith is a pure accelerator quantity. The number of events N_{exp} of a certain process, with the cross section σ_{prod}, is calculated from integration over time of the interaction rate $\frac{dN_{\text{exp}}}{dt}$, which depends on the instantaneous luminosity L of the experiment,

$$\frac{dN_{\text{exp}}}{dt} = L \cdot \sigma_{prod} \Longleftrightarrow N_{\text{exp}} = \int L \cdot \sigma_{\text{prod}} dt = \mathcal{L} \cdot \sigma_{\text{prod}} \, . \tag{2.1}$$

In Eq. (2.1) $\mathcal{L}$ describes the integrated luminosity, which is generally quoted to estimate the number of events that have been recorded. The luminosity L for two colliding bunches a and b consisting of N_a and N_b particles is given by [28]:

$$L = f \cdot \frac{N_a N_b}{4\pi \sigma_x \sigma_y} \, , \tag{2.2}$$

where f is the frequency of the collisions and σ_x and σ_y are the sizes of the Gaussian shaped bunches. The CMS experiment continuously measures the instantaneous luminosity by controlling the size and shape of the beam with a so-called van der Meer scan [29]. The underlying data sets, which are evaluated in this analysis, correspond to an integrated luminosity of $\mathcal{L} = (920.7 \pm 41.3)\,\text{pb}^{-1}$. The uncertainty of $\mathcal{L}$ is described and calculated in [30].

2.1. Large Hadron Collider

The Large Hadron Collider (LHC) [31] is a circular hadron accelerator located at CERN[1] near Geneva, Switzerland. The tunnel of LHC was already used by the

[1] Conseil Européen pour la Recherce Nucléaire

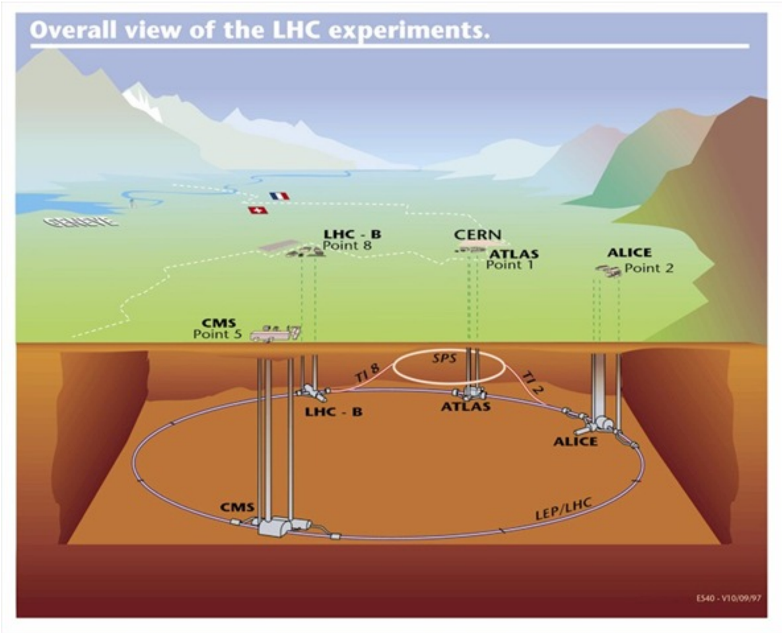

Figure 2.1.: Overview of the arrangement of the LHC accelerator and its experiments. The LHC ring is located 100 m below the surface and uses the old LEP tunnel. There are four main experiments installed: LHCb, ALICE, ATLAS and CMS.

Large Electron-Positron Collider (LEP) and has a circumference of 26.7 km placed around 100 m underground. Four big experiments are placed at the collision points around the ring. Two detectors, ALICE [32] and LHCb [33], are specialized in certain physical processes, whereas the two multipurpose detectors, ATLAS [34] and CMS [35], are built for the discovery of new particles and the precise measurement of physical processes. In Fig. 2.1 a schematic overview of the LHC accelerator is given. Data which has been recorded with the CMS experiment in the first half of 2011 is evaluated within this analysis.

The two proton beams are accelerated in two beam pipes embedded in a cryostat. Super-conducting Niobium-Titanium (NbTi) magnets operate at a temperature of 1.9 K and produce a field strength of 8.33 T, which is necessary to track the protons inside the beam pipes. Super fluid Helium at temperatures below 2.2 K cools the magnets. Overall 1232 super-conducting dipole magnets are used for radial acceleration and 392 quadruple magnets keep the beam focused.

The collision of the protons occurs inside the experiments at a design energy of 7 TeV per beam. In the first two years of LHC operation, collisions have been recorded at an energy of 3.5 TeV per beam. By sharpening the beam focus, increasing the number of protons per bunch and the number of bunches per beam the instantaneous luminosity reached $3.5 \cdot 10^{33}\,\mathrm{cm}^{-2}\,\mathrm{s}^{-1}$ at the end of 2011. The

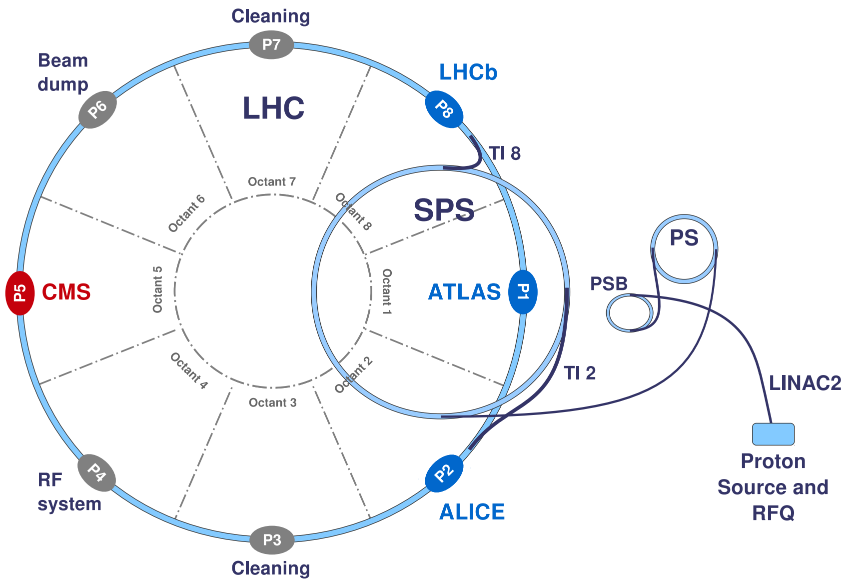

Figure 2.2.: Sketch of the CERN accelerator complex (not in scale). The order for the proton acceleration is: source - RFQ - LINAC2 - PSB - PS - SPS - LHC [36].

integrated luminosity recorded by CMS in the first two years of proton-proton collisions with an energy of 3.5 TeV totals to $\mathcal{L} \approx 5.7\,\text{fb}^{-1}$.

Before the protons enter the LHC ring, they have to be accelerated to a certain energy. This is done by several pre-accelerators [37] shown in Fig. 2.2. Electrons are fired on hydrogen plasma and produce a proton current. The extracted protons are accelerated by a 90 kV supply and enter a radio frequency quadruple (RFQ). This splits the beam into different bunches and accelerates the protons to an energy of 750 keV. A chain of different accelerators follows, each providing a particular energy rise to the beam. At the end of LINAC2, a linear accelerator, the protons have an energy of 50 MeV. In the Proton Synchrotron Booster (PSB) the energy rises to 1.4 GeV and the Proton Synchrotron (PS) accelerates the particles to 25 GeV. At a last step before the main LHC ring the Super Proton Synchrotron (SPS) increases the beam energy to 450 GeV. The beam splits up into two beams and both are injected in opposite directions into the LHC.

2.2. Compact Muon Solenoid (CMS)

One of the largest experiments in particle physics ever built, is one of the two multipurpose detectors at the LHC, called Compact Muon Solenoid (CMS) [31]. It is placed at an interaction point of the LHC ring 100 m underground in a cavern at Point 5 near Cessy, France. The detector is 21.6 m long, has a diameter of 14.6 m and a total weight of 12500 t. An overview of the CMS detector and its components, which are introduced in detail in the next sections, is given in Fig. 2.3. The design of CMS was driven by the aim to discover the Higgs boson and to search for super-symmetric particles. Very promising channels for the Higgs boson search comprise leptons ($H \rightarrow ZZ^* \rightarrow \mu\mu\mu\mu$) or photons ($H \rightarrow \gamma\gamma$) in the final states. Hence, the detection and measurement of isolated photons and leptons were the crucial topic for the design of the CMS detector. Particles that only interact via the weak force like the super-symmetric ones or neutrinos cannot be detected directly but leave footprints in the total sum of transverse momenta which must be conserved in each event. Overall the detector needs to cover a high angular range with a maximum of sensitive detection material.

The CMS detector has a modular structure which divides the detector into 15 sections and made it possible to build every part on surface and assemble them in the cavern. In addition the modular structure allows a disassemblement of the entire detector for inspection, maintenance and enhancements. For reconstruction and measurements of an event it is useful to introduce a coordinate system, which has its origin at the nominal collision point. The x-axis points to the center of the LHC ring and the y-axis vertically upwards. The z-axis is defined along the beam direction in such a way that the coordinate system is right-handed. Moreover two angular quantities are defined with respect to the coordinate axes. The azimuthal angle ϕ is located in the x-y plane, where the polar angle θ is embedded in the x-z plane. Another variable which is useful and often used is the pseudorapidity η defined as $\eta = -\ln\tan\left(\frac{\theta}{2}\right)$. For massless particles the pseudorapidity is equal to the rapidity $y = \frac{1}{2}\ln\left(\frac{E+p_z}{E-p_Z}\right)$, which is defined in the laboratory frame and Lorentz invariant under longitudinal boosts.

The following subsections describe the different sub-detectors, starting from the nominal interaction point in the center of the detector.

Tracking System

The tracker [39, 40] is the innermost sub-detector system of the CMS experiment. It measures the tracks of charged particles coming from the interaction point. The tracker has a cylindrical shape, is 5.8 m long and has a diameter of 2.5 m. A schematic overview can be seen in Fig. 2.4. All components of the tracker operate at a temperature of −20 °C. The tracker is based on a doped semiconductor, operated in reverse-biasing mode. A charged particle flying through such a depletion region leaves a signal measurable as current. The small cell size of these modules gives a high granularity and many hits of a charged particle can be arranged to a track. The high magnetic field of 3.8 T infiltrates the tracker, bends the trajectory of a charged particle and allows to measure its momentum by the curvature of the track. For the LHC design luminosity one event produces a large amount of particles that hit the tracker. Therefore the tracker needs to have a fast response time and high granularity. To have the good mixture between precise measurement and a

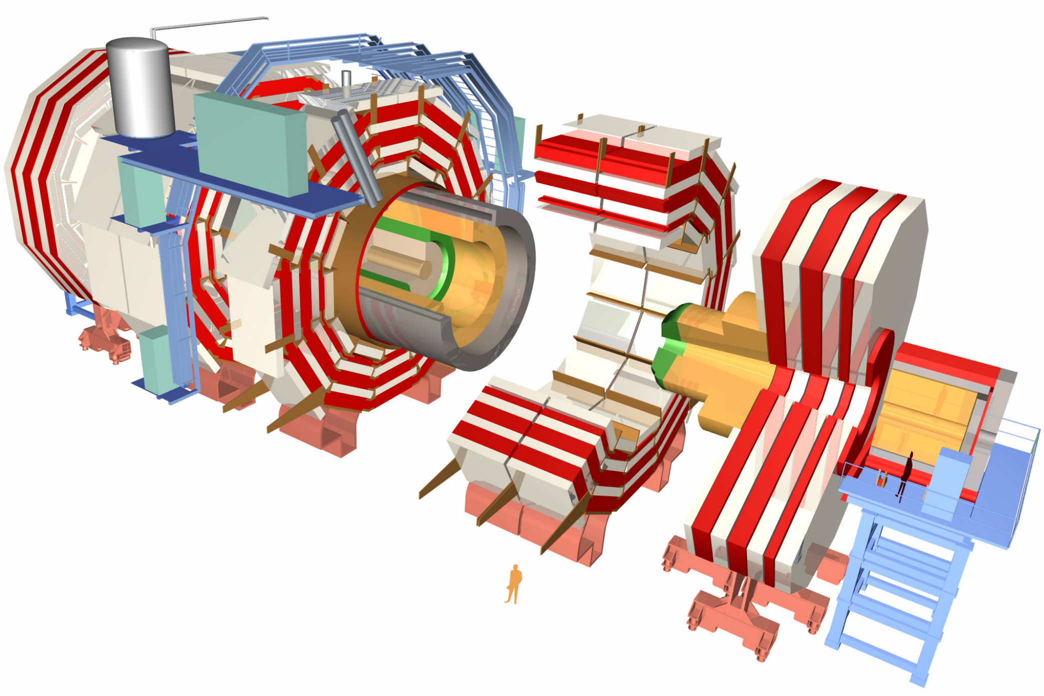

Figure 2.3.: Schematic overview of the Compact Muon Solenoid (CMS) detector [38]. The detector has onion-like layers around the beam pipe. Tracking system, electromagnetic and hadronic calorimeters are surrounded by the super-conducting solenoid. The muon system is integrated into the iron return yoke. This sketch gives an impression of the modular concept of the CMS detector with several barrel segments and two end cap disks.

minimum number of read-out-material there are two tracker systems: the silicon pixel detector and the silicon strip detector.

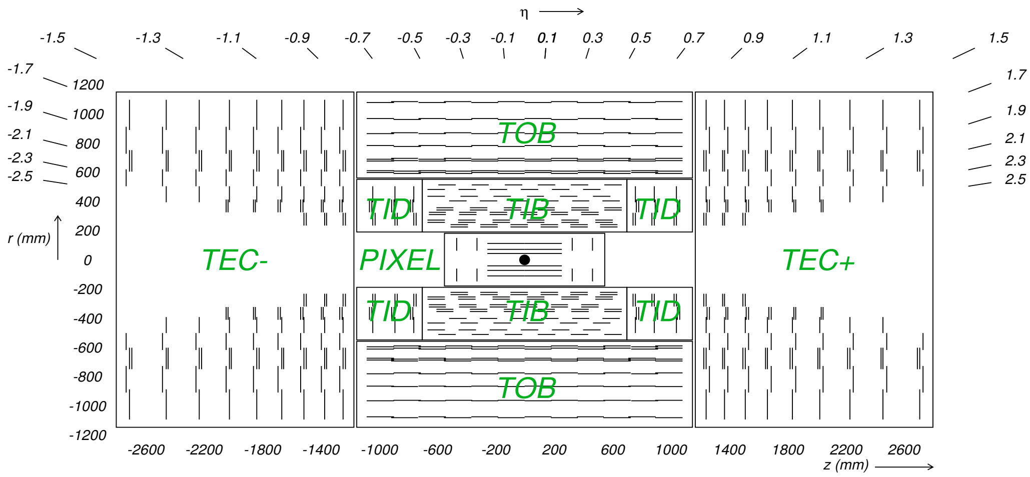

Figure 2.4.: Schematic overview of the CMS tracking system. The tracker is the closest component to the beam pipe. It is separated into different parts, the silicon pixel detector is surrounded by the silicon strip detector.

Silicon Pixel Detector

The silicon pixel detector has the smallest cells of depletion regions and gives a very precise measurement of the location of the particle. Its size is $100 \times 500\ (\mu\text{m})^2$ which gives a single point resolution of $10\,\mu$m in the r-ϕ plane and $15\,\mu$m in the z direction. The silicon pixel detector encloses the beam pipe in three layers with distances of 4.4 cm, 7.3 cm and 10.2 cm and a total length of 53 cm. There are two end cap disks extending from 6 cm to 15 cm in radius. Overall the silicon pixel detector has a surface of $1\,\text{m}^2$ and contains 66 million pixels, the covered pseudorapidity range is $|\eta| < 2.5$.

Silicon Strip Detector

As opposed to a pixel detector a strip detector has an extended depletion region. The advantage is a lower heat production and less read-out-electronics but with a small loss of accuracy. These components lead to polysemous measurements if the current of charged particles through it is too high, only when the current is reached under a certain threshold the silicon strip detector provides a reasonable result. It surrounds the pixel detector and is divided into different subsystems: Tracker Inner Barrel (TIB), Tracker Outer Barrel (TOB), Tracker Inner Discs (TID) and two Tracker End Caps (TEC). Overall the silicon strip detector contains 9.6 million silicon strips. The arrangement of the subsystems can be seen in Fig. 2.4. The expected transverse momentum resolution for muons with a transverse momentum in the order of 100 GeV/c is around 1.5%.

Electromagnetic Calorimeter (ECAL)

The tracking system is followed by the calorimeters. They measure the energy of an incident particle and help to identify it. The electromagnetic calorimeter especially measures the energy of electrons and photons. Its material needs to be very dense in order to stop high energetic photons and electrons. They produce a cascade of photons and e^+-e^--pairs within the material. The ECAL is made out of lead tungstate ($PbWO_4$) crystals that are transparent and therefore operate as scintillator and absorber at the same time. The high density of this material ($8.28\,\mathrm{g/cm^3}$) achieves a small radiation length of the shower particles ($X_0 = 0.89\,\mathrm{cm}$) and hence a thin design of the ECAL. In addition, the scintillation time of the material is of the same order as the nominal bunch crossing rate of 25 ns. 61200 of these crystals constitute a homogeneous calorimeter. The ECAL of the CMS detector is one of the big strengths of the whole detector. An impression of the position and the size of the ECAL in comparison to other components is given in Fig. 2.5. It covers an η region of $|\eta| < 2.6$. The energy resolution of the electromagnetic calorimeter can be parameterized as:

$$\left(\frac{\sigma_E}{E}\right)^2 = \left(\frac{S}{\sqrt{E}}\right)^2 + \left(\frac{N}{E}\right)^2 + C^2 \,. \tag{2.3}$$

In Eq. (2.3) the energy of a particle E is given in units of GeV; S describes the stochastic term, which depends on event-to-event fluctuation in lateral shower containment, photo-statistics and photo-detector gain; N represents the noise term (given in units of MeV), which is sensitive to the level of electronic noise and C is the constant term, which depends on non-uniformity of the longitudinal light collection and leakage of energy. By fitting test beam measurements to this functions, the values for these parameters can be determined. For electron beams with an energy of $20 - 250\,\mathrm{GeV}$ [41] the parameters are determined to $S = 2.8\%$, $N = 41.5$ and $C = 0.3\%$.

Hadronic Calorimeter (HCAL)

To identify hadrons and other strong interacting particles and measure their energy, the hadron calorimeter (HCAL) surrounds the ECAL. It is a typical sampling calorimeter where non-magnetic brass, which has a short interaction length of $X_0 = 16.42\,\mathrm{cm}$, is used for absorption and plastic scintillator tiles appropriate as active material. The HCAL is split into four parts: hadron barrel (HB), hadron end cap (HE), hadron outer (HO) and hadron forward (HF). In Fig. 2.5 the position of all four parts are depicted.

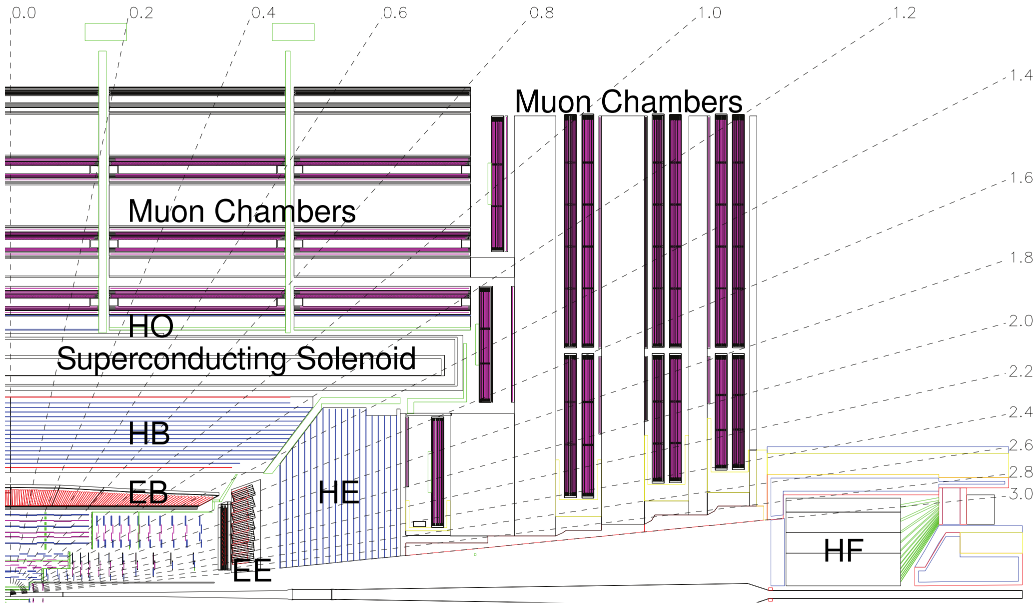

Figure 2.5.: Longitudinal view of one quarter of the CMS detector. Dashed lines mark the corresponding η value. One can see the arrangement of different elements in the barrel and end cap. The ECAL is marked with EB (electromagnetic barrel) and EE (electromagnetic end cap). The HCAL is split into four parts: HB (hadron barrel), HE (hadron end cap), HO (hadron outer) and HF (hadron forward).

36 flat brass absorber plates aligned parallel to the beam axis form the HB over a range up to $|\eta| < 1.3$. Between these absorbers 17 plates of active plastic scintillators are arranged. The HE calorimeter covers a pseudorapidity range of $1.3 < |\eta| < 3.0$ and together with the HB it fully surrounds the ECAL inside the solenoid. Outside the solenoid the HO is located. It consists of two scintillator tiles outer the solenoid to increase the effective thickness of the HCAL by using the solenoid as additional absorber material. This leads to an improvement of the energy resolution function and missing transverse energy measurement. The HF is located around 11 m from the nominal interaction point and extends the pseudorapidity range to $3.0 < |\eta| < 5.0$. The HF is made out of quartz fibers embedded in steel absorbers. Photo multipliers detect the emitted Cerenkov light from particle showers in the quartz fibers. The large η range of the HF makes it possible to detect forward jets, which are typical in certain event signatures of the singe top t-channel process (see Fig. 1.4(a)). The recoiling light quark is presumably found in the forward region of the detector.

Muon System

All detectable particles are stopped by the described components except for muons. Hence, the muon system is the last sub-detector at the outside of the CMS detector. It is used for muon identification, triggering and precise momentum measurement. There are three different types of gaseous detectors: Aluminum drift tubes (DT) in the barrel region, cathode strip chambers (CSC) in the end cap and resistive plate chamber (RPC) in both regions. All drift chambers are embedded in the iron return yoke and are infiltrated by a magnetic field of 2 T. In Fig. 2.6 the layout of the muon chambers is illustrated.

In the barrel region ($|\eta| < 1.2$) four layers of DT chambers are installed. In this region the neutron induced background is small as well as the muon rate. At the end caps these rates are much higher, thus each end cap has four layers of CSC chambers which have a fast response time, a fine segmentation and a high radiation resistance. The RPC chambers are in both regions. They combine a very fast response time with a good time resolution, which provides necessary information for trigger. A detailed description of the muon system can be found in [42].

Trigger System

At the instantaneous luminosity, which is reached through the 2011 runs, the interval of a bunch crossing for protons is 50ns. This is equivalent to a crossing frequency of 20 MHz and with six simultaneous pp collisions every crossing. This leads to a huge amount of data which cannot be saved completely. Hence it is necessary to filter events that are interesting for processing and analyzing. To reduce this rate a trigger system selects only a subset of all events. There are two steps of triggers used: the Level-1 (L1) Trigger and the High-Level-Trigger (HLT). The L1 Trigger

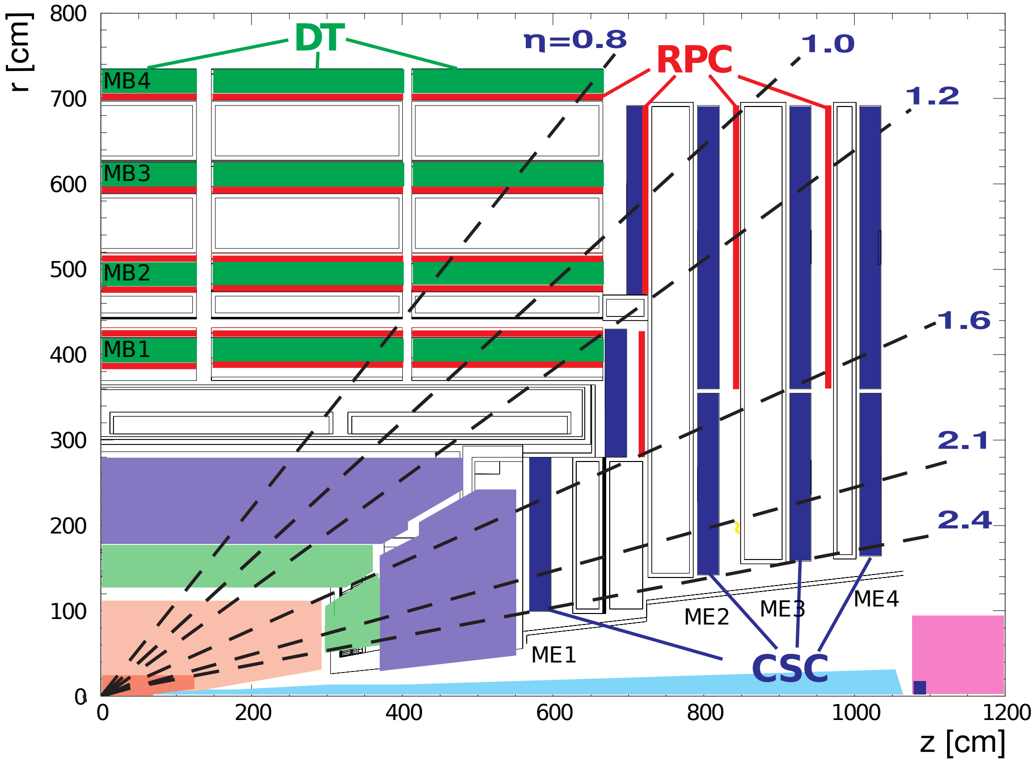

Figure 2.6.: Longitudinal view of one quarter of the CMS muon system [43]. Muons can be detected by DT chambers (green) in the barrel region and CSCs (blue) in the end cap. RPCs (red) are installed in both regions. The muon system is embedded in the iron yoke (white).

is based on hardware systems which roughly read out only a few sub-detectors like the calorimeters or the muon system. This reduces the rate of events to less than 100 kHz. The HLT is a software based trigger system that uses more detailed information of all sub detectors and has already offline analysis tools available. This reduces the event rate by a factor of 1000. The remaining events can be stored and processed for analysis. The architecture of the CMS Data Acquisition System is shown in Fig. 2.7.

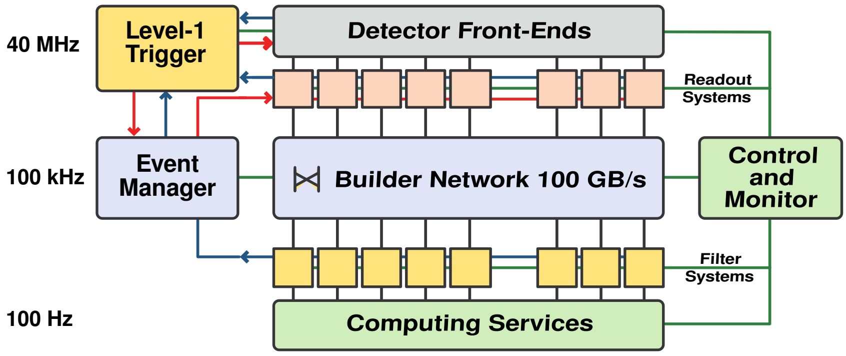

Figure 2.7.: This chart shows the architecture of the CMS Data Acquisition System [35]. The trigger system reduces the data flow from 40 MHz to 100 Hz. The complete detector read-out is stored in a pipeline. After the L1 trigger accept signal the detector information is forwarded to the readout systems. The event manager controls the data flow through the builder network and builder units. After defragmentation the information of the events the HLT intervenes. Everything is controlled and monitored by the control and monitor system.

Computing Infrastructure

The huge amount of data and its processing implies the necessities of a lot of computing resources. In addition, all members working at LHC need access to the data. Hence CMS decided to use the hierarchical, tier structured LHC computing grid [44]. The raw data that passes the HLT is stored at the Tier-0 center at CERN. After preprocessing the raw data it is transfered to various Tier-1 centers at national computing facilities around the world, so it is achievable by at least two independent sites. The Tier-1 centers store also the simulated data. Tier-2 centers store copies of MC samples and data streams, which are required for physics analyses. Additionally Tier-1 and Tier-2 centers provide resources for MC production. The computer clusters are accessible for grid jobs submitted by a user. Tier-3 centers are local analysis centers for the end user. Fig. 2.8 gives a schematic overview of the CMS computing grid.

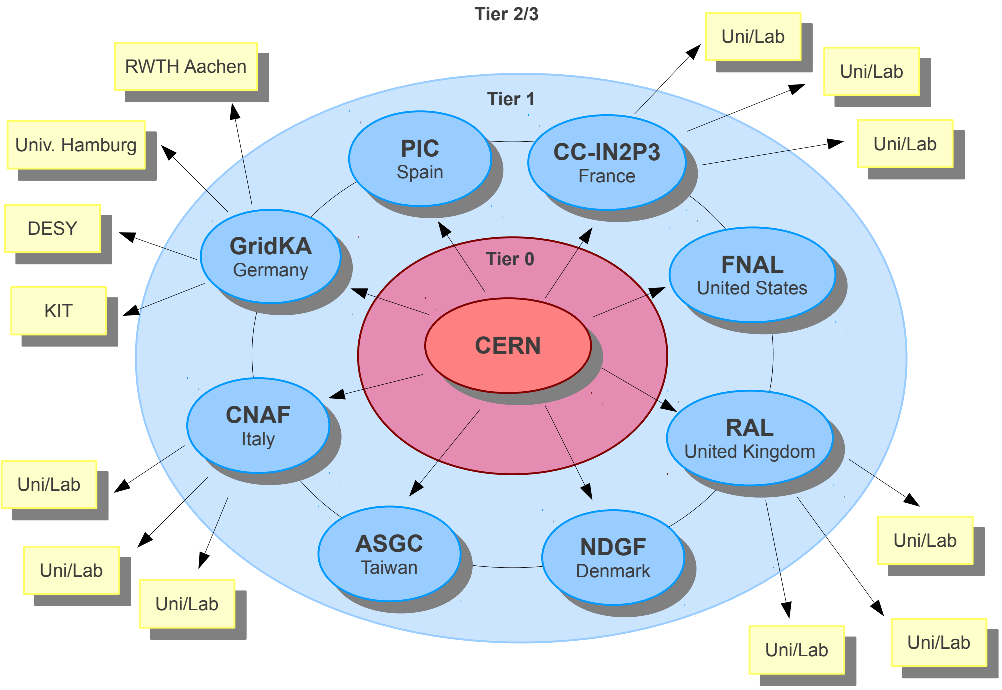

Figure 2.8.: Schematic overview of the CMS computing grid, adapted from [45]. At CERN the Tier-0 site receives all data that is collected by the experiments. From there, it is transferred to Tier-1 centers all over the world. Data and simulated data is distributed to Tier-2 sites, where it is available for analyses which are mainly performed on Tier-3 sites.

3. Generation, Simulation and Reconstruction of Single Top Quark Production

In each collision a huge number of electrical signals from the read out devices are produced by every interaction of particles with the detector material. To translate this raw detector information into physically interpretable quantities, it is essential to reconstruct physical objects and their kinematic properties. This translation is accomplished by different reconstruction algorithms in the CMS offline software (CMSSW) introduced in the following sections.

In addition to recorded events from the detector simulated events are needed, which are indistinguishable from recorded events and which are reconstructed the same way. This simulation is carried out with so-called Monte Carlo (MC) methods, based on randomly generated events according to the probability of a given process. For such a simulation the CMS detector is fully emulated as well. Collectively, simulated and recorded events can reasonably be compared with each other and provide information on the physical processes of the Standard Model or give hints to undiscovered physical effects. The advantage of simulated events is the possibility to have access to the real process (MC truth). The following sections describe the event simulation and reconstruction for MC generated events and recorded data.

3.1. Generation of Events

The hard parton interaction is calculated with MC generators with respect to the corresponding matrix elements of the processes and the probability density of the phase space. MC techniques ensure that a point in the phase space is picked randomly. A full simulation of a proton-proton collision contains several steps which can be factorized. A schematic overview of these simulation steps is shown in Fig. 3.1 and more detailed descriptions can be found in the following four sections.

Hard scattering

The PDF distributions describe the momentum fraction of each parton flavor at a certain energy scale Q^2. Exemplarily, a PDF distribution is shown in Fig. 1.2. In a hard interaction only one parton of each proton takes part and since the strong coupling constant α_s is small for large Q^2, the cross section can be calculated with

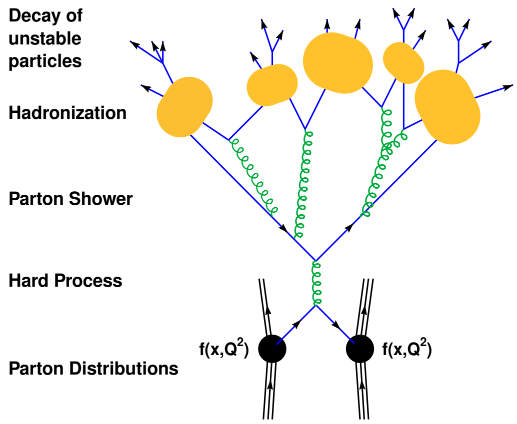

Figure 3.1.: Schematic overview of the different steps of MC event generation processes, adapted from [46]. The interaction of partons is simulated with respect to PDF and the matrix element. A next step generates additional soft radiations from initial and final states partons. In the hadronization stage color-neutral particles are formed. The last event generation step simulates the decay of unstable particles. A simulated event should be indistinguishable from a detector recorded event.

the help of perturbation theory. As a consequence the so-called matrix element (ME) method is introduced, which uses the Feynman diagrams of a certain process and the corresponding transition amplitude to calculate the probability of such a process to occur.

Parton Shower

In the second step of the MC event generation the radiation of gluons and the production of additional quarks, called initial state radiation (ISR) and final state radiation (FSR), is simulated. Two different methods are used to generate such radiations.

Analogically to the hard scattering process step the ME method calculates the probability of radiation based on perturbation theory. This method is limited to interactions with high momentum transfer since the perturbation theory is valid only for $\alpha_s \ll Q^2$. After that the Parton Shower (PS) approach uses simplified models for the kinematics of the interaction. The structure of gluon radiations, given in terms of branches, can be described mathematically by the DGLAP QCD evolution equation [47, 48, 49]. The probability of radiating a gluon is calculated via the Altarelli-Parisi splitting functions. ISRs are approximated as space-like showers, where the shower initiators can be found by starting from the two incoming partons at the hard interaction, tracing the shower backwards in time, modeled in terms of sequence of decreasing Q^2 and increasing momentum fraction x. Contrarily FSRs are modeled by decreasing the Q^2 scale along the positive time direction. In order to avoid singularities arising from soft and collinear gluon emission, a lower cut-off value is essential.

Hadronization and Decay

The next step of the MC event generation models the transformation of colored partons into colorless hadrons, called hadronization. Free colored objects cannot be directly observed in nature, they are bound together in hadrons. Due to the fact that perturbation theory is only valid at short distances and high energy scales, it breaks down trying to describe the hadronization correctly. Rather it is required to use purely phenomenological models, where required parameters are tuned to data. One of the most prominent models for this generation step is the Lund string model [50]. In this model the color field between separating quarks and anti-quarks is modeled as a color flux string. If the bound particles depart from each other the potential energy of these color strings increases till the point is reached where the energy exceeds the level to produce a new $q\bar{q}$ pair. This process repeats itself until the energy is too small to create new pairs of quarks. At the end of the hadronization step the decay of unstable baryons and mesons is simulated randomly with respect to the known branching ratio of the hadrons.

Underlying Event and Pile-Up

In addition to the hard scattering process an event contains contributions from other processes as well. The proton remnant of the parton collision is color charged and interacts with particles of the hard interaction. This process is called underlying event and has to be taken into account in the MC simulation. A more detailed description of the underlying event is given in [51].

In addition, an other process, the so-called pile-up has to be considered as well. Pile-up events occur at high instantaneous luminosities when more than just two protons collide during the same bunch crossing (in time pile-up). For LHC design luminosity there can be up to 25 pile-up events at the same time. For the data set that is examined in the analysis the average number of pile-up events is determined to be six. The influence of (in time) pile-up events is taken into account in the MC event simulation.

3.2. Monte Carlo Generators

With respect to the several steps in the event simulation there are different kinds of Monte Carlo generators available. For a full event generation with all steps from the hard scattering up to the decay, diverse types of generators are combined with appropriate matching methods, i. e. CKKW [52, 53] and MLM [54]. Some event generators like Pythia [55] and Herwig [56] are equipped with a full event generation modeling including the hadronization and decay. In contrast to those there are matrix element generators like MadGraph/MadEvent [57, 58, 59] or Alpgen [60], which provide simulations for ISR and FSR in LO matrix elements, but no simulation for hadronization. Another kind of simulation is required for the detector. Geant is a detector simulation program [61], which simulates the interaction of particles with the detector material. A short overview of different MC generators used in this analysis is given in the following.

Pythia

The potential of the Pythia simulation extends from hard scattering simulation to ISR/FSR generation via the PS approach and hadronization modeling, using the Lund string model, to many models beyond the Standard Model for the hard interaction as well as soft contributions. It also includes contributions from underlying events. This constitutes Pythia to a multipurpose MC event generator for particle collisions at high energies. Combined with an external matrix element generator like MadGraph/MadEvent, Pythia is mostly used for the simulation of some background processes in this analysis.

MadGraph and MadEvent

A fusion of the matrix element generator MadGraph and the tree level generator MadEvent affords a powerful simulation of diverse sets of hard interaction processes. In addition to determining the amplitude for a given process including all subprocesses, MadGraph also provides information for the phase space integration. MadEvent processes this information and calculates cross sections and generates MC events. The output is stored in the Les Houches event format (LHE) [62] and can be committed to Pythia to simulate showering and hadronization. The MLM matching method [54] taking double counting of processes into account. For enhanced models with new hypothetical exchange particles MadGraph/MadEvent is easily expandable.

Powheg

The Powheg (Positive Weight Hardest Emission Generator) simulation software package [63, 64] provides the combination of a parton shower generation with a fixed NLO QCD calculation. The event weight is always positive and overcounting is avoided by design. Powheg is embedded in the framework PowhegBox [65] and calculates events on NLO precision. Therewith it includes both single top quark t channel processes ($2 \to 2$ and $2 \to 3$). The basic idea of this MC generator is to generate the hardest radiation first and then feed the event to any shower generator for softer radiations. Powheg is frequently combined with Pythia to simulate showering and hadronization.

3.3. Detector Simulation

If the particles produced in a collision traversing through the detector they presumably interact with the detector material and produce hits in the tracker or signals in the calorimeters. In order to have realistic simulated events it is necessary to simulate the detector itself. A detailed model of the CMS detector and its material is modeled with the GEANT toolkit [61]. It takes into account all physical effects like energy loss by ionization, bremsstrahlung, electromagnetic and hadronic interactions and simulates the electric response of the read out electronics. Since the simulation of an event with the full detector simulation requires a lot of time and computing resources there is also a fast simulation of the detector available [66]. With simplified models for interactions and a trimmed detector layout simulation the computing time shrinks by a factor of 100, where the results are still competitive.

3.4. Signal Modeling

In this analysis, the single top quark production is simulated with the POWHEG MC generator. It calculates all three production modes of the single top quark production on NLO accuracy. A detailed description can be found in [67]. For this processes the top quark mass is set to $m_t = 172.5\,\mathrm{GeV}/c^2$, the renormalization and factorization scale is set to $\mu_r = \mu_f = m_t$ and MSTW2008 [21] NNLO central PDF set.

3.5. Reconstruction of Events

The reconstruction step translates the raw electrical signals from the read out electronics to physical objects with kinematics. This is accomplished by different algorithms embedded in the CMSSW in order to aim at obtaining all particles which arose from the hard scattering event. In a first step, tracks of charged particles in the tracker are reconstructed by fitting trajectories trough the hits in the tracker with respect to energy deposits in the calorimeter systems. To receive the physical object of a track, calorimeter entries are linked to hits in the tracker. Reconstructed tracks are used to identify the de facto interaction point. In the following different reconstruction steps are applied on recorded data and simulated MC events. A more detailed description for events recorded with the CMS detector can be found in [43].

Reconstruction of Charged Particles

Charged particles are influenced by the magnetic field and traverse the detector on bent trajectories and may leave hits in the tracker system of CMS. These hits are used to reconstruct trajectories with the Combined Track Finder (CTF) [68], particularly a Kalman Filter (KF) [69]. Since a global fit to all hits in the tracker and all energy deposits in the calorimeters simultaneously needs too much computer resources, the KF uses local fits to find the actual trajectories. The track reconstruction is split up in several iterations. First, hits in the innermost pixel detector are used as seeds for a trajectory candidate. Such a seed has to fulfill two criteria: In addition to a beam spot constraint a seed has to have a hit triplet or two hits. The KF algorithm looks for hits in the subsequent layers with respect to the motion of the charged particle through the magnetic field, the energy loss in the tracker material and multiple scattering. For each found hit a trajectory candidate is created. Since charged particles do not necessarily generate a hit in every layer the next layer is examined in case no hit is found for a specific extrapolation. If two consecutive layers have no hit, the trajectory candidate is rejected. The fit of all trajectory candidates is calculated in parallel until the outer layer is reached. To avoid overlaps between two candidates the trajectories are compared with each other. In case of two tracks having more than half of their hits in common, the algorithm rejects either the trajectory with the lower number of hits, or in case that both tracks have the same number of hits, the one with the lower χ^2 value of the fit is rejected. An additional global fit is applied after the local fit of the KF in order to improve the precision of the track parameters.

Reconstruction of Vertices

The interaction of the hard scattering process takes place at the primary vertex (PV). It is important to reconstruct it to estimate the number of pile-up events and to make b tagging (see Sec. 3.5.1) possible. The reconstruction of the PV is based on the search of a common origin of reconstructed tracks. Vertex candidates arise from different track groups and a re-fitting assumes that they come from that vertex. For the HLT, where speed is important, the PV search is reduced in a way that only the z-coordinate is taken into account. For a more accurate search of the PV there are mainly three criteria, which the tracks have to fulfill: Two hits in the pixel detector are required, as well as seven hits in the silicon strip detector and in addition the χ^2 value of the fit divided by the number of degrees of freedom has to be smaller than 5.0.

Particle Flow Algorithm

For the reconstruction of electrons, muons, jets, and any imbalance in transverse momentum due to neutrinos, the particle-flow (PF) algorithm is used. It combines the information of all sub-detectors and reconstructs stable particles individually. The main idea is to combine elements such as energy deposits in the calorimeters, hits in the muon chambers and hits in the tracker, in order to get as much information about the particle as possible. The PF algorithm reaches a high efficiency and a low fake rate at identifying and matching these different elements with advanced tracking and clustering algorithms, which are explained in detail in [70]. In the following sections the reconstruction of electrons, muons and jets is described in more detail, where the focus lies on the electron reconstruction, due to the event selection (see Sec. 4) in this analysis.

Reconstruction of Electrons

As charged particles, electrons leave hits in the tracker system and energy deposits in the ECAL. Due to their comparatively low mass, they loose a large amount of energy when flying through the tracker due to the emission of bremsstrahlung photons. These photons leave signatures in the ECAL along the ϕ direction of the electron trajectory.

Two complementary algorithms are used within the PF algorithm to reconstruct electrons. Firstly there is an ECAL-driven reconstruction which starts with searching for energy deposits and combines them in 'super clusters' with respect to the electron kinematics. As the electron trajectory can be considerably bent by the magnetic field, the bremsstrahlung photon and electron energy deposits can be widely spread along the azimuthal direction. A mentioned 'super cluster' is used to seed the reconstruction of the electron track in a fitting procedure. It is able to identify sudden changes in curvature due to bremsstrahlung photon emission. This ECAL-driven reconstruction method performs well for high-p_{T} and isolated electrons [71].

For low-p_{T} or not well isolated electrons the reconstruction method is different. The seeding for such an electron reconstruction comes off a subset of all tracks reconstructed in the event, which are compatible with the electron particle hypothesis. The corresponding energy deposit is estimated by extrapolating the track to the ECAL. The energy deposits of possible bremsstrahlung photons in the ECAL are localized by extrapolating a straight line tangent to the electron track from each tracker layer, where an emission of photons is most likely. Afterwards the energy deposits are combined to a 'super-cluster' and linked to the track.

Reconstruction of Muon Candidates

Muons are the only charged particles which can traverse through the whole detector. This property makes an identification and reconstruction easier and very precise. For the muon reconstruction mainly the tracker system and the four layers of the muon chambers are used. There are three different ways of reconstruction where two of them treat special kinematic cases of the muon. All three methods are based on an independent reconstruction of tracks in the silicon tracker and in the muon spectrometer. The most common technique is called Global muon reconstruction. With combination of calorimeter entries in the muon chambers and matching trajectories from the silicon tracker, a global muon track is fitted. In this analysis only global muons are requested. A more detailed description, also

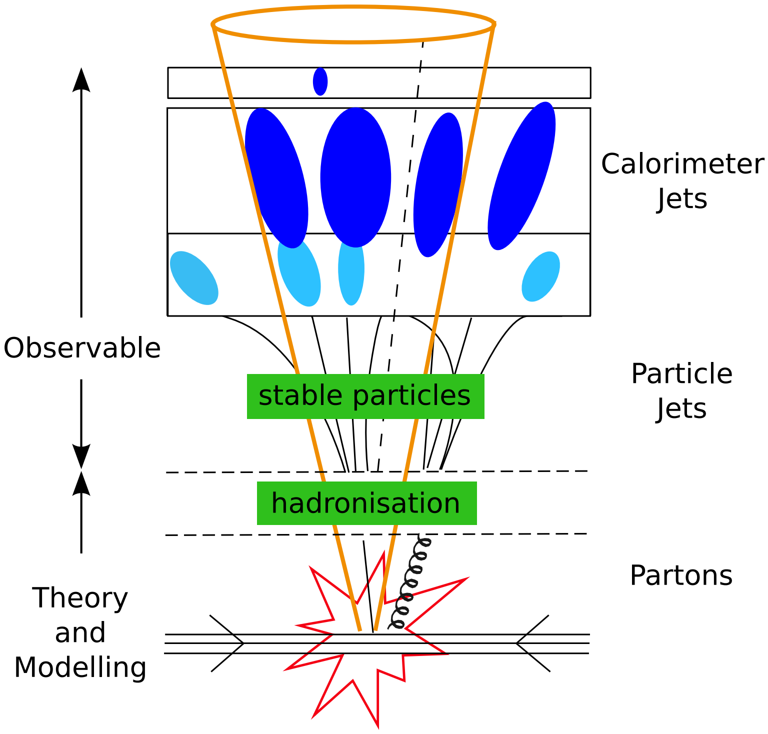

Figure 3.2.: Illustration of the evolution of a jet, taken from [36]. Energy deposits are marked as blue ellipses in the ECAL (bright) and HCAL (dark). They are used as input for jet reconstruction algorithms.

for the two other techniques, of muon reconstruction can be found in [72].

Reconstruction of Jets

Color charged particles obey the QCD confinement and therefore cannot be observed directly. A single colored particle hadronizes into several colorless hadrons which fly conically through the detector and leave a signature called a jet. In Fig. 3.2 the evolution of such a jet in the detector is shown. The jet reconstruction algorithm extracts the four-vector of the parton which took part in the hard scattering process and cluster all particles, which are produced in the hadronization.

In such a clustering algorithm all kind of physical objects can be considered, like simulated partons, generated stable particles after hadronization and decay or detector objects like calorimeter entries. Jets reconstructed from calorimeter information are called CaloJets. In contrast PFJets contain particles, which are all reconstructed with the PF algorithm. The jet clustering algorithm has to be aware of additional soft radiations, so called infrared safety, which should not change the number of jets in an event. High probability for a soft gluon emission in a hadron shower, soft contributions from the underlying event or noise of the electronics require this approach. Another important requirement is the collinear safety, i. e. the splitting of one particle into two particles with the same four-vector in total should not change the algorithms output.

Cone Algorithm

A cone algorithm like the iterative cone algorithm (ICONE) [43] is one of the commonly used clustering algorithms within the jet reconstruction. It clusters together all particles in a given cone with a fixed radius R in the $\eta - \phi$ plane. A proto-jet is build up from a particle with the highest transverse energy E_{T}, given by

$$E_{\mathrm{T}} = E \cdot \sin\theta \tag{3.1}$$

where E in Eq. (3.1) is the energy of the object and θ defines the azimuthal angle of its momentum vector. The current proto-jet is used as a seed for constructing the next proto-jet. The iteration stops when a certain criterion is reached, for example the jet axis changes, a lower energy threshold or a predetermined number of iterations is reached. A stopped iteration adds the proto-jet to the list of reconstructed jets and the algorithm regards only the remaining particles for a new iteration until no particles above a certain threshold remain. The collinear safety is not given since only seeds above a certain threshold are considered. An alternative would be to require no threshold at all, but this would take too much time for testing all subsets of cones. To solve this problem the *Seedless Infrared Safe Cone* (SISCone) [73] algorithm uses an advanced non-iterative method which succeeds in finding all stable cones in a convenient amount of time.

Sequential Clustering Algorithm

In addition to cone algorithms, one can choose sequential clustering algorithms which do not consider a geometrical shape of the reconstructed jet. Instead it uses the distance $d_{i,j}$ between two objects i and j, given by:

$$d_{i,j} = \min\left(p_{T,i}^{2n}, p_{T,j}^{2n}\right) \cdot \frac{(\Delta R)_{i,j}^2}{D^2}\ , \tag{3.2}$$

where $(\Delta R)_{i,j}^2 = (\eta_i - \eta_j)^2 + (\phi_i - \phi_j)^2$ describes the distance between i and j in the η-ϕ plane and $p_{\mathrm{T},i}$ is the transversal momentum of object i. Furthermore the resolution parameter D determines the size of the jet and n indicates a free parameter for different methods of the distance calculation. The distance to the beam $d_{k,\mathrm{beam}}$ of object k is given by:

$$d_{k,\mathrm{beam}} = p_{\mathrm{T},k}^{2n} \, . \tag{3.3}$$

For different parameters n the algorithm has a different naming:

- $n = 1$ K_T algorithm [74]
- $n = 0$ Cambridge-Aachen algorithm [75, 76]
- $n = -1$ anti-K_T algorithm [77]

The sequential clustering algorithm calculates the minimal distance $d_{i,j}$ between two objects i and j in every iteration and merges them to a new object, while removing i and j from the event afterwards. If the smallest distance of a particle to an object is the one to the beam, the object is removed from the event and added to the list of jets. This procedure is repeated until all objects are included in reconstructed jets.

These algorithms fulfill the infrared and collinear safety requirement. The currently used algorithm for CMS event reconstruction is the anti-K_T algorithm with a radius of 0.5.

At CMS, three different reconstruction approaches are used, meaning three different kinds of input variables are used for the jet reconstruction. Calorimeter jet reconstruction is based on the usage of calorimeter towers, which are the unweighted sum of all energy deposits in the ECAL and HCAL. This leads to the above-mentioned CaloJets.

The Jet Plus Tracks (JPT) algorithm [78] uses additional information from the tracker, in order to improve the transverse momentum resolution of CaloJets. To accomplish this, the information of corresponding charged particle tracks is added and matched to the CaloJets with respect to their distance in the η-ϕ plane and by the track momenta at the interaction point. An extrapolation of the track to the calorimeters indicates whether the track is an in-cone or out-of-cone track, meaning the track stays inside the jet cone or breaks through the surface of it, respectively. With this additional information the momentum of the tracks are added, or in case a track corresponds to a charged pion, subtracted. As a last step, the jet axis of the CaloJet is corrected.

The aforementioned PFJets take reconstructed PF objects as input for the jet reconstruction. All information of the sub detectors is used for each PF object and they have already been classified as particles with certain kinematics. Taking these objects as input for the PFJet reconstruction method improves the jet clustering, e. g. the transverse momentum resolution of the jet, as shown in Fig. 3.3. PF particles which not loose their energy in the HCAL and therewith are not “jet particles”, like global muons, are removed from the jet particle list.

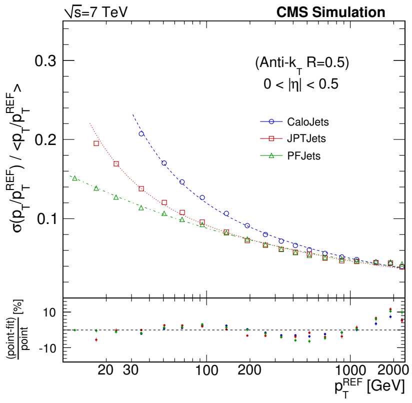

(a) (b)

Figure 3.3.: Transverse momentum resolutions of calorimeter, JPT and PF jets as a function of $p_{\mathrm{T}}^{\mathrm{REF}}$ for the ranges $0 < |\eta| < 0.5$ in (a) and $2 < |\eta| < 2.5$ in (b) [79]. p_{T} corresponds to the transverse momentum of the reconstructed jet and $p_{\mathrm{T}}^{\mathrm{REF}}$ to the transverse momentum of the matched generator jet. For PF jets the resolution improves in both η ranges.

Jet Energy Correction

The jet energy measurement is influenced by multiple sources, which distort the measurement. In order to correct for these effects the Jet Energy Corrections (JEC) are applied after the jet reconstruction. This correction process is divided into seven steps [80], namely Level 1 to Level 7 corrections, where each step treats another influence. The first three corrections handle instrumental and hardware based effects. The following four steps improve the estimation of the energy and momentum measurement of underlying partons. The first three jet corrections are applied for this analysis.

Level 1: The jet energy increases by electronic noise and pile-up collisions. In order to correct for this effect the FastJet corrections [81] are applied. They calculate the energy density ρ per unit area for each event. Afterwards the median of ρ is subtracted from the jet energy.

Level 2: The inhomogeneous detector layout in the η direction leads to η-dependent response of the calorimeters. Therefore, relative corrections are applied in order to equalize the jet response as a function of η to the jet response in the central region $|\eta| < 1.3$ [79].

Level 3: The calorimeter response depends on the transverse momentum of the jet. The Level 3 correction arranges a uniform calorimeter response with respect to the p_{T} value of the jet [79].

Level 4-7: Different electromagnetic fractions of the jets are corrected in Level 4. Level 5 corrects for flavor dependent effects, e. g. gluons have a higher probability for energy loss by radiation, than light quarks, which leads to lower calorimeter entries as necessary. Energy distributions from underlying event activity, which is assumed to be independent of the direction and energy scale of the hard interaction, is taken into account and correct in Level 6. Level 7 corrections look for possible differences in the energy of the initial parton and the corresponding jet.

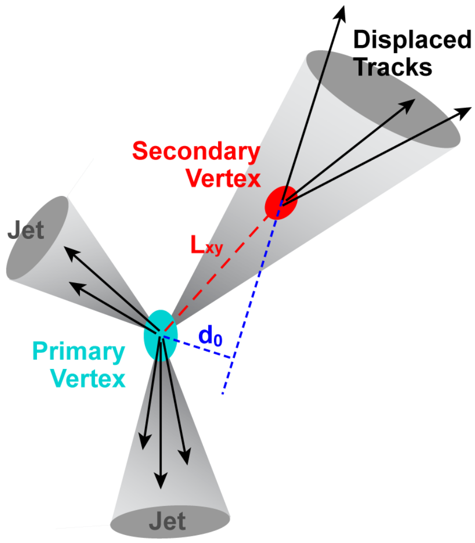

Figure 3.4.: Illustration of a collision event with a b jet, taken from [82]. The originated b quark forms bound states in terms of B hadrons. They predominantly decay via the weak interaction and therefore have a lifetime of typically $\tau \approx 1.6\,\mathrm{ps}$. This comparably long lifetime leads to a measurable covered distance L_{xy} of the B hadron before it decays. The resulting particles constitute a jet that has displayed tracks with respect to the primary vertex. Each displayed track has an impact parameter (IP), indicated as d_0 in the figure. Usually a primary vertex (PV) with a distance L_{xy} to the hard interaction point can be reconstructed from the displayed tracks. Many algorithms in the CMSSW software use L_{xy} and the IPs of the jets to identify b jets.

3.5.1. b Tagging

Many analysis contains events with b quarks in the final state, as well as this analysis does. Jets originated from a b quark are indicated by a shifted secondary vertex, since most often a b quark hadronizes into B hadrons which preferably decay via the weak interaction. Hence, they have a long lifetime compared to hadrons with lighter quarks ($\tau_B \approx \mathcal{O}(\mathrm{ps})$). This leads to a measurable distance between interaction point of the hard process and decay position of the B hadron ($c\tau \approx 460\mu\mathrm{m}$).

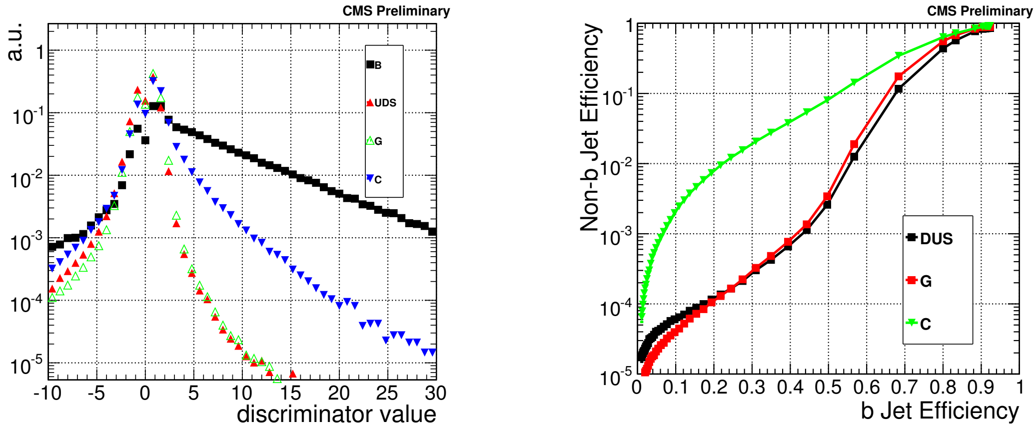

(a) (b)

Figure 3.5.: The diagram (a) shows the discriminator values for the TCHP b tagging algorithms for different jet flavors (light quarks UDS/DUS, gluons G, charm quarks C and bottom quarks B). In diagram (b) the mistag rates for the TCHP is shown [83].

The reconstructed tracks of such a jet are displaced from the primary vertex and implicate a variable called impact parameter (IP) (see Fig. 3.4). Usually a secondary vertex can be reconstructed within displaced tracks and give some indication for a decay of a B hadron. Algorithms that try to identify if a jet originates from a b quark are called b tagging algorithms. They can help to suppress a large amount of background events with jets induced by up, down or strange quarks and gluons. A schematic overview of a b jet is shown in Fig. 3.4.

The CMSSW software provides several b tagging algorithms [83]. All of them are optimized for having a high efficiency of identifying a b jet and simultaneously having a small mistag rate, meaning the efficiency for erroneously identifying a jet originating from a light quark as a b jet, is low. The diagrams in Fig. 3.5.1 show the discriminator values and mistag rates for the Track Counting High Purity (TCHP) algorithm, which is used in the presented analysis. This b tagger is based on the signed IP significance, which is defined as the ratio of the track IP over the track IP uncertainty. Found tracks, which are associated with jets, are ordered by their IP significance. The TCHP algorithm checks the third entry in this list and if it is above a certain threshold, the jet is claimed as b jet. The TCHP algorithm provides three working points for various kinds of tasks and analyses. Each WP corresponds to a certain mistag rate and is called loose, medium and tight WP. The discriminator values for this WP can be seen in Tab. 3.1, respectively. The commissioning of the THCP algorithm shows a remarkable agreement with the expectation based on samples of simulated events for the first collision data [84].

Table 3.1.: Working points of the TCHP b tagging algorithm and the corresponding discriminator value thresholds. Additionally the b tagging efficiency is shown [84].

Algorithm	WP	Discriminator Value	Mistag Rate	Efficiency
	loose	1.19	0.1	0.404
TCHP	medium	1.93	0.01	0.303
	tight	3.41	0.001	0.233

Missing Transverse Energy

The colliding protons have initially only a momentum in parallel to the beam axis. Hence, momentum conservation forces the transverse momentum to be conserved in each event. This characteristic can be used to get indications for neutrinos or other weakly interacting particles, which are not interacting with the detector itself, but leave an imbalance of the total transverse momentum. This imbalance is called Missing Transverse Energy (MET or $\vec{\not{E}}_{\mathrm{T}}$) and is defined as the negative vectorial sum of all transverse energy deposits in the calorimetry systems [85], given by

$$\vec{\not{E}}_{\mathrm{T}} = -\sum_{n=1}^{N} \left(E_n \sin\theta_n \cos\phi_n \hat{x} + E_n \sin\theta_n \sin\phi_n \hat{y} \right) , \tag{3.4}$$

where N is the total number of calorimeter input objects and $\hat{x}$ and $\hat{y}$ are the unit vectors in the x and y direction, respectively. In order to get a reliable MET value at the end, it has to be corrected to avoid miscalculation because of undetected escaped particles close to the beam line, or detector malfunctions, like dead sensors or poorly instrumented detector regions. Within the correction of MET the jet energy corrections are applied to the reconstructed jets as well. The corrected MET is given by

$$\left(\vec{\not{E}}_{\mathrm{T}}\right)_{\mathrm{corr}} = \vec{\not{E}}_{\mathrm{T}} - \sum_{i=1}^{N_{\mathrm{jets}}} \left(\vec{p}_{\mathrm{T},i}^{\,\mathrm{corr}} - \vec{p}_{\mathrm{T},i}^{\,\mathrm{raw}} \right) . \tag{3.5}$$

In Eq. (3.5) $\vec{p}_{\mathrm{T},i}^{\,\mathrm{corr}}$ and $\vec{p}_{\mathrm{T},i}^{\,\mathrm{raw}}$ are the transverse momenta of jet i before and after jet energy corrections. The corrections are only accomplished for jets with transverse momentum $p_{\mathrm{T}} > 10\,\mathrm{GeV}$ in order to avoid the large uncertainties for jets with lower p_{T}. Since the ECAL can accurately measure the energy of electrons, their energy deposits do not need to be corrected. However, muons, which deposit only a small amount of their energy in the calorimeters, can significantly disturb the MET determination. Therefore the transverse momentum of all muons is subtracted from the MET value. The correction for jet energy and muons is called Type-I correction. In addition there is an optional Type-II correction, which takes effects from pile-up and underlying event into account.

Related to the jet reconstruction, different input information can be used to calculate the MET value. The described MET determination with calorimeter entries is called caloMet. The track-corrected missing transverse energy (TCMet) reconstruction [86] uses additional information from the tracker. In this analysis the PFMet is applied. It takes all PF reconstructed particles and jets as input for the MET calculation (Eq. (3.4)), which makes the Type-I and Type-II corrections redundant. Fig. 3.6 is showing the improvement of using additional information for the determination of MET [87].

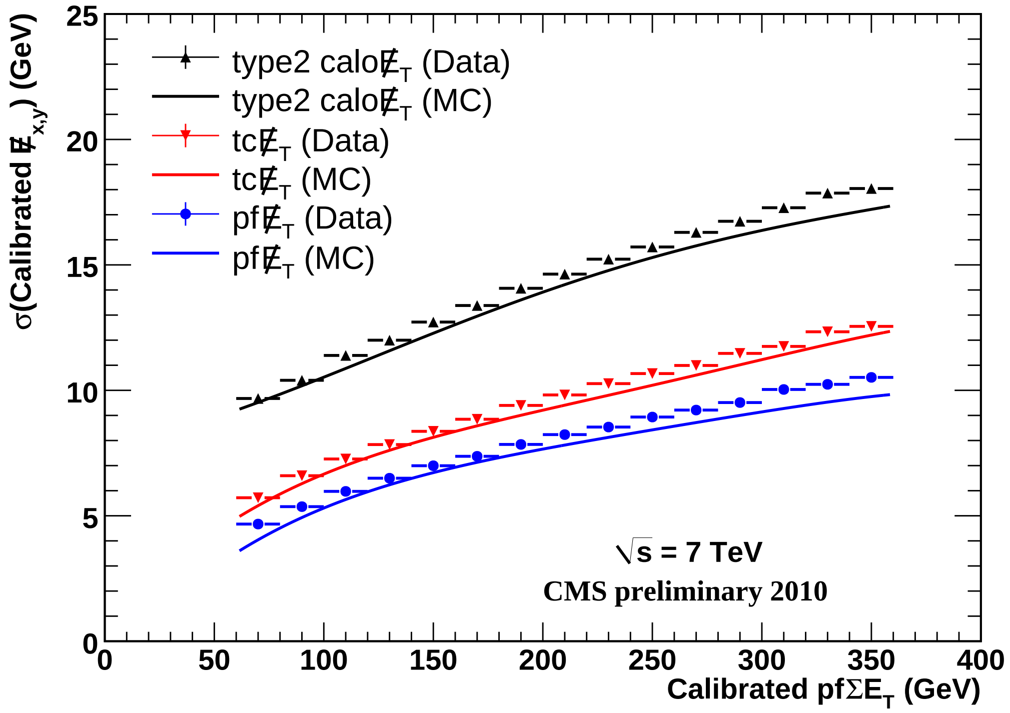

Figure 3.6.: Comparison of three different E_{T} calculations. Calibrated E_{T} resolution is shown versus calibrated E_{T} sum of particle flow objects [87]. Resolution values for Type-II corrected calorimeter-based (caloMet), track corrected (TCMet) and particle flow (PFMet) missing transverse energy in MC and data. The more information is used for the E_{T} calculation the merrier the resolution improves.

4. Event Selection

The focus of this analysis is on the single top quark t-channel process with an electron in the final state. The inelastic proton-proton cross section is around nine orders of magnitude higher than that of the single top quark t-channel production, as shown in Fig. 4.1. Moreover, many so-called background processes have the same final state as the signal process. Hence, appropriated selection steps are adopted on simulated events as well as recorded data events in order to maximize the signal-to-background ratio (S/B). These selection steps are tuned on MC events and aligned to the certain signal properties. This analysis focuses on a signal process, where the W boson from the top quark decays into an electron and an electron neutrino. Therefore the selection is based on the requirement of an isolated electron and the presence of missing transverse energy. The last selection steps cut on the number of PFJets and requiring b tagging for some of them. With a certain combination of different numbers of jets and b tagged jets, the analysis is split into six channels and allows a sophisticated estimation of the single top quark t-channel cross section at the end.

This section introduces the main background processes and the necessary selection steps to reduce them. In addition, the utilized MC and data samples are introduced. In Tab. 4.1 an overview of all simulated processes and their cross sections is given.

4.1. Background Processes

The single top quark t-channel production shares the final state with several other processes, which will be selected also although they are background. In recorded events the real interaction is unknown, whereas in generated events the actual process can be retrieved (MC truth). A comparison between both is the key to tune the event selection. The most important background processes are described in the following. Furthermore, there is another class of background processes due to mismodelled, misidentified or erroneously reconstructed objects. Such processes can lead to a final state that is similar to the signal process and contaminate the measurement as well.

4.1.1. Top Quark Production as Background

The $t\bar{t}$ cross section is about three times higher than the single top quark t-channel production cross section. Both top quarks decay into a W boson and a b quark. If

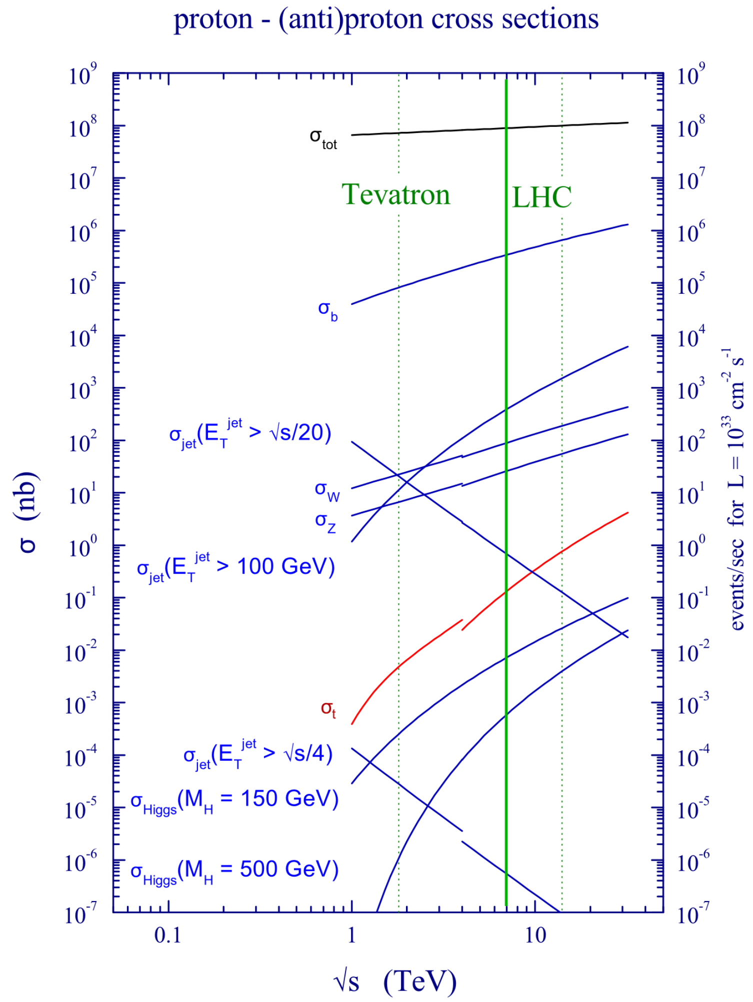

Figure 4.1.: NLO cross sections for several processes as a function of the center-of-mass energy $\sqrt{s}$, adopted from [88]. The cross sections for $p\bar{p}$ collisions are shown for $\sqrt{s} <$ 4 GeV and those for pp collisions for $\sqrt{s} >$ 4 GeV. The solid green line marks the current operating point of the LHC ($\sqrt{s} = 7$ TeV). The dashed green lines indicate the center-of-mass energy of the Tevatron ($\sqrt{s} = 1.96$ GeV) and the design value for the LHC ($\sqrt{s} = 14$ TeV), respectively. The total inelastic proton-proton cross section (black) is about nine orders of magnitude higher than the cross section of top quark production (red), requiring a selection to obtain a top quark enriched sample. Moreover, the cross section for vector boson production is two to three orders of magnitude larger compared to the $t\bar{t}$ production cross section.

one of the W bosons decays into leptons and the other into quarks, this process is called semileptonic decay. A semileptonic top quark pair decay occurs in $\sim 44\%$ of all cases. In this analysis only decays into electrons are taken into account, which reduces this rate to $\sim 15\%$. The relative contribution of this background increases with the number of selected jets. The LO Feynman diagram for $t\bar{t}$ production via gluon-gluon fusion and a subsequent semileptonic decay, is shown in Fig. 4.2. The inclusive $t\bar{t}$ MC sample is produced with MadGraph and showered with Pythia.

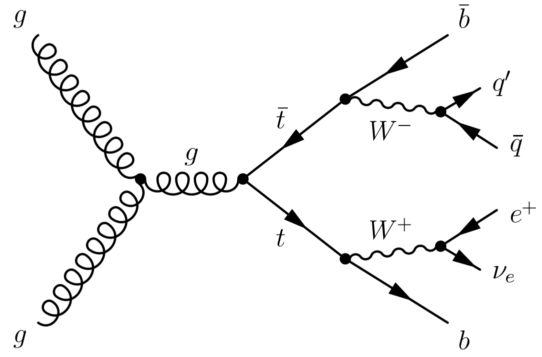

Figure 4.2.: LO Feynman diagram for $t\bar{t}$ production via gluon-gluon fusion. One of the W bosons decays in a $q\bar{q}'$, where the other decays in an electron and the corresponding neutrino. This decay mode is called semileptonic $t\bar{t}$ decay.

In addition, the single top quark production via s-channel and tW-channel are treated as background processes for this analysis. For the tW-channel a semileptonic decay is necessary to fake the final state of the signal. In Fig. 4.3 the Feynman diagrams are shown for these processes. Both processes have a relatively small cross section and do not have much influence on the measurement. The single top quark background processes are simulated with Powheg and showered with Pythia. There is a sample for top quark and anti-top quark production available. The tW production sample is determined with the diagram removal method (see Sec. 1.2). In Tab. 4.1 more details on the MC samples can be found.

4.1.2. Vector Boson Production

A large background process contribution is caused by the W and Z boson production in association with additional jets. The production modes induce light quarks and gluons or heavy quarks. Both production modes are shown in Fig. 4.4. If the W boson decays into an electron and the corresponding neutrino or a Z boson decays into an electron-positron pair, these processes can fake the topology of single top quark t-channel production. Z+jets production contributes to the background if one of the leptons from $Z \to e^+e^-$ was not reconstructed correctly. A strict b tagging requirement can reduce the W boson plus light flavor jets production significantly. Due to the large cross section and a non vanishing mistag rate, this background still has a large influence.

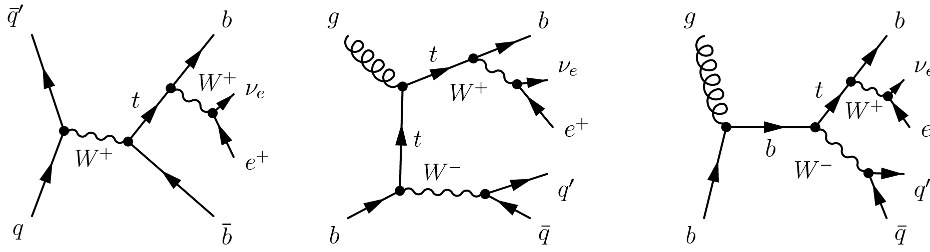

(a) (b)

Figure 4.3.: LO Feynman diagrams for the electroweak top quark production. The s-channel production is shown in (a). The associated production of top quarks is shown in (b). For the tW-channel a semileptonic decay is necessary. One of the W bosons decays in two quarks ($q\bar{q}'$), while the other decays in an electron and the corresponding (anti-)neutrino.

These background processes were produced with MadGraph and showered with Pythia. The renormalization scale and factorization scale is set to the W boson mass for the W+jets samples and to the Z boson mass for the Z boson sample. The W+jets sample is split into three parts: W+light jets (u,d,s,g), W+c jets and W+b jets. This separation gives a more detailed overview of the contributions of these subprocesses. The splitting is performed by accessing the MC truth of the selected jets and classify them afterwards. In Tab. 4.1 further details on the MC samples are listed.

(a) (b)

Figure 4.4.: (a) shows one Feynman diagram for the production of a W boson in association with quarks which are produced from a gluon radiation. The W boson decays in an electron and the corresponding neutrino. Usually the radiated gluon splits into a light quark anti-quark pair. With a b tagging criterion in the jet selection this background can be suppressed efficiently. The Z boson decays (b) into an electron-positron pair. With additional jets from a gluon radiation and a misidentification of one of the leptons these processes lead to a final state similar to that of the single top quark production.

4.1.3. Diboson Production

A small background contribution is added by production of diboson processes, namely WW, WZ and ZZ. Typical Feynman diagrams for these processes are depicted in Fig. 4.5. Events involving at least one W boson have a charged lepton, a neutrino and quarks in the final state, though they can directly fake the signal topology. In the ZZ production, where one Z decay leads to two leptons in the final state, one of these leptons has to get lost in the detector or has to be reconstructed wrongly to contribute to the background. The diboson processes are simulated with PYTHIA and the samples contain all decay channels, but all have a comparable small cross section. Details on the MC samples are listed in Tab. 4.1.

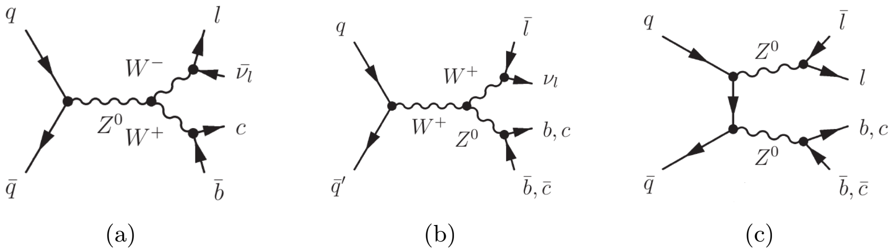

Figure 4.5.: Typical Feynman diagrams for diboson production: WW (a), WZ (b) and ZZ (c).

4.1.4. QCD Multijet Production

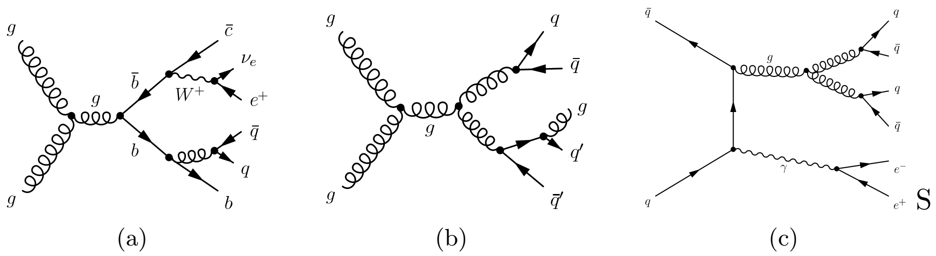

Figure 4.6.: Exemplary Feynman diagrams for QCD multijet production processes. In (a) the production of a $b\bar{b}$ pair via gluon-gluon fusion is shown. One b quark is hadronizing while the second b quark is decaying via the electroweak interaction. The resulting W boson decays leptonically into an electron and the corresponding neutrino. A final state with five jets via the QCD multijet production is presented in (b). If some of the jets fulfil the jet cut criteria and an electron is wrongly assigned to this event, the structure looks the same as in single top quark production. In (c) a real photon is emitted and it decays into an electron-positron pair. If one of these leptons is misidentified this process can be taken as signal.

A large background contribution originates from the QCD multijet production.

In Fig. 4.6 three QCD processes are shown exemplarily. In principle the final state of these processes contains only jets. Some of these jets can have the same kinematic values as the ones from the signal process, or even more unlikely, one of the jets is misidentified as an electron. In addition, electroweak interaction, e. g. a b quark decay, produces a W boson, which can decay into an electron and the corresponding neutrino.

In Tab. 4.1 some of the QCD multijet production samples are listed. Events in these samples can mimic electron+jets events and they are simulated in two separate non-overlapping phase spaces, leading to two different samples. Both samples are produced with Pythia. The BCtoE samples contain events where electrons arise from a b or c quark decay only. The EMEnriched samples contain events where the final state partons presumably become misidentified as electrons. Both types of samples are split into three parts, separated by $\hat{p}_{\mathrm{T}} = \sqrt{\hat{t} \cdot \hat{u} / \hat{s}}$. Herein $\hat{t}$, $\hat{u}$ and $\hat{s}$ represent the Mandelstam variables [89].

In Fig. 4.6(c) a multijet process with a real photon in the final state and additional jets is depicted. The photon probably interacts with the detector material and converts into an electron-positron pair. If one of these conversion electrons is misidentified or only one of them is reconstructed, this process can mimic the single top quark production as well. The MC sample if produced with Pythia and split into three parts. They differ in the $H_{\mathrm{T,Had}}$ variable, which describes the scalar sum of the transverse momenta of all final state quarks and gluons.

All QCD multijet production samples listed in Tab. 4.1 are quoted for the sake of completeness. The QCD background can be reduced efficiently with a cut on the missing transverse energy and on the electron isolation. Indeed the reduction is so large that almost no MC produced QCD event passes the whole selection. However, for a reliable background estimation this fact is impractical, because statistical fluctuations can determine the measurement. Hence, in this analysis the QCD background is estimated from recorded data events with a special electron selection (see Sec. 4.3.7).

4.2. Analyzed Data Sample

The analyzed data has been recorded by the CMS detector during the LHC pp operation in 2011 till June. All these events passed the HLT system (see Sec. 2.2), hence they are preselected in the sense of requiring already certain event criteria. This preselection is exploited to sort these events in primary data sets (PD). For this analysis the `SingleEle` data set and the `EleHad` data set are used. The `SingleEle` data set contains events triggered by requiring an electron as well as some isolation criteria using calorimeter information. The `EleHad` data set contains events selected by cross triggers, which require one electron in addition to a certain

Table 4.1.: Overview of the MC samples for this analysis. QCD and diboson samples were produced with PYTHIA. W+jets, Z+jets and $t\bar{t}$ samples were produced with MADGRAPH and showered with PYTHIA. The single top quark production samples are simulated with POWHEG and showered with PYTHIA. Leptonic decay modes include $l = e, \mu, \tau$. The effective cross sections σ_{eff} contain the branching ratio and filter efficiencies, if cuts were applied. N_{prod} is the number of produced events in the sample. The listed QCD samples are for the sake of completeness only, and give a general view to the cross sections for these processes. The QCD background is modeled from data with special electron cuts (see Sec. 4.3.7).

Process	Comments	σ_{eff} [pb]	N_{prod}
	Single top quark production		
t-channel (t)	inclusive	41.92 (NLO) [22]	3900171
t-channel ($\bar{t}$)	inclusive	22.65 (NLO) [22]	1944826
tW-channel ($t+\bar{t}$)	inclusive (DR)	15.74 (NLO) [24]	1624374
s-channel (t)	inclusive	3.19 (NLO) [90]	209971
s-channel ($\bar{t}$)	inclusive	1.44 (NLO) [90]	137980
	Top quark pair production		
$t\bar{t}$	inclusive	163.0 (NNLO) [20]	3701947
	Vector boson production		
W+jets	$W \to l\nu$	31314.0 (NNLO) [91]	54899972
Z+jets	$Z \to l^+l^-$	3048.0 (NNLO) [91]	36277961
WW	inclusive	43.0 (NLO) [92]	4225916
WZ	inclusive	18.2 (NLO) [92]	4265243
ZZ	inclusive	5.9 (NLO) [92]	4187885
	QCD multijet production		
BCtoE	$20\,\mathrm{GeV}/c \leq p_{\mathrm{T}} \leq 30\,\mathrm{GeV}/c$	132160 [92]	2243439
BCtoE	$30\,\mathrm{GeV}/c \leq p_{\mathrm{T}} \leq 80\,\mathrm{GeV}/c$	136804 [92]	1995502
BCtoE	$80\,\mathrm{GeV}/c \leq p_{\mathrm{T}} \leq 170\,\mathrm{GeV}/c$	9360 [92]	1043390
EMEnriched	$20\,\mathrm{GeV}/c \leq p_{\mathrm{T}} \leq 30\,\mathrm{GeV}/c$	2454400 [92]	361362246
EMEnriched	$30\,\mathrm{GeV}/c \leq p_{\mathrm{T}} \leq 80\,\mathrm{GeV}/c$	3866200 [92]	70708892
EMEnriched	$80\,\mathrm{GeV}/c \leq p_{\mathrm{T}} \leq 170\,\mathrm{GeV}/c$	139500 [92]	8069591
γ+jets	$40\,\mathrm{GeV} \leq H_{\mathrm{T,had}} \leq 100\,\mathrm{GeV}$	23620 [92]	2217101
γ+jets	$100\,\mathrm{GeV} \leq H_{\mathrm{T,had}} \leq 200\,\mathrm{GeV}$	3476 [92]	1065691
γ+jets	$200\,\mathrm{GeV} \leq H_{\mathrm{T,had}}$	485 [92]	1142171

number of jets per event.

The recorded data is separated into different runs, where each run indicates a time period in which the CMS detector has recorded data without interruptions. The runs are further divided into luminosity sections (LS). In an LS the instantaneous luminosity is considered to be constant. The data sets for this analysis cover the following run numbers:

`SingleEle:` runs 160431 to 163869

`EleHad:` runs 165088 to 167151

The Data Quality Monitoring (DQM) system [93] selects runs and LSs, which are considered to be good for physical analyses and lists them into a JSON file. For this analysis a filter is applied based on the JSON file `Cert_160404-167151-_7TeV_PromptReco_Collisions11_JSON` [94].

During the year of pp operation the instantaneous luminosity increased by a factor of 3. Consequently, triggers which apply relatively loose event criteria will select far too many events for saving. To avoid that, a trigger gets a certain prescale x, which means it selects only every x^{th} event. The consequence is a decreasing effective integrated luminosity when using this trigger. For physics analysis one tries to use as many events as possible, hence the choice of an unprescaled trigger is desirable.

4.3. Event Selection

In the following the event selection is described. All selection criteria have been chosen in order to reduce as many background events and keep as many signal events as possible.

For the analysis there are six different regions defined, called analysis channels. They differ in the number of selected jets and in the number of b tagged jets. The abbreviation xjyt stands for the channel with x selected jets where y jets are tagged by the TCHP b tagging algorithm at its tight working point (see also Tab. 3.1). For the 3j2t channel the number of b jets can be two or more. For all other channels the number of b jets is exact.

Single Top Quark Region: 2j1t, 3j1t

W+jets enriched Region: 2j0t, 3j0t

$\mathbf{t\bar{t}}$ enriched Region: 2j2t, 3j2t

The background enriched regions are introduced in order to check and estimate especially the W+jets and $t\bar{t}$ distributions, which are presumably selected in these phase spaces. The channels with exactly one b tagged jet have the largest signal over background ratio. All six channels are used for the final analysis.

4.3.1. Trigger

Table 4.2.: Overview of the applied triggers for the certain run ranges and primary data sets (PD). The analysis is split into different regions. The tagged regions require at least one b tagged jet. The quoted effective luminosity is calculated for the respective trigger. The untagged region is W+jets enriched. In the background enriched regions only the `SingleEle` data set is used, because the trigger in the `EleHad` data set are prescaled and do not contribute many events at all.

PD	Run Range	HLT trigger path	$\mathcal{L}_{\text{eff}}$ [pb]
	Tagged region (event has at least on b jet)		**920.7**
`SingleEle`	160404 - 163869	`HLT_Ele27_CaloIdVT_CaloIsoT _TrkIdT_TrkIsoT`	214.8
`EleHad`	165088 - 165969	`HLT_Ele25_CaloIdVT _TrkIdT_CentralJet30_BTagIP`	138.7
	165969 - 167151	`HLT_Ele25_CaloIdVT_CaloIsoT _TrkIdT_TrkIsoT_CentralJet30_BTagIP`	567.2
	Untagged region (event has no b jet)		**214.8**
`SingleEle`	160404 - 163869	`HLT_Ele27_CaloIdVT_CaloIsoT _TrkIdT_TrkIsoT`	214.8
`EleHad`	165088 - 165969	`HLT_Ele25_CaloIdVT_TrkIdT _CentralJet30`	3.5
	165969 - 167151	`HLT_Ele25_CaloIdVT_CaloIsoT _TrkIdT_TrkIsoT_CentralJet30`	30.1

This analysis is focused on a final state, where the single top quark decays into an electron via a W boson. Therefore, all triggers require already the presence of an isolated electron with a certain transverse energy in the central region ($|\eta| < 2.5$). For higher run numbers the `SingleEle` data set has no suitable unprescaled trigger available. In order to select as many events as possible the PD is changed to `EleHad` where unprescaled cross triggers are obtainable.

For the `SingleEle` data set a trigger, which requires an electron with a transverse energy larger than 27 GeV and certain identification requirements is applied. In the `EleHad` data set the triggers select an electron with a transverse energy larger than 25 GeV, at least one jet with a transverse energy larger than 30 GeV in the central region ($|\eta| < 2.4$) and at least on jet, which is identified as b jet by the TCHE algorithm at its medium WP. For the W boson enriched region, where no b tagged jet has to be selected, only the `SingleEle` PD is evaluated. The `EleHad` PD has no suitable unprescaled trigger available. In Tab. 4.2 all triggers, their run ranges and the corresponding effective luminosity is summarized.

4.3.2. Primary Vertex (PV)

Each event must have at least one good primary vertex. A reconstruction from at least four tracks ($n_{\mathrm{dof}} > 4$) is necessary. The maximum longitudinal distance $|z|$ from the PV to the nominal interaction point is 24 cm and the radial distance ρ_{PV} of the PV to the nominal interaction point is 2 cm.

4.3.3. Electron Selection

The electron candidates selected for this analysis have to fulfil several criteria. Their transverse energy has to be larger than 30 GeV, they have to pass the tracker in $|\eta| < 2.5$ and their supercluster must be located outside the region $1.4442 < |\eta_{sc}| < 1.5660$. This region defines the ECAL endcap-barrel transition region and is excluded due to the large amount of material an electron has to pass, which increases the probability to emit a large amount of energy via bremsstrahlung photons. In addition the absolute 2D impact parameter of the track with respect to the beam spot has to be smaller than 0.02 cm. An ensemble of several criteria is collected in the VBTF70 [95] requirement, which also has to be passed for an electron to be selected. Furthermore, the electron candidate has to be isolated, which means only a certain amount of activity (energy) is found around the track and in the calorimeters of the electron. This property is given by the relative isolation:

$$\mathrm{I}_{\mathrm{rel}} = \frac{\mathrm{E}_{\mathrm{Trk}} + \mathrm{E}_{\mathrm{ECAL}} + \mathrm{E}_{\mathrm{HCAL}}}{p_{\mathrm{T}}}\,, \tag{4.1}$$

where $\mathrm{E}_{\mathrm{Trk}}$ is the sum of the transverse momenta of tracks, excluding the electron track, with $p_{\mathrm{T}} > 1\,\mathrm{GeV}/c$ in a cone of radius $R = 0.4$ around the electron. The sum of the energy deposits inside the cone of radius $R = 0.4$ around the electron track is described by $\mathrm{E}_{\mathrm{ECAL}}$ and $\mathrm{E}_{\mathrm{HCAL}}$, respectively. An electron candidate for this analysis has to have $\mathrm{I}_{\mathrm{rel}} < 0.125$. Exactly one electron that fulfils all mentioned requirements is permitted per event.

In order to avoid events with additional charged leptons, two vetoes are applied. The first rejects events with additional isolated muons. Global muons with a transverse momentum $p_{\mathrm{T}} > 10\,\mathrm{GeV}/c$ within a pseudorapidity $|\eta| < 2.5$ and a relative isolation of $\mathrm{I}_{\mathrm{rel}} < 0.2$ are considered. Furthermore, an event with another electron is rejected as well. Only electrons that have at least a transverse energy of $E_{\mathrm{T}} > 15\,\mathrm{GeV}$ inside the pseudorapidity of $|\eta| < 2.5$ and $\mathrm{I}_{\mathrm{rel}} < 0.2$ are considered.

However, additional electrons can not only appear from the vertex itself but from conversions of photons. Taking this process into account a conversion veto that rejects events with such extra electrons has to be applied. The first part of this cut examines the number of hits of the electron candidate track in the innermost tracker layer. If no hit is encountered, the electron candidate is marked as a conversion electron and the event is rejected. The second part of this selection step searches for a partner track of the electron candidate track [96, 97]. If this track has the opposite curvature and deceeds a certain distance at the origin of the tracks to the original track the event is rejected.

4.3.4. Jet Selection

The selected jets base on PF objects and they are reconstructed with the anti-k_t algorithm with a cone size parameter of $D = 0.5$ (see Sec. 3.5). All jets are corrected with the first three levels of jet energy corrections. In order to avoid contributions from misidentified photons, electrons, pions or calorimeter noise, the fractions of charged electromagnetic, neutral electromagnetic and neutral hadronic energies must be less than 0.99, respectively. Further, the jet must have at least two constituents.

For this analysis events with exactly two or exactly three PFJets with $p_\mathrm{T} > 30\,\mathrm{GeV}/c$ and pseudorapidity $|\eta| < 4.5$ are selected, depending on the analysis channel. The large pseudorapidity range has to be considered due to the light quark jet, which is preferably emitted in the forward region.

4.3.5. Missing Transverse Energy Cut

The missing transverse energy (MET) is calculated with Eq. (3.4), using PF objects as input. In Fig. 4.7 the distribution for different backgrounds is shown for simulated events. For small MET values the dominant processes are QCD and Z+jets. Therefore, a cut of MET $> 35\,\mathrm{GeV}$ is applied to reduce such backgrounds.

4.3.6. b Tagging

Since the top quark decays into a W boson and a b quark, b tagging is applied to select events with a b jet. The track counting high purity (TCHP) algorithm is used with a discriminator value of 3.41 (tight WP, see Tab. 3.1). Depending on the number of b tagged jets the events are categorized into the different channels.

4.3.7. QCD Estimation from Data

As mentioned earlier on, the number of QCD multijet background events and the shape of distributions of kinematic variables for this process is estimated from data with a special electron selection (in this context it is called *antiele* selection). The advantage of this method is a more reliable estimation of the amount of QCD

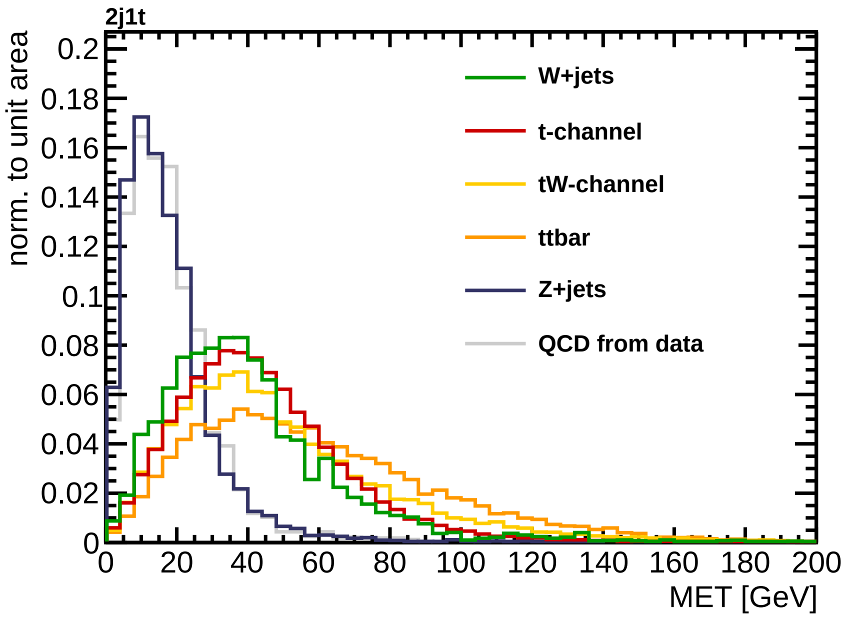

Figure 4.7.: Shape distribution of MET for the most important backgrounds and signal MC. QCD is modeled from data with a special electron definition. A cut at MET > 35 GeV reduces mostly QCD and Z+jets events.

background events, than taking it from MC generated events. Moreover, for data estimated events less systematic uncertainties have to be taken into account.

As well as in the standard electron selection (*refsel*) the transverse energy and the pseudorapidity for electrons are chosen to $E_{\mathrm{T}} > 30\,\mathrm{GeV}$ and $|\eta| < 2.5$. In addition the ECAL endcap-barrel transition region is excluded as before. The distinction is in the following three criteria:

- $\mathrm{I_{rel}} > 0.125$
- Impact parameter $d > 0.02\mathrm{cm}$
- fail the VBTF70 electron ID

If at least two of these criteria are fulfiled by the electron candidate the event is selected. Furthermore, the electron candidate has to have a relative isolation of $\mathrm{I_{rel}} < 0.5$ due to the HLT requirement. Especially the inverted relative isolation condition ensures an electron track that originates from a QCD process. Several checks have been done in order to ensure not to have a kinematic bias with this criteria. In Fig. 4.8 the shape of the MET is shown for both selections. Since the shape is the same, there is no kinematic bias found. Furthermore, the input variables were checked as well.

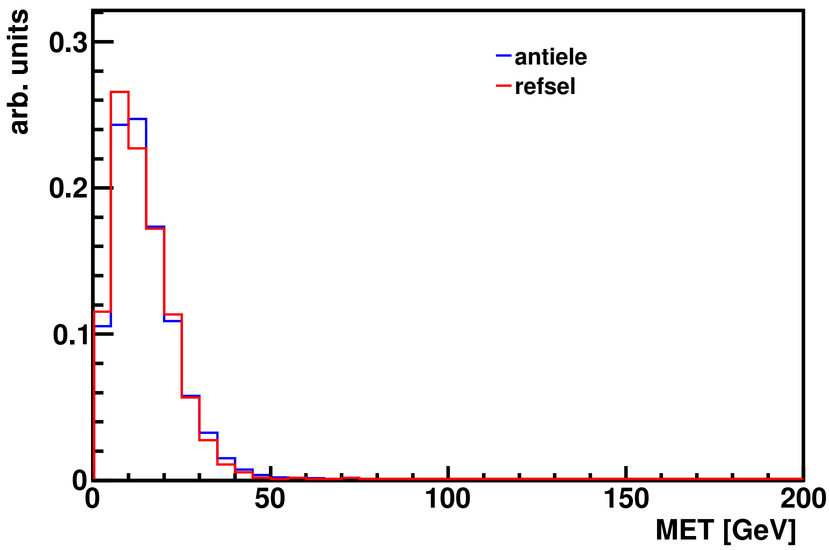

Figure 4.8.: Shape distribution of MET for the standard electron definition (*refsel*) and the QCD selection criteria (*antiele*). Both shapes have the same behavior. The QCD selection leads not to a kinematic bias.

The normalization scale factor for the QCD background is determined by a template fit to the MET distribution. The good separation power between QCD events and all other processes, shown in Fig. 4.7, is obvious. Ten processes showing a signal like MET distribution, i. e. $t\bar{t}$, W+jets (split into W+b, W+c and W+light) and all three single top production modes for t and $\bar{t}$, are added up according to the SM prediction and form one template for the fit. The Z+jets template is taken as an extra sample with a fixed parameter $\beta_{\mathrm{Zjets}} = 1$. The QCD template is taken from data with the inverted $\mathrm{I}_{\mathrm{rel}}$ condition. The overall distribution as measured in data is assumed to be composed of these twelve contributions and can be parametrized by:

$$F(MET) = \beta_{\mathrm{signal}} \cdot S(MET) + \beta_{\mathrm{QCD}} \cdot QCD(MET) + \beta_{\mathrm{Z}} \cdot Z(MET)\,, \tag{4.2}$$

where S(MET), QCD(MET) and Z(MET) are the expected distribution from signal-like events, QCD events and Z+jets events, respectively. A binned likelihood fit calculates $\beta_{\mathrm{signal}} = N_{\mathrm{fit}}/N_{\mathrm{pred}}^{\mathrm{signal}}$ and $\beta_{\mathrm{QCD}} = N_{\mathrm{fit}}/N_{\mathrm{pred}}^{\mathrm{QCD}}$ in order to match the number of all background events to the number of data events in each bin. The fit is performed in 20 bins for a range from $0\,\mathrm{GeV} < \mathrm{MET} < 100\,\mathrm{GeV}$ with the THETA framework [7]. The fit is performed for all of the six analysis channels. The β_{QCD} is applied for the analysis and all diagrams afterwards, the determined values for it are presented in Tab. 4.3. In Fig. 4.9 the results of the fit in each analysis channel are presented.

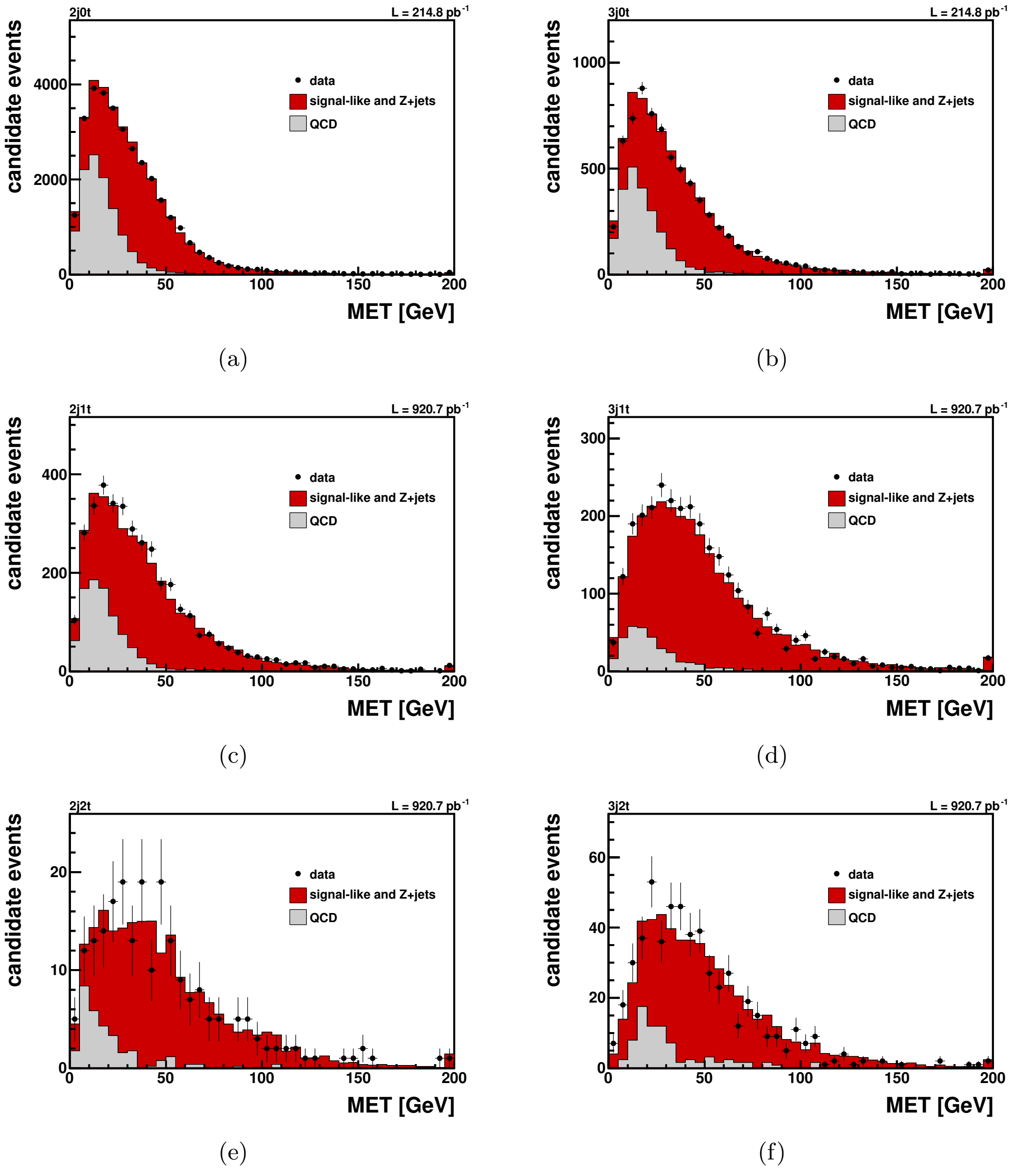

Figure 4.9.: Results for the template fit in order to estimate the QCD background. The fits are performed using the THETA framework [7]. All backgrounds, excluding the Z+jets template, are treated as signal like processes. The fit is performed in every analysis channel.

Table 4.3.: The results with statistical uncertainty of the binned likelihood fit to the MET distribution. β_{signal} represents the rate of all templates, which show a signal-like distribution.

Channel	β_{signal}	β_{QCD}
2j1t	1.07 ± 0.03	0.28 ± 0.02
3j1t	1.18 ± 0.03	0.32 ± 0.05
2j0t	1.35 ± 0.01	1.64 ± 0.03
3j0t	1.58 ± 0.03	1.71 ± 0.06
2j2t	1.18 ± 0.11	0.19 ± 0.07
3j2t	0.94 ± 0.07	0.80 ± 0.02

4.4. Corrections to Monte Carlo Events

The event generators have not yet simulated all effects that appear in a recorded event, i. e. the number of pile-up events and the influence of the HLT. The applied corrections to MC events adjust for such effects and are accomplished by giving each MC event a weight to match the observed data.

4.4.1. Pile-up Reweighting

The provided pile-up scenario from MC generators does not cover the observed pile-up conditions in the 2011 data taking period at LHC. Therefore, a pile-up reweighting is applied in order to adjust the pile-up distribution in MC events to that from recorded data [98]. Within these corrections each MC event gets an event weight according to the number of simulated pile-up events.

4.4.2. Simulation of Triggers

Since the HLT paths applied on the `EleHad` data set are not simulated in the generated events, their influences have to be modeled separately. The HLT cross trigger consists of two parts, a leptonic part, requiring at least one electron satisfying certain criteria and a hadronic part, requiring a given number of well-defined jets. The efficiencies of both parts of the trigger are assumed to factorize. The electron part will contribute to an event weight since the trigger cut for the transverse energy of the electron of 25 GeV is well below the offline electron selection cut of 30 GeV. For this cut the trigger efficiency for the electron cut is assumed to be flat, and in case the efficiency is not 100 %, a global electron selection efficiency factor can be applied in a later step of the analysis.

For the simulation of the hadronic part of the trigger two facts have to be taken into account. Firstly, the cut for the transverse momentum of the jet is the same for online and offline selection ($p_{\text{T}} > 30\,\text{GeV}/c$) and secondly, the jet definition differs in online and offline selection. The trigger regards CaloJets, whereas the offline data looks for PFJets. Hence, there is no guarantee that all PFJets correspond to the same CaloJet. The selection efficiency of a single PFJet to be triggered by the CentralJet30 path of the HLT is measured and parametrized for different η regions with a Gompertz function:

$$\epsilon\left(p_{\mathrm{T}}\right) = a \cdot \exp\left(b \cdot \exp\left(c \cdot p_{\mathrm{T}}\right)\right) . \tag{4.3}$$

In Eq. (4.3) the parameters a, b and c are determined from a χ^2-fit to data, taken from a single muon trigger. The results are shown in Fig. 4.10.

The analysis channels require different numbers of jets. In every case more than one jet is selected in the offline cut, while the trigger selects at least on jet. In order to get the selection efficiency for the whole event, a combination of all possibilities of jet assignments have to be taken into account.

4.4.3. Jet Energy Resolution

Simulated events feature a better resolution for the transverse momenta of jets as it is observed in recorded data. This effect is estimated to be around 5% to 29% depending on the η value of the jet [99]. Each selected jet in the simulated events is matched to a generator jet and the difference between their transverse momenta is multiplied by a certain factor and propagated to the four vector of the reconstructed jet. The correction factor in dependency of η is shown in Tab. 4.4.

Table 4.4.: Scale factors for the jet energy resolution correction. The scale factor differs for different η values of the jet [99].

$\lvert\eta_{\mathrm{jet}}\rvert$	Scale Factor
$\lvert\eta_{\mathrm{jet}}\rvert < 0.5$	1.05
$0.5 < \lvert\eta_{\mathrm{jet}}\rvert < 1.1$	1.06
$1.1 < \lvert\eta_{\mathrm{jet}}\rvert < 1.7$	1.10
$1.7 < \lvert\eta_{\mathrm{jet}}\rvert < 2.3$	1.13
$2.3 < \lvert\eta_{\mathrm{jet}}\rvert$	1.29

4.4.4. *b* Tagging Scale Factors and Efficiency

It turns out that the b tagging algorithm performs differently on recorded and simulated events [100]. In order to correct for this effect, scale factors for three categories of jets (b jets, c jets and light quark jets), are introduced and applied to the jets in simulated events.

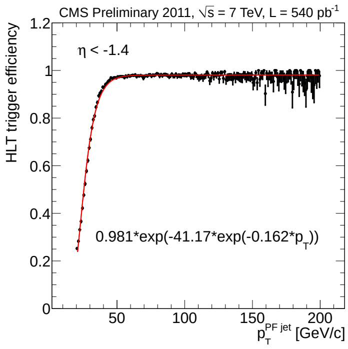

(a)

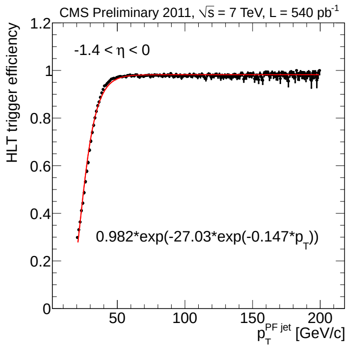

(b)

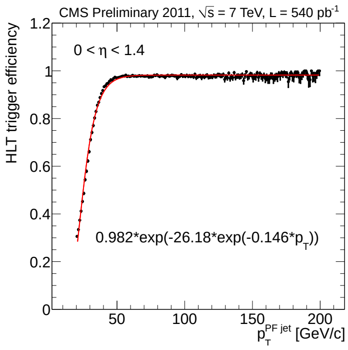

(c)

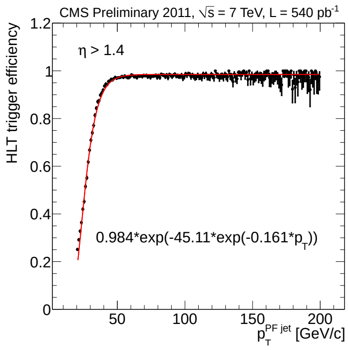

(d)

Figure 4.10.: Trigger turn-on curves for a single PFJet to be accepted by the CentralJet30 trigger as function of the transverse momentum of the jet in the pseudorapidity regions $\eta < -1.4$ (a), $-1.4 < \eta < 0$ (b), $0 < \eta < 1.4$ (c) and $\eta > 1.4$ (d). Since the selected jets in this analysis are required to posses a p_T larger than $30\,\mathrm{GeV}/c$ the functions given in the diagrams are used to calculate the probability of a simulated event to pass the HLT used on data.

In addition, the TCHP b tagging algorithm has a certain mistag rate, meaning a non b jet is identified as a b jet. Furthermore, a certain b tagging efficiency is given for this algorithm, describing the actual rate of identifying a b jet correctly. This efficiency can vary for each MC sample and has been determined for each MC sample. The b tagging efficiency is determined by counting the number of identified b jets divided by the total number of b jets in each MC sample. The mistag rate is examined similarly: Counting the number of jets, which are erroneously identified as b jet divided by the total number of jets gives the mistag rate for that jet category. For each event a weight is introduced which corrects for this efficiency. For a certain number of jets and b jets in the selection all combinatorial possibilities are taken into account.

4.4.5. Event Yield

In Tab. 4.5 the number of selected weighted events (normalized to $1\,\mathrm{pb}^{-1}$) are presented for all processes. In order to compare the number of selected events in data to all MC event rates, they are multiplied with the luminosity of $\mathcal{L} = 920.8\,\mathrm{pb}$. The expected signal to background ratio for the 2j1t channel is $S/B = 18.3\%$ and $S/B = 7.1\%$ for the 3j1t channel.

Table 4.5.: The number of expected events after the selection in $\mathcal{L} = 920.7\,\mathrm{pb}$ in the channels with b tagged jet and $\mathcal{L} = 214.8\,\mathrm{pb}$ for the channels with no b tagged jet. QCD is selected with an inverted $\mathrm{I_{rel}}$ cut in data.

	2j1t	3j1t	2j0t	3j0t	2j2t	3j2t
t-channel t	150.625	61.905	60.236	16.123	5.330	16.104
t-channel $\bar{t}$	86.687	34.730	32.971	8.543	3.167	8.880
s-channel t	16.145	6.391	4.382	1.186	4.092	1.866
s-channel $\bar{t}$	5.813	2.015	1.480	0.401	1.326	0.836
tW-channel	71.860	82.395	29.782	24.541	2.446	9.478
$t\bar{t}$	479.982	983.165	149.427	215.122	73.681	286.709
W+light	54.967	16.429	5626.17	986.648	0.297	0.111
W+c	251.937	73.719	1343.52	334.645	0	0.642
W+b	313.432	135.105	126.358	42.926	15.242	12.870
Z+jets	17.467	11.471	97.154	28.948	0.519	0.919
WW	6.611	2.844	78.237	17.167	0.061	0.157
WZ	7.090	2.773	18.074	4.616	1.046	0.575
ZZ	0.231	0.151	0.476	0.161	0.038	0.027
QCD from data	71.743	51.671	616.867	175.155	3.501	19.890
Total background	1296.277	1358.124	8091.927	1826.900	102.249	334.080
Total predicted	1533.589	1454.759	8185.134	1851.566	110.746	359.064
Selected Data Events	1652	1716	10185	2574	131	330

4.5. Top Quark Reconstruction

The top quark has to be reconstructed from its decay products for each event in order to have access to its 4-vector. Since the top quark decays into a W boson and a b quark, in the first step the W boson is reconstructed. In this analysis only W bosons are involved which decay into an electron and the corresponding neutrino. The x and y components of the missing transverse energy must originate from the neutrino. A constraint on the W boson mass is applied in order to calculate the z component of the neutrino momentum, $P_{z,\nu}$:

$$M_W^2 = \left(E_e + \sqrt{\mathbf{E}_{\mathrm{T}}^{\mathrm{miss}^2} + P_{z,\nu}^2}\right)^2 - (\mathbf{P}_{\mathrm{T},e} + \mathbf{E}_{\mathrm{T}}^{\mathrm{miss}})^2 - (P_{z,e} + P_{z,\nu})^2 \ . \tag{4.4}$$

There are in general two solutions for $P_{z,\nu}$:

$$P_{z,\nu}^{A,B} = \frac{\mu \cdot P_{z,e}}{P_{\mathrm{T},e}^2} \pm \sqrt{\frac{\mu^2 \cdot P_{z,e}^2}{P_{\mathrm{T},e}^4} - \frac{E_e^2 \cdot \mathbf{E}_{\mathrm{T}}^{\mathrm{miss}^2} - \mu^2}{P_{\mathrm{T},e}^2}} \ , \tag{4.5}$$

where

$$\mu = \frac{M_W^2}{2} + \mathbf{P}_{\mathrm{T},\mu} \cdot \mathbf{E}_{\mathrm{T}}^{\mathrm{miss}} \ . \tag{4.6}$$

In case the discriminant in Eq. (4.5) is positive, two real values for $P_{z,\nu}$ solve this equation. This occurs in 73.9% of all cases. The smallest value of $|P_{z,\nu}|$ is chosen. For this choice the ΔR distance between the real neutrino and the reconstructed neutrino is minimal in 61.2% of the cases.

For a negative discriminant of Eq. (4.5), $P_{z,\nu}$ gets an imaginary part, which happens if M_{T} is larger than the W boson pole mass of 80.4 GeV/c^2, mainly because the resolution of $\mathbf{E}_{\mathrm{T}}^{\mathrm{miss}}$ is finite (in 26.1% of all cases this occurs). In this analysis the components of the missing transverse energy are modified in the way that $M_{\mathrm{T}} = M_W$ and Eq. (4.4) is solved simultaneously [101]. $M_{\mathrm{T}} = M_W$ implies a vanishing radicand in Eq. (4.5) and leads to a quadratic equation for $P_{y,\nu}$ with dependence on $P_{x,\nu}$. Assuming that the true values of the neutrino momentum components are not too far away from the measured MET components, the distance δ between the missing transverse energy of the neutrino and the modified missing transverse energy is minimized with respect to the solutions $P_{y_{1,2},\nu}$:

$$\delta_{1,2}(P_{x,\nu}) = \sqrt{(P_{x,\nu} - (\mathbf{E}_{\mathrm{T}}^{\mathrm{miss}})_x)^2 + (P_{y_{1,2},\nu}(P_{x,\nu}) - (\mathbf{E}_{\mathrm{T}}^{\mathrm{miss}})_y)^2} \tag{4.7}$$

The smallest δ is chosen for the reconstruction of the neutrino momentum components in order to keep the transverse energy close to the measured $\vec{\not{E}}_{\mathrm{T}}$. The new values for $P'_{x,\nu}$ and $P'_{y,\nu}$ are taken for the calculation of the new real value of $P_{z,\nu}$.

The jet assignment, which jet originates from which quark, depends on the number of b tagged jets in the event. If two jets are selected there is the following assignment applied: If none or two b tags are required (2j0t, 2j2t) the most forward jet is chosen to be the recoiling light quark jet, respectively. The remaining jet is the jet stemming from the top quark decay. If the event has exactly one b jet, this tagged jet is assumed to be the b jet from the top quark decay (correct in 92.7% of the cases [27]). The other one is matched to the recoil light quark (correct in 89.6% of the cases [27]).

For the three jet selection the jet assignment is different. When b tagging was applied in the selection (3j1t or 3j2t) the jet with the lowest TCHP discriminator output is assumed to stemming from the recoiling light quark (correct in 83.1% of the cases). If no b tagging was applied (3j0t) the most forward jet is estimated to be the jet stemming from the recoiling light quark. In all channels the energy of the remaining two jets is taken to determine the invariant mass with the reconstructed W boson. The jet corresponding to the closest invariant mass compared to the top quark mass is assigned to be the b quark jet originating from the top quark decay. The other jet is assigned to be jet stemming from the second b quark. The assignment of all jets for all channels is shown in Tab. 4.6.

Table 4.6.: Matching of all reconstructed jets to the underlying final state partons in selected signal events. For the matching the jet and parton have a distance of $\Delta R < 0.3$.

Channel	Fraction
2j0t	64.8%
2j1t	85.3%
2j2t	51.9%
3j0t	42.5%
3j1t	62.8%
3j2t	71.5%

5. Neural Network Analysis

The previous chapter introduced an event selection in order to increase the signal contribution in the selected data set. Nevertheless, the selection in data selects only signal candidates and cannot distinguish between signal or background. Such a seperation is possible with a multivariate analysis (MVA), i. e. an artificial neural network (NN), a boosted decision tree (BDT) or a likelihood funktion (LF). They are all based on several kinematic variables as input and flag each event as more background like or more signal like. In this analysis a NN is trained with the NeuroBayes package [102, 103].

5.1. Neural Networks

Artificial neural networks try to mimic biological neural networks. Their neurons, called nodes, are ordered in different layers. The nodes in the first layer are called input nodes. Every input node of the i^{th} layer has a one direction connection (feed-forward) to the nodes of the $(i+1)^{\text{th}}$ layer. Layers which are neither the first nor the last layer are called hidden layers. The last layer of nodes is called output layer. In Fig. 5.1 an example of a three layer feed-forward NN is shown. Every connection has a specific weight which will be determined during the training process. If the weight between two nodes becomes too small the training process prunes the connection. The training is performed with simulated events in order to be able to access the MC truth and compare it to the NN output. A properly trained NN should be able to separate signal and background events on (unknown) recorded data events.

5.2. NeuroBayes

The NeuroBayes package provides a three layer NN with an automated and robust preprocessing of input variables. Moreover, the training is performed with a Bayesian regularization. The aim of the algorithm is to achieve an estimate of the conditional probability density $f\left(t|\vec{x}_i\right)$ for a given measurement vector $\vec{x}$ and the target variable t.

The input of the j^{th} node of the hidden layer is the sum of the output of all nodes i, with input x_i, in the previous layer multiplied with the weight ω_{ij} of the connection, respectively:

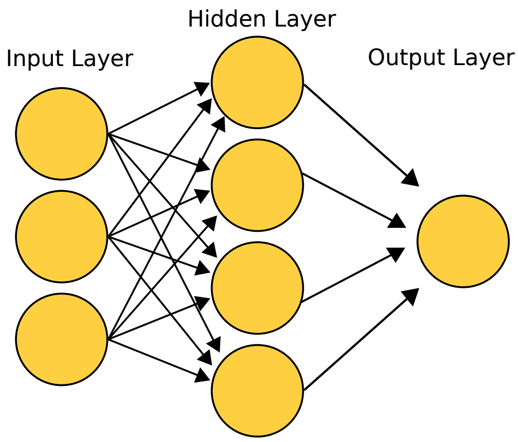

Figure 5.1.: A three layer Neural Network with an input, hidden and output layer. Each connection leads only in one direction and possess a specific weight, which is determined in the training process.

$$h_j(\vec{x}) = \sum_i \omega_{ij} x_i \tag{5.1}$$

A symmetric sigmoid function is applied as transfer function $S(x)$, in order to regularize the output from $]-\infty, \infty[$ to the interval $[-1, 1]$:

$$S(x) = \frac{2}{1 + e^{-h(x)}} - 1 \tag{5.2}$$

$S(x)$ from Eq. (5.2) is depicted in Fig. 5.2. The sigmoid function is mainly sensitive in the region around zero. A saturation is reached for very large or very small arguments of $S(x)$, hence outliers of the measurements are transfered close to -1 or 1 and the weighted sum of input values $\sum_i \omega_{ij} x_i$ is shifted to the linear region of $S(x)$.

The N outputs of o_j with 3 layers and M hidden nodes is given by:

$$o_j = S\left(\sum_l^M \omega_{lj}^{2\to 3} \cdot S\left(\sum_i^N \omega_{il}^{1\to 2} x_i\right)\right); \tag{5.3}$$

where the index l runs over all layer nodes. $\omega_{lj}^{2\to 3}$ is the weight of the connection between node l of the first and node j of the second layer and $\omega_{il}^{1\to 2}$ that between node l of the second and node i of the output layer.

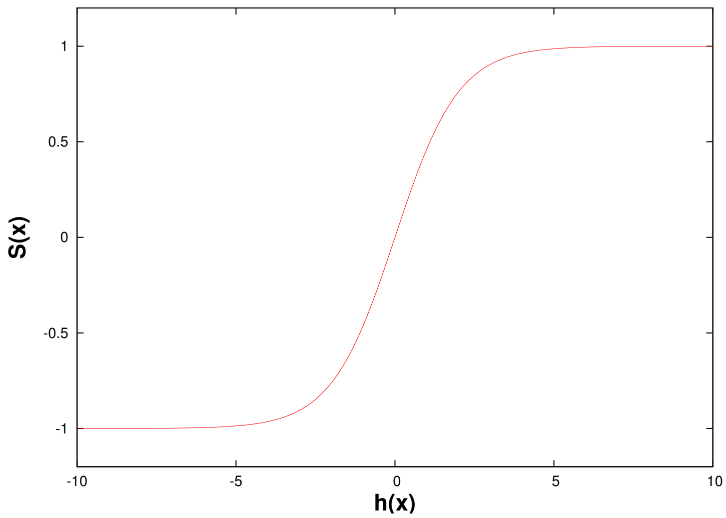

Figure 5.2.: The symmetric sigmoid function in the interval $[-10, 10]$. This function is applied as transfer function for each node of the NN.

5.3. Training

In the iterative training process the NN algorithm compares its output with the MC truth for each event. After a couple of events the weights on the connections will be adjusted in such a way, that the difference between NN output and MC truth is minimal. Therefore the weights are varied until an error function is minimized. A possible error function is the entropy error function, which is defined as:

$$E_D = \sum_{j,i} \omega_j \log \left(\frac{1}{2}(1 + T_{ji} \cdot o_{ji} + \epsilon) \right) . \tag{5.4}$$

In Eq. (5.4) T_{ji} and o_{ji} are binary values for the target and the output, respectively. These values are 1 in case of a signal event and -1 for background events. If the NN classifies an event completely wrong ($o_j = 1$ and $T_j = -1$, or vice versa) E_D in Eq. (5.4) becomes infinite. In order to avoid numerical problems at the beginning of the training, a small regularization constant ϵ is introduced. It gets smaller in every iteration step and vanishes at all after the training.

Since a minimum has to be found in a multi dimensional space, the minimization of the error function is a non-trivial problem. Therefore, a gradient descent method is applied, which changes each weight ω_{ij} proportionally to the gradient of the error function $\Delta\omega_{ij} = -\eta \frac{\partial E}{\partial(\Delta\omega_{ij})}$. η is the step width, which is adjusted individually for each weight. In addition NeuroBayes can use the Broyden-Fletcher-Glodfarb-Shanno (BFGS) method for minimalization. This method converges faster than the gradient descent method. The error for each weight is in this method back-propagated to the hidden layer from the output layer.

5.4. Preprocessing

A huge advantage of the NeuroBayes based NN is the preprocessing of the input variables. It automatically takes care of the correlations between the input variables, avoids the risk of overtraining and makes the training robust against statistical fluctuations. An overtrained NN has learned the events from training by heart and has no generality in classification for unknown events anymore.

In order to reduce statistical outliers in the input note all input variables are flattened and scaled to the interval $[-1, 1]$. A transformation into a Gaussian with a mean of zero and a width of one standard deviation ensures the output of the input nodes and the output of the hidden nodes not to be saturated. Instead of a Gaussian transformation also spline fits can be applied to the variables. Furthermore, the transformed variables are decorrelated in such a way that the covariance matrix of the set of input variables is given by the unit matrix. For this, the total correlation and the correlation matrix of all training variables to the target variable is calculated. In an iteration the remaining variable with the least correlation to the target is removed and the loss of correlation is calculated until the correlation for all variables to the target is known. By dividing the loss of correlation to the target by the square root of the sample size, the significance for every variable can be calculated. NeuroBayes provides the possibility to exclude variables for the classification, which have not reached a certain significance in the training.

5.5. Input Variables

For this analysis two different networks are trained in the single top quark enriched channels and applied also to the background enriched channels. For both networks the set of input variables is different. In general there are several variables available. A couple of final state quantities like p_{T} and η distributions from leptons, W boson, top quark and jets enter the networks. Furthermore there are combined variables like the Dijet mass and H_{T}. A third class of input variables are reconstructed quantities like the top quark mass and the transverse W boson mass. Further details to all input variables can be found in the following subsections. For the 2j1t channel 22 input variables are tested out of 30 variables, which were successfully used in a single top quark observation with a NN analysis at CDF [104]. In Tab. 5.1 the order of the used variables is shown. The most important variable is the η distribution of the light quark (η_{lq}). The recoiling light quark from the single top quark production is presumably found in the forward region of the detector. Background processes do not have this behavior. The second most important input variable is the reconstructed top quark mass ($M_{l\nu b}$). For single top quark events a clear peak in the distribution around the top quark mass is visible. Background processes show a longer tail to higher values of $M_{l\nu b}$. The shape for these two input variables is shown in Fig. 5.3. All input variables with a significance of $> 3\sigma$ for all 3 channels are shown in App. A.

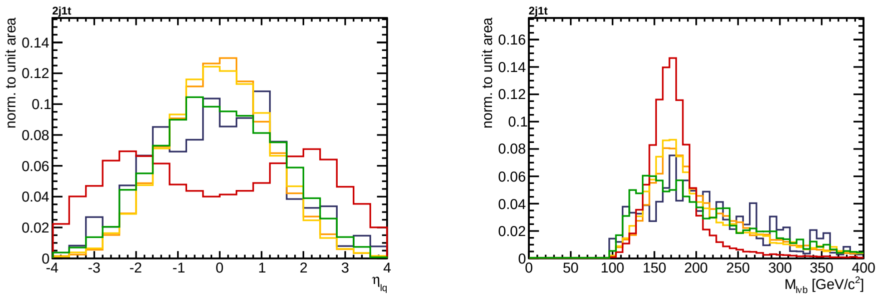

Figure 5.3.: The two most important input variables in the 2j1t analysis channel. Both variables show the clear separation power for signal and background processes.

For the 3j1t channel more variables were available. The training in this channel is performed with 30 variables. All input variables and the significance of the training is shown in Tab. 5.2. As well as in the 2j1t channel the η distribution of the light quark jet has the most separation power with the same shape distribution. The second most important variable in the 3j1t channel is the dijet mass of the hardest and the second hardest jet. The value of the dijet mass is mostly higher for single top quark events. The shape distributions of both quantities is shown in Fig. 5.4. All input variables with a significance of $> 3\sigma$ for all 3 channels are shown in App. B.

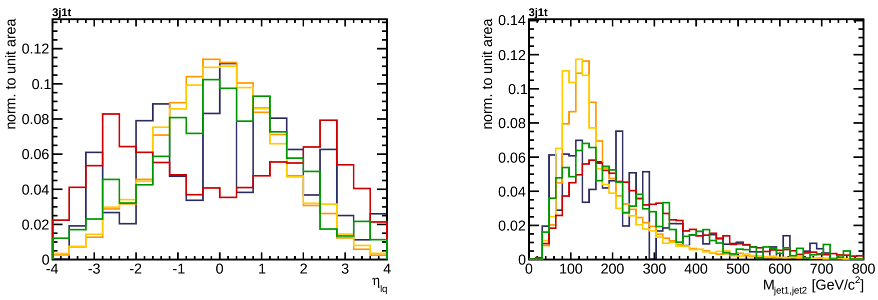

Figure 5.4.: The two most important input variables in the 3j1t analysis channel. Both variables show the clear separation power for signal and background processes. The statistic is low in this analysis channel which leads to the spiky structure.

Two trainings are performed, one in the 2j1t channel and one in the 3j1t channel. A weight for each training is applied, which provides a balanced number of signal and background events (50:50). For both NN only input variables with an additional significance of $> 3\sigma$ are taken into account for the classification. The correlations (before decorrelation) between these variables are shown in Fig. 5.5 and Fig. 5.6.

The network trained in the 2j1t channel will be also applied on the background enriched channels with two selected jets. The network has to demonstrate if especially W+jets and $t\bar{t}$ production can be assigned well. The same procedure is done in the three jet channels. One network is trained in the 3j1t region and applied on the 3j0t and 3j2t region. All six network outputs are used in the Bayesian approach to extract the signal cross section.

Both networks are trained with the following MC samples: single top quark t-channel production, $t\bar{t}$, W+jets and Z+jets. The available MC samples are split into two parts after the selection procedure. The first one consists of 70% of the events and is used for the training process. The remaining 30% of each sample is applied to check the NN for overtraining. All single top quark t-channel processes have a true target value, whereas for all background processes this value is false. In the App. A and App. B the input variables for the 2j1t and 3j1t analysis channel are depicted. Each input variable is illustrated in four figures. A shape comparison for the most important background processes and the signal is depicted in (a). This diagram demonstrates the separation power of the variable. The single top quark enriched region with one selected b tagged jet is shown in subfigure (b), respectively. The background enriched regions are presented in (c) and (d). The modeling of W+jets is shown in (c), which contains the region with zero b tagged jets. The fourth diagram (d) shows the $t\bar{t}$ enriched region with two selected b tagged jets. The legend for the code color of all diagrams is depiced in Fig. A.1. All diagrams for the signal top quark region (2j1t and 3j1t) are normalized to prediction. The excess of data is clearly visible. The control region diagrams are normalized to data.

5.5.1. Light Quark η

In both trained networks this variable has the most separation power. The recoiling light quark is presumably found in forward direction, which corresponds to high η values. In Fig. A.2(a) and Fig. B.2(a) this behavior is clearly visible. The background processes show a distribution around zero, where the signal has two maxima.

5.5.2. Reconstructed Top Quark Mass $M_{l\nu b}$

The reconstruction of the top quark for each event is described in Sec. 4.5. A sharp peak around $m_t = 173\,\mathrm{GeV}/c^2$ indicates the production of top quarks. For background processes the peak is broadened to higher values of $M_{l\nu b}$. The selected

b quarks for top quark pair production events in this region are not coming from the same top quark as the selected electron. If both W bosons decay leptonically, two neutrinos are produced, which disturbs the missing transverse energy measurement, which is necessary for the neutrino reconstruction. The W+jets background shows no peak at the top quark mass and decreases with a long tail to high values of $M_{l\nu b}$.

5.5.3. Invariant Dijet Mass

The invariant mass of two selected and reconstructed jets is calculated. The jets are ordered and numbered with decreasing p_{T} in each event. Signal events have a broader tail. Background events peak at a lower dijet mass and show a faster decreasing distribution.

5.5.4. Polarization Variable $\cos\Theta$

This variable shows the introduced top quark spin, which is visible in the angular correlations of its decay products (see Sec. 1.2). The angle Θ is defined as the angle between the direction of the electron and the light quark jet in the top quark rest frame. The shape for signal events shows the increasing behavior (see. Fig. A.7(a) and Fig. B.12(a)). Due to the isolation cuts on the electron the distribution drops for $\cos\Theta \approx 0.7$. The comparison of data and MC event is not perfect, especially for values of $\cos\Theta \approx -1$. Several background processes have been examined, but neither a different QCD selection nor W+x+jets distributions (x for heavy or light flavour) solved the mismodelling in this region. Nevertheless, this variable shows a high correlation to other input variables in the networks. Rejecting the variable from the training would not solve the issue entirely. Furthermore, the mismodelling only appears for low values of $\cos\Theta$, which has no influence to the signal process. The background processes will be estimated in the background enriched regions, where the mismodelling does not appear clearly. Allover, more studies are necessary, which are not part of this thesis. All background processes show a flat distribution in this variable. With it, single top quark t-channel production can be separated from associated production (tW).

5.5.5. Transverse W Boson Mass

The reconstructed transverse W boson mass is defined as:

$$M_{\mathrm{T,W}} = \sqrt{(p_{\mathrm{T},l} + p_{\mathrm{T},\nu})^2 - (p_{x,l} + p_{x,\nu})^2 - (p_{y,l} + p_{y,\nu})^2}\ , \tag{5.5}$$

where $p_{\mathrm{T},l}$ and $p_{\mathrm{T},\nu}$ are the transverse momenta of the charged lepton and the neutrino. In processes with a W boson, the distribution shows a Jacobian peak at the W boson mass of $80.4\,\mathrm{GeV}/c^2$. This variable discriminates between single top quark t-channel and $t\bar{t}$ due to a longer tail in top quark pair production.

5.5.6. Scalar Sum of Transverse Energies H_T

The scalar sum of $\vec{\not{E}}_T$, lepton p_T and all jet p_T is bundled in H_T. The main background processes and the signal process show different behavior in this variable and help to separate signal from background.

5.5.7. Angle ϕ Difference between Hardest Jet and MET $\Delta\phi_{\text{jet1,MET}}$

This variable describes the difference between the azimuthal angle ϕ of the jet with the highest p_T and the missing transverse energy. This variable shows a clear difference for events with a top quark and those without. Z+jets, QCD and Diboson events have a maximum around zero. In signal events the neutrino and the hardest jet are commonly back-to-back in the ϕ plane.

Table 5.1.: Applied input variables for the NN training and their significance in the 2j1t analysis channel. Only variables with an additional significance of $> 3\sigma$ are used for the NN classification.

	Variable	Additional Significance	Significance
1	Light Quark η_{lq}	38.65	38.65
2	$M_{l\nu b}$	29.52	36.93
3	$M_{T,W}$	16.18	23.12
4	$M_{\text{jet1,jet2}}$	14.28	25.52
5	W Boson η	7.86	7.05
6	$\cos\Theta$	6.80	19.41
7	H_T	4.52	19.22
8	$\Delta\phi_{\text{jet1,met}}$	4.56	1.83
9	Hardest Jet η	3.85	23.42
10	Lepton η	3.20	9.36
11	Neutrino η	2.20	9.04
12	Lepton p_T	1.27	20.74
13	$\vec{\not{E}}_T$	1.57	16.25
14	W Boson p_T	2.39	18.87
15	b Quark p_T	1.62	19.29
16	$\Delta R_{\text{jet1,jet2}}$	1.49	30.31
17	Neutrino p_T	1.26	17.19
18	Top Quark η	1.07	9.33
19	Top Quark p_T	1.22	5.35
20	Hardest Jet p_T	1.13	13.19
21	Second Hardest Jet η	0.44	22.19
22	b Quark η	0.11	4.82

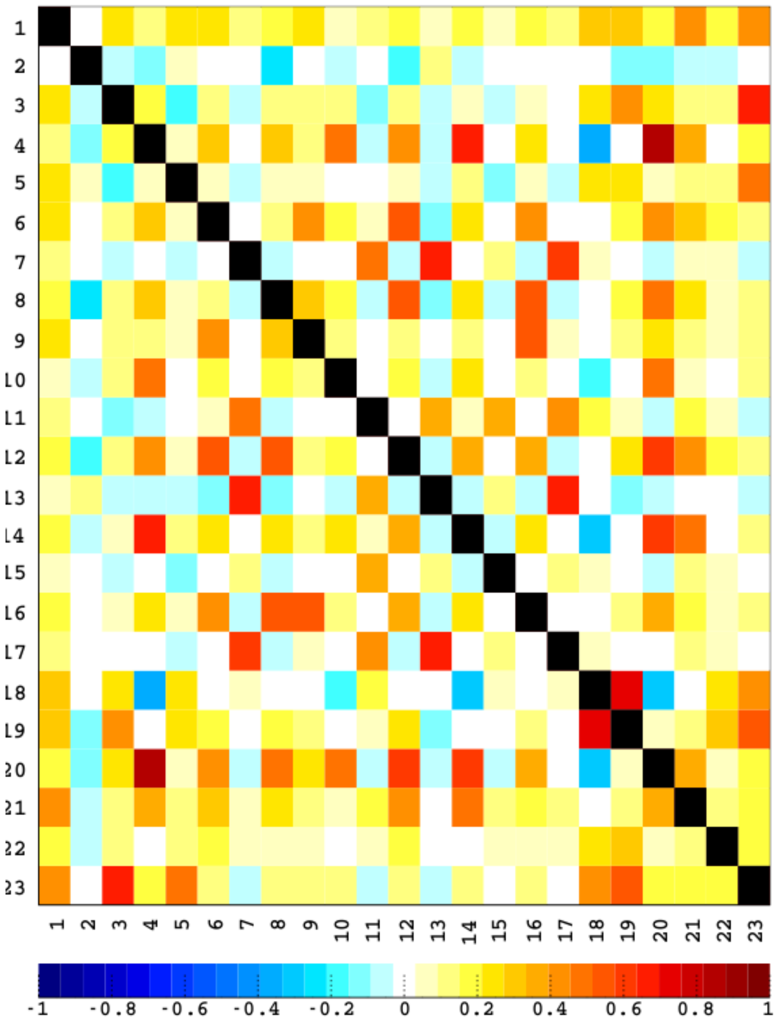

Figure 5.5.: Correlations of the input variables in the 2j1t analysis channel. The variable labeled with 1 is the target variable. The others are the input variables from Tab. 5.1 in the same order starting with 2 in the diagram.

Table 5.2.: Applied input variables for the NN training and their significance in the 3j1t analysis channel. Only variables with an additional significance of $> 3\sigma$ are used for the NN classification.

	Variable	Additional Significance	Significance
1	Light Quark η_{lq}	40.64	40.64
2	$M_{\mathrm{jet1,jet2}}$	17.93	25.57
3	H_{T}	20.46	17.80
4	$M_{\mathrm{jet1,jet3}}$	14.71	26.41
5	$M_{\mathrm{T,W}}$	11.33	18.36
6	$M_{l\nu b}$	10.96	17.99
7	$M_{\mathrm{jet2,jet3}}$	7.19	23.47
8	Second b Quark p_{T}	7.34	11.38
9	Second b Quark η	6.17	19.43
10	Lepton η	5.17	5.95
11	$\cos\Theta$	4.40	17.28
12	W Boson p_{T}	4.19	15.42
13	Top Quark p_{T}	4.65	8.98
14	b Quark p_{T}	3.63	10.77
15	Lepton p_{T}	2.30	17.64
16	$\vec{\not{E}}_{\mathrm{T}}$	3.31	12.82
17	Third Hardest Jet p_{T}	2.59	9.68
18	Third Hardest Jet η	2.68	20.95
19	Second Hardest Jet p_{T}	2.06	9.69
20	Second Hardest Jet η	1.77	21.83
21	Neutrino p_{T}	1.52	13.76
22	Neutrino η	0.53	5.74
23	Top Quark η	0.32	3.29
24	W Boson η	0.40	2.72
25	Hardest Jet p_{T}	11.35	0.32
26	$\Delta R_{\mathrm{jet1,jet3}}$	0.30	29.57
27	$\Delta R_{\mathrm{jet2,jet3}}$	0.31	23.70
28	$\Delta R_{\mathrm{jet1,jet2}}$	0.23	33.20
29	b Quark η	0.18	1.08
30	Hardest Jet η	0.22	25.35

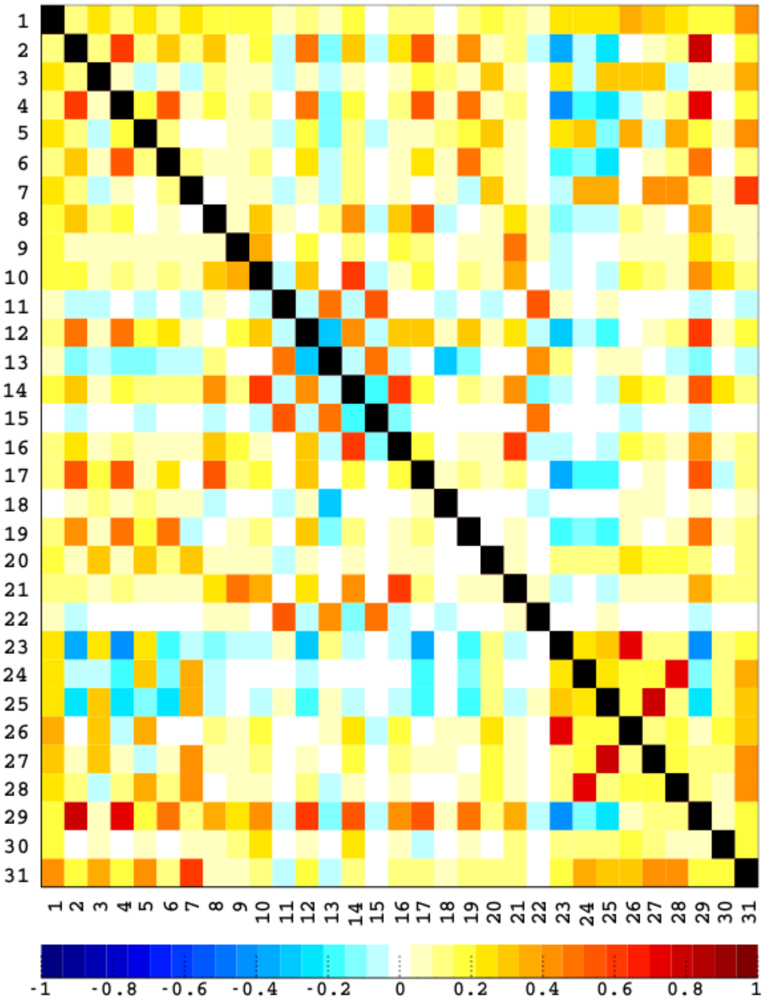

Figure 5.6.: Correlations of the input variables in the 3j1t analysis channel. The variable labeled with 1 is the target variable. The others are the input variables from Tab. 5.2 in the same order starting with 2 in the diagram.

5.6. Training Results

In Fig. 5.7(a) and Fig. 5.7(c) the NN output for both networks after the training is presented. A clear separation between background and signal events is obvious. Background events tend to negative output values, while signal events mostly have an output close to 1. For all processes the SM prediction is assumed. The dependence of the purity on the network output helps to judge the quality of the network training. The purity of a network output o is defined as:

$$P(o) = \frac{N_{sig}}{N_{sig} + N_{bkg}}\,, \tag{5.6}$$

where N_{sig} and N_{bkg} are the number of signal and background events. The output in dependence of the purity is shown in Fig. 5.7(b) and Fig. 5.7(d).

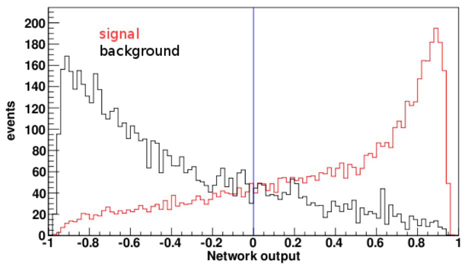

(a)

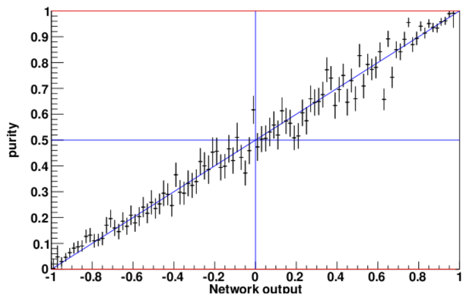

(b)

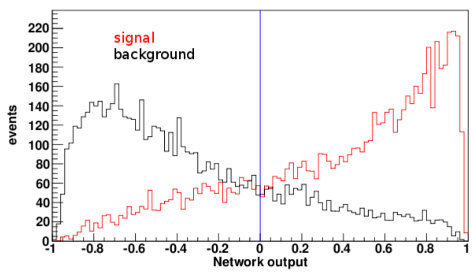

(c)

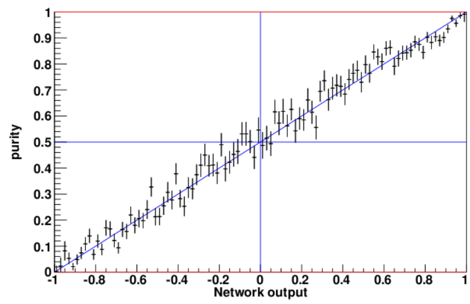

(d)

Figure 5.7.: Output of the NN for trainings events for the 2j1t analysis channel (a) and for the 3j1t analysis channel (c). The output for signal events is shown in red, background events are black. Both networks can clearly distinguish between signal and background events. Both NN give an output, which is proportional to the purity ((b),(d))

The output of the trained network for different processes is shown in Fig. 5.8(a) and Fig. 5.9(a). For background processes the output is very similar with an overhang to lower discriminator values. Signal events are classified mostly with higher output values. In the 3-jet channel the W+jets and Z+jets background have lost their clear background shape behavior. This is a statistical effect: only a few events pass the 3-jet channel selection and the training of the NN is influenced by this low statistic.

The results when applying the trained network on recorded and simulated events are presented in Fig. 5.8(b) and Fig. 5.9(b) for the single top quark regions. The accordance between both is good within the statistical uncertainties. Recorded events with an high NN output value seem to be single top quark t-channel events. The W+jets enriched regions (Fig. 5.8(c) and Fig. 5.9(c)) with zero selected b jets show a good agreement between data and MC events in the higher output value region. However, in the 2-jet channel the W+jets enriched sideband show a mismodeling for low NN output values. A reason for this mismodeling could be the mismodeled polarization angle of the top quark mentioned earlier on. The $t\bar{t}$ enriched regions (Fig. 5.8(d) and Fig. 5.9(d)) have a low number of events. Albeit, the MC can model the selected events within the statistical uncertainty.

Summarizing two NN, trained in the single top quark enriched region, can describe either this region as well as the background enriched regions which are W+jets and $t\bar{t}$ enriched. The following chapter describes the signal extraction with a Bayesian approach to this NN outputs in all six channels with systematic uncertainties.

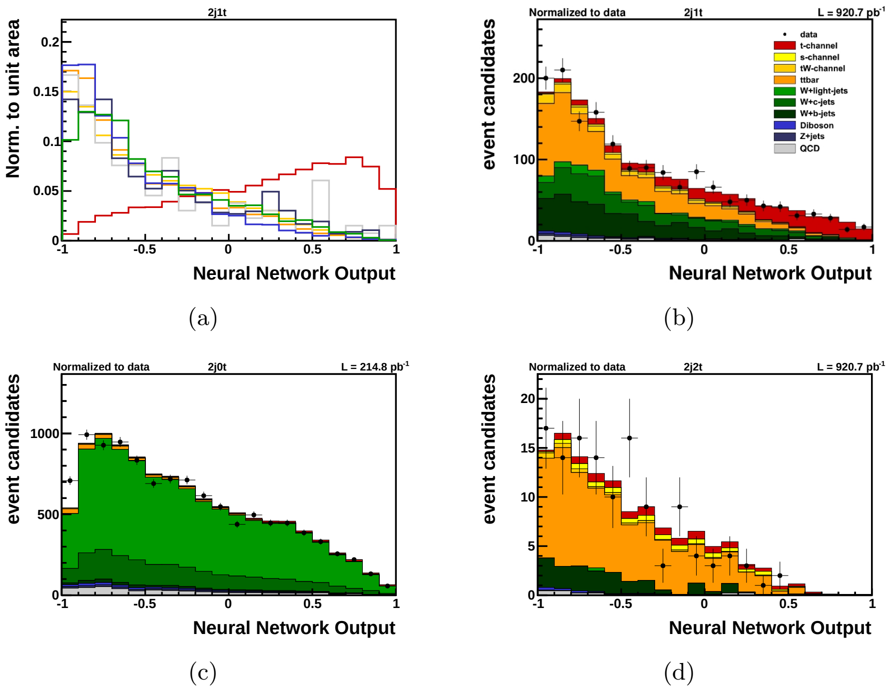

Figure 5.8.: Shapes for the 2j1t NN output for different processes (a). Outputs of the 2j1t NN for simulated events and data for the 2j1t (b), 2j0t (c) and 2j2t (d) channels.

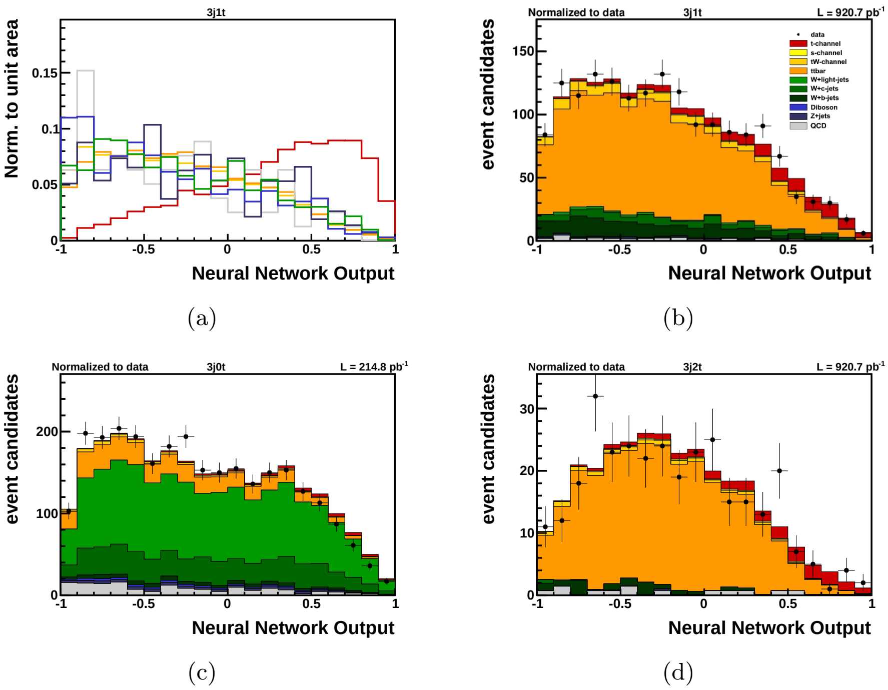

Figure 5.9.: Shapes for the 3j1t NN output for different processes (a). Outputs of the 3j1t NN for simulated events and data for the 3j1t (b), 3j0t (c) and 3j2t (d) channels.

6. Signal Extraction and Cross Section Measurement

The present analysis measures the cross section of the t-channel single top quark production with an electron in the final state in six different channels, which are: 2j0t, 3j0t, 2j1t, 3j1t, 2j2t and 3j2t. The cross section is extracted by constructing a likelihood function to the Neural Network output distribution for each channel. A product of these likelihood functions leads to a combined likelihood function for all channels. In the regions which are W+jets or $t\bar{t}$ enriched (zero b tag region and two b tag region) this method can estimate the shape and rate of these background processes. The influences of systematic uncertainties are considered in the likelihood function. The statistical evaluation of this analysis is performed with the THETA framework [7].

With the determined cross section the matrix element V_{tb} can be evaluated. The theoretical predicted cross section σ_{theory} is calculated using the fact that the matrix elements V_{td} and V_{ts} (see Eq. (1.2)) are very small. As a consequence, $|V_{tb}|^2$ is the proportional constant between σ_{measured} and σ_{theory}.

6.1. Statistical Method

To extract the signal cross section a Bayesian approach is applied. The posterior, which is defined as the product from the likelihood function and the prior, is determined using Neural Network outputs in all six analysis channels. The binned distribution of the NN is used for the statistical interference. The number of events in each bin is expected to follow a Poisson distribution, where the mean is given by the sum of all contributing processes. The likelihood function in Eq. (6.1) depends on the fit parameter $\beta_1 = \frac{\nu_1}{\nu_1^{\text{exp}}}$, where ν_1 is the number of estimated signal events and ν_1^{exp} represents the numbers of expected events in the examined distribution.

$$L_\lambda(\beta_1) := \prod_{i=1}^{N_{\text{bins}}^\lambda} \frac{\left(\mu_i^\lambda(\beta_1)\right)^{n_i^\lambda} e^{-\mu_i^\lambda(\beta_1)}}{n_i^\lambda!}\,, \tag{6.1}$$

where μ_i represents the number of expected events in the i^{th} bin of the NN output distribution of a certain analysis channel λ, and is given by:

$$\mu_i^\lambda(\beta_1) = \beta_1 \nu_1^{\mathrm{exp}} \cdot \left(\alpha_1^\lambda\right)_i \,, \tag{6.2}$$

with $\left(\alpha_1^\lambda\right)_i$ the fraction of selected events in the signal process predicted to be found in bin i of the channel λ. A result of $\beta_1 = 1$ represents the exact reproduction of the SM prediction for the single top quark t-channel production cross section. All six analysis channels are statistically independent, hence the combined likelihood function L is the product of the individual likelihood functions L_λ and depends always on the same β_1:

$$L(\beta_1) = \prod_{\lambda=1}^{6} L_\lambda(\beta_1) \;. \tag{6.3}$$

6.2. Systematic Uncertainties

Several systematic uncertainties are studied in order to present a reliable and comprehensive result. Two different types of uncertainties are taken into account: rate uncertainties, where the absolute number of events of the NN output changes and shape uncertainties, where the form of the NN output changes. For all six channels, the systematic uncertainties are incorporated separately into the statistical model by adding nuisance parameters to the model and hence to the likelihood function as well. For each systematic uncertainty u a new parameter δ_u is introduced parametrizing the intensity of the template variation by the uncertainty. Hence the dependencies of the number of expected events μ_i^λ in Eq. (6.2) and the likelihood function L in Eq. (6.1) enlarge with these parameters. The likelihood function for the examination of a channel λ is the product of Poisson terms for all bins of the distribution with the measured number n_i^λ and the predicted number μ_i^λ in the i^{th} bin for all processes:

$$\mu_i^\lambda = \mu_i^\lambda(\beta_1, \delta_1, \ldots, \delta_{N_{\mathrm{syst}}}) = \beta_1 \nu_1^{\mathrm{exp}} \cdot \left(\alpha_1^\lambda\right)_i + \sum_{u=1}^{N_{syst}} \delta_u \nu_u^{\mathrm{exp}} \cdot \left(\alpha_u^\lambda\right)_i \tag{6.4}$$

$$L(\beta_1, \delta_1, \ldots, \delta_{N_{\mathrm{syst}}}) = \prod_{i=1}^{N_{\mathrm{bins}}^\lambda} \frac{\left(\mu_i^\lambda(\beta_1, \delta_1, \ldots, \delta_N)\right)^{n_i^\lambda} e^{-\mu_i^\lambda(\beta_1, \delta_1, \ldots, \delta_N)}}{n_i^\lambda!} \cdot \prod_{u=1}^{N_{syst}} \mathcal{N}(\delta_u|\Delta_u) \tag{6.5}$$

The second term $\mathcal{N}(\delta_u|\Delta_u)$ in Eq. (6.5) is a log-normal with mean value 1 and a standard deviation of Δ_k :

$$\mathcal{N}(\delta_u|\Delta_u) = \frac{1}{\sqrt{2\pi}\Delta_u} \cdot \exp\left(-\frac{(\ln \delta_u - 1)^2}{2\Delta_u^2}\right), \tag{6.6}$$

where Δ_u represents the prior knowledge of relative rate and shape uncertainties of the systematic uncertainties.

For each uncertainty u commonly two alternative templates $\alpha^{\lambda}_{u,u,\pm}$, corresponding to $\pm 1\sigma$ deviations, are available and evaluated for each template α^{λ}_{u}. The templates are produced with a modification in a single initial condition concerning the systematic uncertainty, i. e. scale factors, which are applied in a certain selection step, are modified in that way, that their systematic or statistical uncertainty is added or subtracted, and the resulting new scale factor is used for further calculations. All other simulation, reconstruction and selection steps are retained. At the end two templates are accessible for each systematic uncertainty: an up and a down template with a single uncertainty shifted up or down. The template with the standard values is the reference for all systematic uncertainties. Exemplarily the jet energy resolution and jet energy scale systematic uncertainties are shape effect on the NN output is shown in Fig. 6.1.

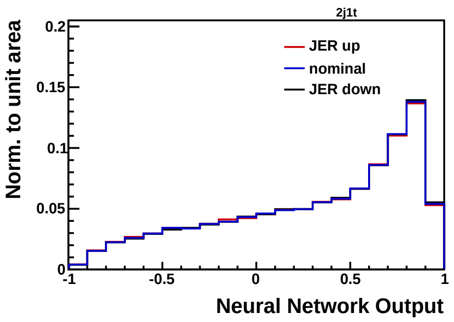

(a)

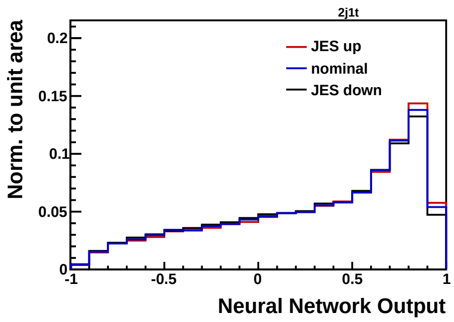

(b)

Figure 6.1.: In (a) the shape difference in the NN output of the jet energy resolution signal template between the nominal (blue), up (red) and down (black) variation. The same is shown for the jet energy scale uncertainty in (b). In both diagrams the distributions are normalized to unity in order to compare the form. Both systematic uncertainties show almost no shape discrepancies in the NN output for the signal process.

The prior knowledge of each parameter δ_u follows a normal distribution with mean $\mu = 0$ and standard deviation $\sigma = 1$:

$$\frac{1}{\sqrt{2\pi}} e^{-\frac{(\delta_u)^2}{2}} . \tag{6.7}$$

The posterior is the product of the Likelihood function and the prior distribution:

$$\tilde{L}(\beta_1, \delta_1, \ldots, \delta_{N_{\text{syst}}}) := L(\beta_1, \delta_1, \ldots, \delta_{N_{\text{syst}}}) \cdot \prod_{u=1}^{N_{\text{syst}}} \frac{1}{\sqrt{2\pi}} e^{-\frac{\delta_u^2}{2}} . \qquad (6.8)$$

The posterior $p(\beta_1, \delta_u|data)$ is given by the likelihood function L in Eq. (6.5). The parameter of interest is the β_1, therefore only the marginal distribution of β_1 of the full posterior is considered and is given by:

$$p(\beta_1|data) = \int p(\beta_1, \delta_u|data) d\delta_u . \qquad (6.9)$$

The marginal posterior is determined by a Markov-Chain Monte-Carlo (MCMC) method. The most probable value of this marginal posterior $p(\beta_1)$ provides the central value for the signal parameter β_1. The confident level for β_1 is found by evaluating the 68% credible level central interval of the posterior.

The estimation of the effect of the individual systematic uncertainties is determined with pseudo experiments as input. Exactly one source of systematic uncertainty is 'switched on' by setting all nuisance parameters to their nominal value and shift one nuisance parameter up and down. The signal cross section is set to the SM value of $\beta_1 = 1$.

The following sections explain the systematic uncertainties which are investigated in this analysis.

6.2.1. Jet Energy Resolution (JER)

As explained in Sec. 4.4.3 the resolution of the transverse momentum of jets is about 5% to 29% worse in recorded compared to simulated events. Therefore, the transverse momentum of the reconstructed jet is corrected with a factor, which depends on the η value of the jet. These factors are shown in Tab. 6.1 [99].

6.2.2. Jet Energy Scale (JES)

By varying all jet four momenta by either $+1\sigma$ or -1σ in their η and p_{T} dependencies simultaneously, the systematic effect of the jet energy scale is determined [105]. The JES variation is accomplished after applying the nominal JER correction of the MC samples.

6.2.3. *b* Tagging Scale Factor

As introduced in Sec. 4.4.4 the Track Counting High Purity (TCHP) b tagging algorithm requires a correction in the form of b tag efficiencies, mistag rates and scale

Table 6.1.: Scale factors for the jet energy resolution correction and its systematic uncertainties. The scale factor differs for different η values of the jet [99].

$\lvert\eta_{\mathrm{jet}}\rvert$	Scale Factor
$0.5 < \lvert\eta_{\mathrm{jet}}\rvert < 1.1$	1.05 ± 0.06
$0.5 < \lvert\eta_{\mathrm{jet}}\rvert < 1.1$	1.06 ± 0.06
$1.1 < \lvert\eta_{\mathrm{jet}}\rvert < 1.7$	1.10 ± 0.06
$1.7 < \lvert\eta_{\mathrm{jet}}\rvert < 2.3$	1.13 ± 0.10
$2.3 < \lvert\eta_{\mathrm{jet}}\rvert$	1.29 ± 0.20

Table 6.2.: Scale factors for the b tagging and its systematic uncertainties [84].

	Scale Factor
$\mathrm{SF_b}$	0.88 ± 0.088
$\mathrm{SF_c}$	0.88 ± 0.176
$\mathrm{SF_{light}}$	1.30 ± 0.200

factors. The measurement of the scale factors is described in [84]. The applied systematic uncertainties for the scale factors are shown in Tab. 6.2.

The $\mathrm{SF_b}$ is determined within a 10% systematic uncertainty. For the $\mathrm{SF_c}$ the systematic uncertainty is estimated to be 20% of the $\mathrm{SF_b}$ value. For the $\mathrm{SF_{light}}$ the systematic uncertainty is measured within a certain η dependency. In this analysis a systematic uncertainty is conservatively estimated to 0.2.

6.2.4. Factorization and Renormalization Scale Uncertainty

The simulated events depend on the factorization and renormalization scale, which has a default value in the samples (see Sec. 3.4). To quantify the influence of the scale choice two alternative MC samples for $t\bar{t}$, W+jets, Z+jets and all channels of single top quark production are utilized. In these samples, the event-by-event Q^2 scale is either shifted up or shifted down by a factor of 4.

6.2.5. Trigger Turn-on Uncertainty

In Sec. 4.4.2 the simulation of the cross trigger is explained. The parameters in the Gompertz function Eq. (4.3) are determined with a fit to data and are affected by a statistical and systematic uncertainty. Applying this function to MC events, a systematic uncertainty enters the analysis. Since the Gompertz function has three parameters, the fit provides a 3×3 covariance matrix for them in each η

range the parameters are determined. From the eigenvectors and eigenvalues of the covariance matrix one obtains three linear independent sets of parametrizations for the `CentralJet30` (ttojet) and the `BTagIP` (ttobtag) part of the trigger. For each eigenvector there are two alternative turn-on curves, one plus and one minus variation. The varied parameters are presented in Tab. 6.3 for the `CentralJet30` and in Tab. 6.4 for the `BTagIP` part of the trigger.

Table 6.3.: Values for parameters of the Gompertz function, which describes the trigger turn-on `CentralJet30` part. The eigenvalues and eigenvectors of the 3×3 covariance matrix can be described by three linear independent sets of parametrizations. For each eigenvector an up and down variation with the statistical uncertainties from the fit is applied. The resulting values for the parameters a, b and c from the Gompertz function in Eq. (4.3) are quoted.

`CentralJet30` part (labeled with ttojet$x$ whit Eigenvector set x)								
η range	par.	nominal	Eigenvector set 1		Eigenvector set 2		Eigenvector set 3	
			+	−	+	−	+	−
$\eta < -1.4$	a	0.981	0.981	0.981	0.982	0.980	0.981	0.981
	b	-41.17	-37.49	-44.84	-41.17	-41.17	-41.17	-41.17
	c	-0.162	-0.158	-0.164	-0.161	-0.161	-0.162	-0.161
$-1.4 < \eta < 0$	a	0.982	0.982	0.982	0.983	0.982	0.981	0.981
	b	-27.03	-27.51	-26.56	-27.03	-27.03	-27.03	-27.03
	c	-0.147	-0.146	-0.147	-0.147	-0.147	-0.146	-0.147
$0 < \eta < 1.4$	a	0.982	0.982	0.983	0.983	0.982	0.982	0.982
	b	-26.18	-26.63	-25.72	-26.18	-26.18	-26.18	-26.18
	c	-0.146	-0.145	-0.147	-0.146	-0.146	-0.146	-0.146
$1.4 < \eta$	a	0.984	0.984	0.985	0.982	0.980	0.981	0.981
	b	-45.11	-42.17	-48.05	-45.11	-45.11	-45.11	-45.11
	c	-0.161	-0.158	-0.164	-0.161	-0.161	-0.161	-0.160

6.2.6. Background Normalization

In order to account for imperfect knowledge of the background process cross sections for each background template a systematic uncertainty is introduced. These parameters concerning the rate uncertainty of the background processes. Background templates for $t\bar{t}$, W+jets (split into W+b, W+c and W+light), Z+jets, single top quark production (s-channel for top quarks and s-channel for anti-top quarks, tW-channel) and data estimated QCD multijet production enter the statistical inference. In total, nine individual background templates are provided for each analysis channel. In Tab. 6.5 the systematic rate uncertainties for the background samples are quoted.

Table 6.4.: Values for parameters of the Gompertz function, which describes the trigger turn-on `BTagIP` part. The eigenvalues and eigenvectors of the 3×3 covariance matrix can be described by three linear independent sets of parametrizations. For each eigenvector an up and down variation with the statistical uncertainties from the fit is applied. The resulting values for the parameters a, b and c from the Gompertz function in Eq. (4.3) are quoted.

`BTagIP` part (labeled with ttobtag$x$ whit Eigenvector set x)							
par.	nominal	Eigenvector set 1		Eigenvector set 2		Eigenvector set 3	
		+	-	+	-	+	-
a	0.844	0.850	0.839	0.824	0.865	0.838	0.851
b	-6.72	-6.35	-7.10	-6.72	-6.73	-6.73	-6.72
c	-0.72	-0.681	-0.759	-0.733	-0.707	-0.710	-0.73

Table 6.5.: Applied rate uncertainties to background processes.

process	uncertainty
$t\bar{t}$	$\pm15\%$
W+b jets	$\pm100\%$
W+c jets	$\pm100\%$
W+light jets	$\pm30\%$
Z+jets:	$\pm30\%$
tW-channel single top	$\pm13\%$
s-channel single top	$\pm15\%$
Diboson processes	$\pm30\%$
QCD	$\pm100\%$

6.2.7. Luminosity

The uncertainty on the luminosity used in the analysis has been taken from the absolute calibration of the luminosity measurement at CMS [30] and has a value of ±4.5%.

6.2.8. PDF and Matching Threshold Uncertainty

The systematic uncertainty concerning the parametrization of the PDF is not taken into account in this thesis. The systematic uncertainty of this effect is expected to be small since other anaylses have shown yet (i. e. [45, 106, 17]). A systemtic uncertainy in the low percentage level is a realistic estimation. For this Bayesian approach the effect will be even smaller because of the insitu constraint of the method.

The matching threshold uncertainty was not taken into account in this thesis as well. Usually two alternative templates with different thresholds for the matching between the hard process generated with MadGraph and the parton shower performed with Pythia are availabe. Since the samples were not available for this analysis yet, the influence is assumed from the experience of other analyses. Also the insitu constraint will reduce the small uncertainty of a low percentage value.

6.3. Results

In Tab. 6.6 the determined influences of the individual systematic uncertainties are quoted. The knowledge of the individual uncertainties is necessary in order to improve the analysis in the future. The statistical method is unchanged while the toy data is shifted with one uncertainty and compared to the nominal sample. To have an idea of the overall systematic uncertainty all up/down variations added quadratically. The higher value is quoted in Tab. 6.6. The fully Bayesian approach uses the full posterior and give a total uncertainty, including statistical and systematic uncertainty, hence with this determination one can estimate the influence of the systematic uncertainty for it self. The systematic uncertainty should be smaller than the total uncertainty of the Bayesian approach. The luminosity uncertainty has the most influence on the systematic uncertainties. Even though the rate systematic uncertainties for the W+jets samples are estimated very conservatively, the impact on the total σ measurement is small. The impact of the b tagging uncertainty is of the same order. Overall, a systematic uncertainty of 10.62% is determined by adding the individual uncertainties quadratically and symmetrizing it by taking the highest value.

The statistical uncertainty is determined by calculating the parameter β_1 with nominal samples on toy data. Taking the width of the distribution gives an estimation of the statistical uncertainty. It is determined to be around 8.7%. Overall, the uncertainty of the Bayesian approach is estimated to be $\sqrt{(10.62\%)^2 + (8.7\%)^2} \approx$ 13.7%.

Table 6.6.: Summary of individual uncertainties for up and down variation. All are quadratically added at the end, the highest value is the symmetric estimation of all systematics.

Systematic uncertainty	up variation	down variation
JER	0.33%	−0.70%
JES	−1.87%	0.65%
btagcb	−1.77%	1.74%
btaglight	−0.08%	0.25%
scale	−0.16%	0.89%
ttojet1	−0.16%	0.20%
ttojet2	0.15%	0.16%
ttojet3	−0.47%	−0.06%
ttobtag1	0.38%	0.04%
ttobtag2	1.97%	−2.01%
ttobtag3	0.96%	−1.02%
$t\bar{t}$ (rate)	1.38%	−1.41%
W+b jets (rate)	1.16%	−0.96%
W+c jets (rate)	−2.10%	0.83%
W+light jets (rate)	−0.08%	0.25%
Z+jets (rate)	0.35%	−0.40%
tW-channel single top (rate)	−0.32%	0.10%
s-channel single top (rate)	−0.17%	−0.04%
WW (rate)	0.11%	−0.10%
WZ (rate)	0.38%	0.19%
ZZ (rate)	−0.54%	0.33%
QCD (rate)	−0.73%	−0.75%
luminosity	−3.79%	4.24%
total systematic uncertainty	10.62%	
statistical uncertainty	8.7%	
total expected uncertainty	13.7%	

6.3.1. Cross Section

In order to extract the signal cross section the posterior is determined from data, with the following result for β_1 with $\pm 1\sigma$ intervals:

$$\beta_1 = 1.0935^{+0.1642}_{-0.1346} \,. \tag{6.10}$$

The posterior distribution within the one standard deviation interval is shown in Fig. 6.2. The measured value determines a 9% deviation from the expectation. The uncertainties cover the expected SM value $\beta_1 = 1$. Therewith, the result for the single top quark t-channel production cross section with an electron in the final state at a center-of-mass energy of 7 TeV and data corresponding to an integrated luminosity of $\mathcal{L} = 920.7\,\text{pb}^{-1}$ is:

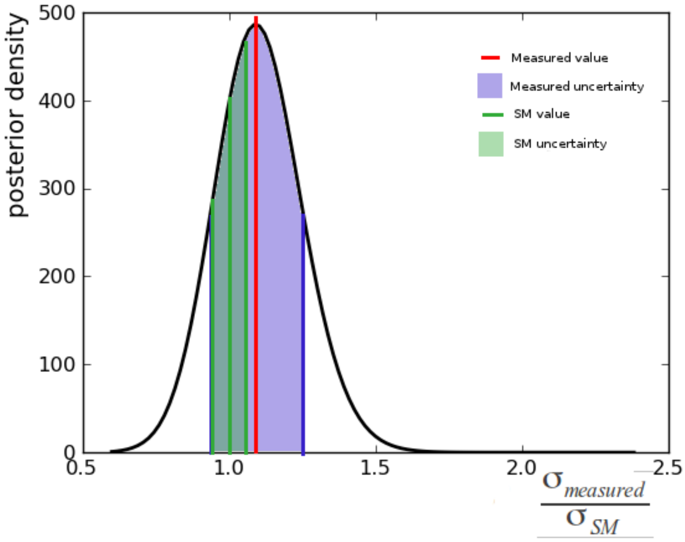

Figure 6.2.: The posterior distribution for the β_1 with the $\pm 1\sigma$ confident intervals (blue). In green the SM prediction with uncertainty is shown.

$$\sigma_{\text{measured}} = \sigma_{\text{theory}} \cdot \beta_1 = 70.64^{+10.60}_{-8.69}\,\text{pb}\,. \tag{6.11}$$

The quoted uncertainty is the overall systematic uncertainty for all evaluated influences in addition with the statistical uncertainty. Within this uncertainties the measured cross section is in good agreement with the SM prediction of $\sigma_{\text{theory}} = 64.6^{+3.5}_{-3.2}\,\text{pb}$ from Eq. (1.5). Moreover, the expected total uncertainty of 13.7% is a good appraised value.

6.3.2. CKM Matrix Element V_{tb}

The determination of the CKM matrix element is done directly from the measured cross section:

$$|V_{tb}|^2 = \frac{\sigma_{\text{measured}}}{\sigma_{\text{theory}}} = 1.09^{+0.17}_{-0.14} \tag{6.12}$$

The value mirrors the 9% deviation of the signal cross sections measurement. The uncertainties of $|V_{tb}|^2$ are estimated due to the theoretical uncertainties of σ_{theory} in Eq. (1.5) and the measured uncertainties of σ_{measured} in Eq. (6.11) with the propagation uncertainty of Gauss, where the correlation between both uncertainties are neglected. Although a value for $|V_{tb}|^2 > 1$ is not compatible with the SM, the systematic uncertainties cover the SM prediction of $|V_{tb}|^2 \approx 1$.

Summary and Outlook

In this thesis the first time the measurement of the cross section of the electroweak production of single top quarks with an electron in the final state at the CMS detector has been presented. This SM process includes a Wtb vertex in the Feynman diagrams and hence a vertex which is directly influenced by the CKM matrix element V_{tb}. Beside three possible production modes, this analysis focusses on the t-channel, in which the top quark decays into an electron via a W boson. The topology of this process contains a neutrino, indicated by missing transverse energy, an isolated electron, a light quark jet, which is presumably found in the forward region, and one or two b jets.

In this analysis, data recorded with the CMS detector with a center-of-mass energy of $\sqrt{s} = 7\,\text{TeV}$, is analysed. The data set corresponds to an integrated luminosity of $\mathcal{L} = (920.7 \pm 41.3)\ \text{pb}^{-1}$ and was collected with a crosstrigger, which was especially developed for single top quark production.

Within this thesis a selection for single top quark events containing an electron was developed and applied for different analysis channels. Allover, six analysis channels which cover different phase spaces with single top quark and background enriched regions. Several background processes with the same final state a the single process complicate the selection of signal processes, where the largest contribution comes from W+jets and $t\bar{t}$ production. In order to estimate these backgrounds the selection is divided into six channels, differing in the number of selected jets and the number of b tagged jets. The channels with no b tagged jet (2j0t and 3j0t) are W+jets enriched, the channels with two or more b jets (2j2t and 3j2t) are $t\bar{t}$ enriched. The largest signal to background ratio is reached in the channels with exactly one b jet (2j1t and 3j1t). After all selection cuts in the 2j1t (3j1t) channel, around 230 (95) single top quark t-channel events are expected to be contained in this amount of data (see Tab. 4.5).

For each single top quark enriched channel (2j1t and 3j1t) a Neural Network (NN) is trained. Therefore, several variables, describing kinematic properties of the final state objects, are used as input for the NN. The NN allocates an output value to each event and accurately separates signal from background events. Both networks perform well also in the background enriched channels.

The extraction of the signal cross section is performed with a sophisticated Bayesian approach to the NN output in all six channels simultaneously. The background enriched regions provide a perfect phase space to estimate the contribution from the background processes. Within this method several systematic uncertainties are taken into account. For each systematic uncertainty a nuisance parameter is introduced and two templates with $\pm 1\sigma$ variation are evaluated. In order to estimate the influence of each systematic uncertainty itself fit parameter is accomplished with toy data as input. The uncertainty of the luminosity and the b tagging uncertainty have the largest influence on the measurement in this analysis (see Sec. 6.2).

The measurement leads to a cross section of the single top quark t-channel production of $\sigma_{\text{measured}} = 70.64^{+10.60}_{-8.69}$ pb. Within the statistical and systematic uncertainties this result is in good agreement with the SM prediction of $\sigma_{\text{theory}} = 64.6^{+3.5}_{-3.2}$ pb [22]. From the ratio of the measured and the theoratical cross section the absolute value of the CKM matrix element V_{tb} can be extracted to $|V_{tb}|^2 = 1.09^{+0.17}_{-0.14}$, again in agreement with the SM prediction of $|V_{tb}| \approx 1$.

This affords a high precission measurement of the cross section of the single top quark t-channel process.

Outlook

This analysis is part of the measurement of the cross section of single top quark production and determination of the CKM matrix element V_{tb} of the single top quark group of the CMS collaboration. In combination with single top quark events including a muon in the final state, the measurement becomes a lot more precise and reliable. In addition a couple of systematic uncertainties, i. e. PDF uncertainty and matching scale uncertainty, will be added in the future. Moreover, the full data set recorded in 2011, which corresponds to an integrated luminosity of $\mathcal{L} \approx 4.9\,\text{fb}^{-1}$, will be analysed to decrease the statistical uncertainty. Altogether, this analysis is part of the determination of the cross section of single top quark t-channel production, which has the prospect to be the most precise at the moment.

In 2012 the LHC will be operated at a center-of-mass energy of $\sqrt{s} = 8\,\text{TeV}$. This increases the cross section of the single top quark t-channel production by $\sim 33\%$ to $\sigma_{8\,\text{TeV}} \approx 85\,\text{pb}$ (calculated with POWHEG and k factor for 7 TeV [65]) and provides a lot more signal events for evaluation. The single top quark t-channel production is already established and more data allows an increasing precision of the cross section measurement as well as the study of the top quark properties. The estimation for the produced integrated luminosity for 2012 is $\mathcal{L} \sim 15\,\text{fb}^{-1}$. Next to the total cross section measurement one can determine differential cross sections (i. e. in dependence of p_{T}, η_{top} or R_t) with more data.

Furthermore, next analyses will focus on the precise determination of the CKM matrix element V_{tb} by giving up the assumption $V_{ts} << 1$ and $V_{td} << 1$. Simulated samples with non vanishing CKM matrix elements V_{ts} and V_{td} are produced and will be evaluated. The influence of these matrix elements help to measure V_{tb} with a higher precision. Its value and its uncertainty has a large influence on Beyond Standard Model theories, in which a fourth generation of matter is assumed and could be excluded or indirectly detected by a precise measurement of the CKM matrix element. Moreover, new physics like anomalous W boson couplings can be studied.

A. Input Variables 2-Jet Network

This appendix contains the diagrams from all input variables for the 2 jet channel. For this channel the signal enriched and both background enriched regions are shown. Additionally, a shape comparison for the signal and the most important background MC samples is presented (a). This diagrams can demonstrate the separation power for each variable. All data MC comparison diagrams for the signal region (b) are normalized to the prediction ($\mathcal{L} = 920.7\,\mathrm{pb}$). For this channel $\sim 12\%$ more data than expected has been collected. All control region plots (c) and (d) are normalized to data in order to compare the shape of the variables. The color code for all diagrams is shown in Fig. A.1.

Figure A.1.: All diagrams are made with this color code.

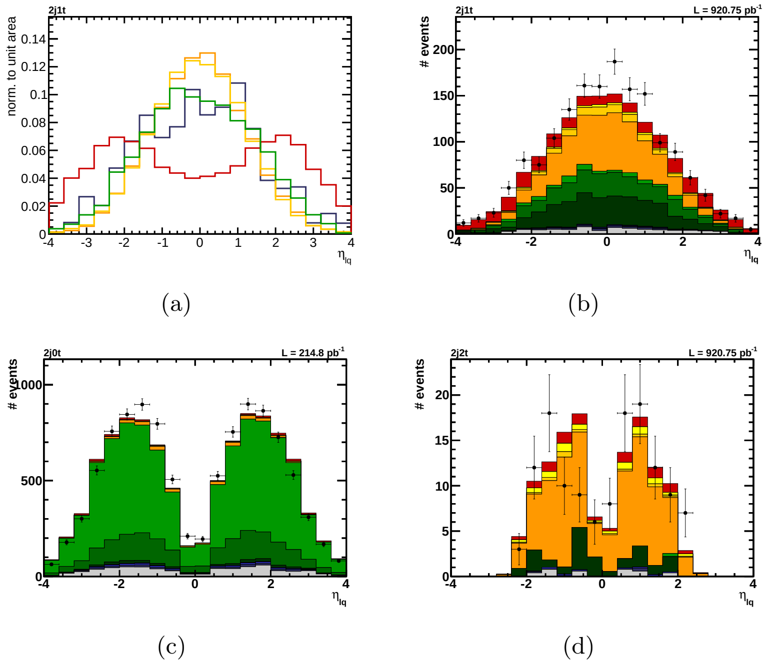

Figure A.2.: η for the recoiling light quark jet. It is the most important variable for both neural networks. The signal show a distribution with two maxima while all background processes have a maximum around zero.

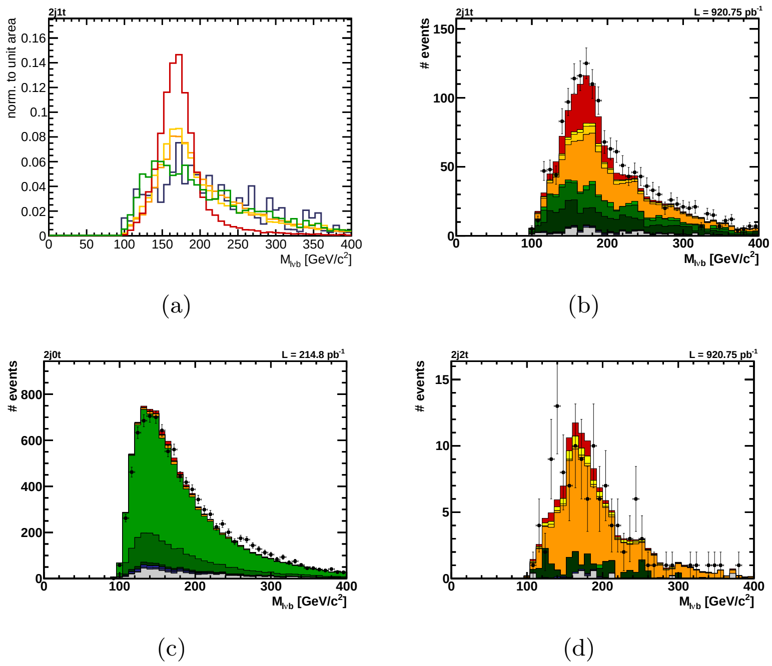

Figure A.3.: The reconstructed top quark mass. Signal events show a clear peak around 173 GeV/c^2. Background events have a broader tail.

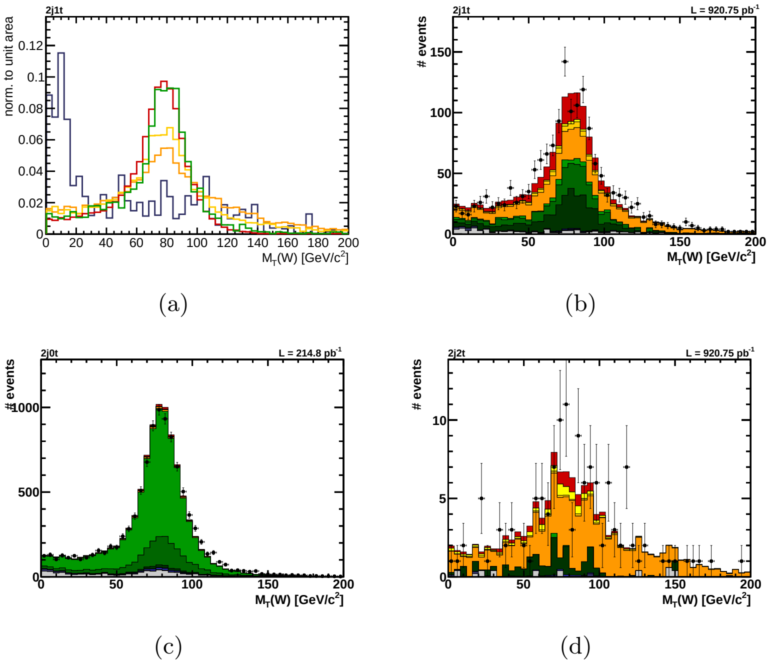

Figure A.4.: The transverse W boson mass. For processes with a W boson the distribution shows a Jacobian peak around 80 GeV/c^2.

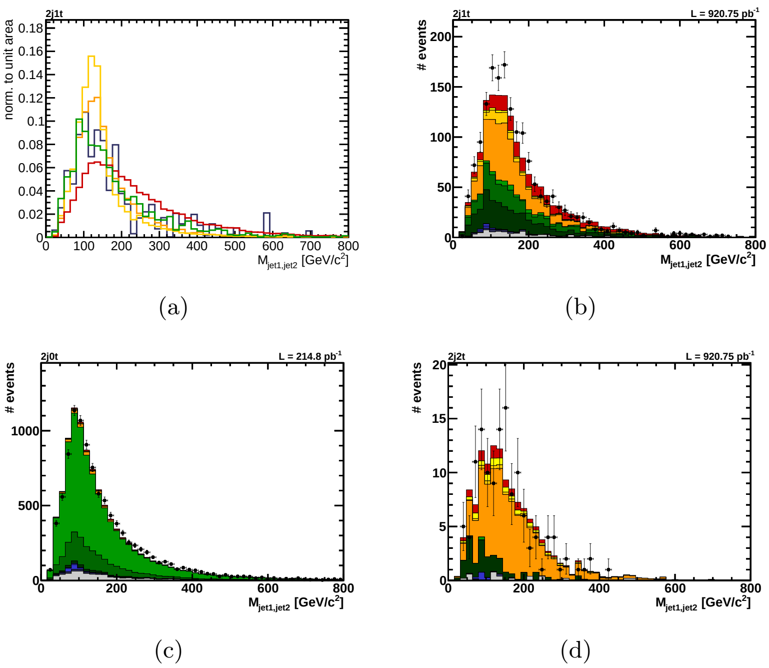

Figure A.5.: The invariant mass of the two hardest jets.

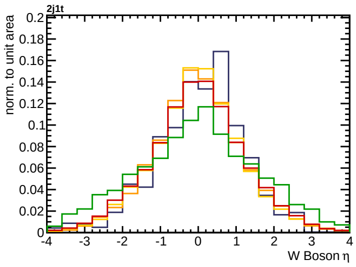

(a)

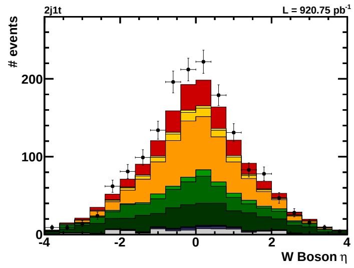

(b)

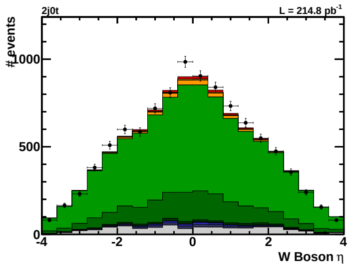

(c)

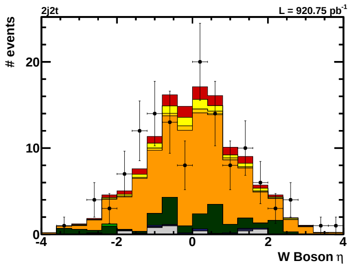

(d)

Figure A.6.: The η distribution of the W boson.

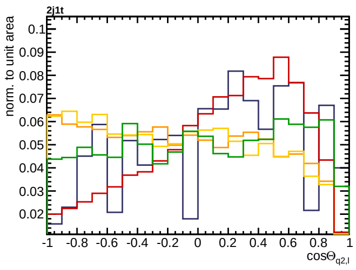

(a)

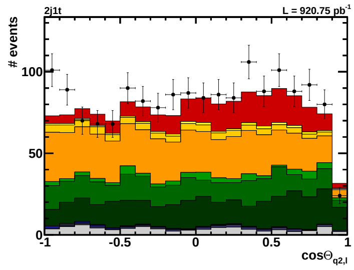

(b)

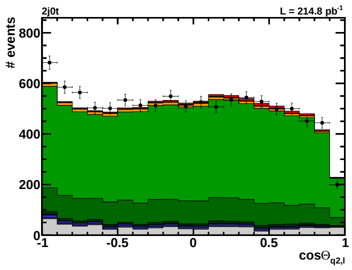

(c)

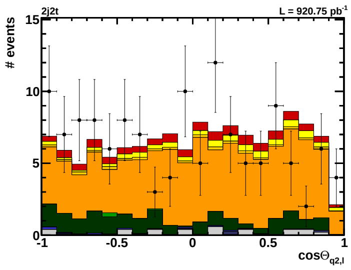

(d)

Figure A.7.: The cosine of the angle between light quark jet and the electron in the top quark rest frame (see Sec. 1.2).

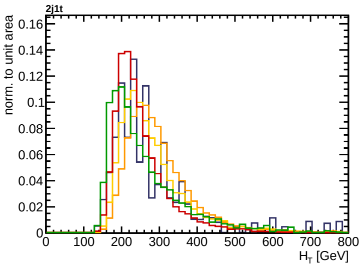

(a)

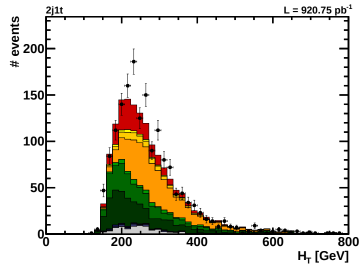

(b)

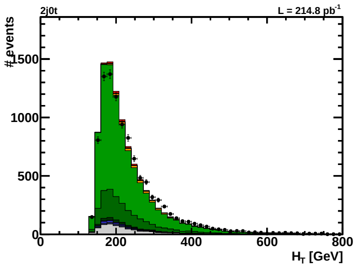

(c)

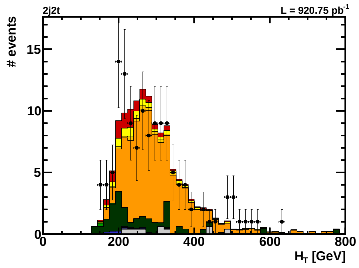

(d)

Figure A.8.: The sum of all transverse energies.

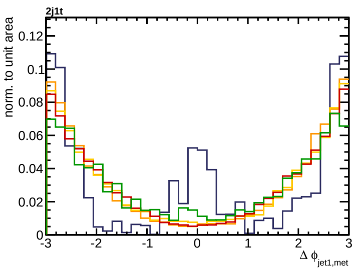

(a)

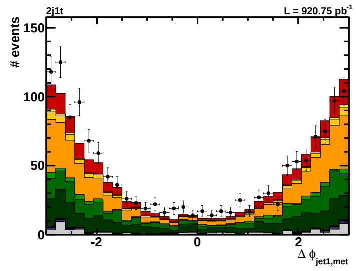

(b)

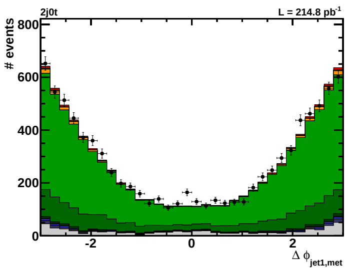

(c)

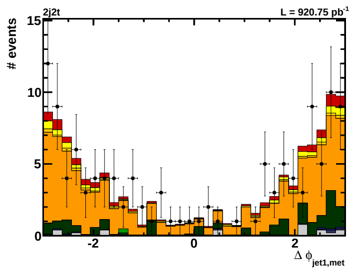

(d)

Figure A.9.: The difference between the ϕ values of the hardest jet and the missing transverse energy $\Delta\phi_{\mathrm{jet1,MET}} = \phi_{\mathrm{jet1}} - \phi_{\mathrm{MET}}$.

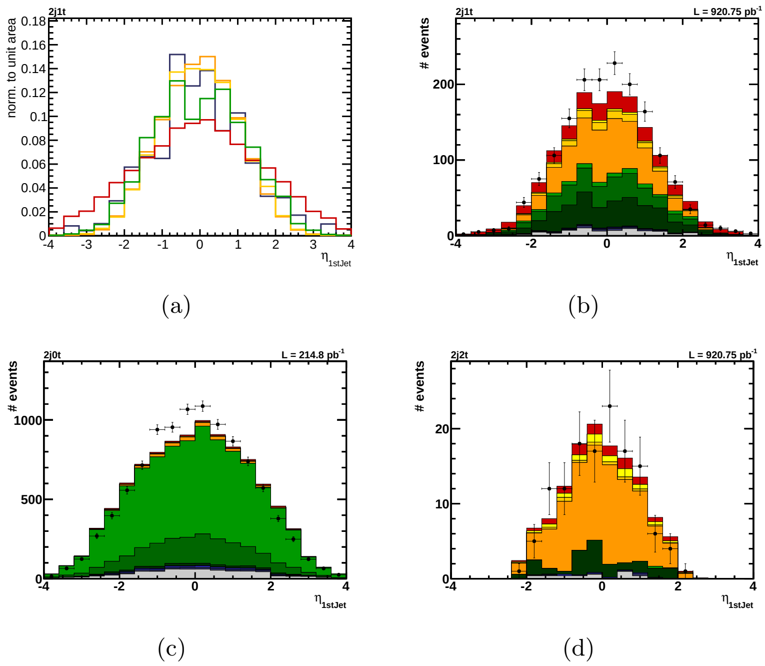

Figure A.10.: The η distribution for the hardest jet.

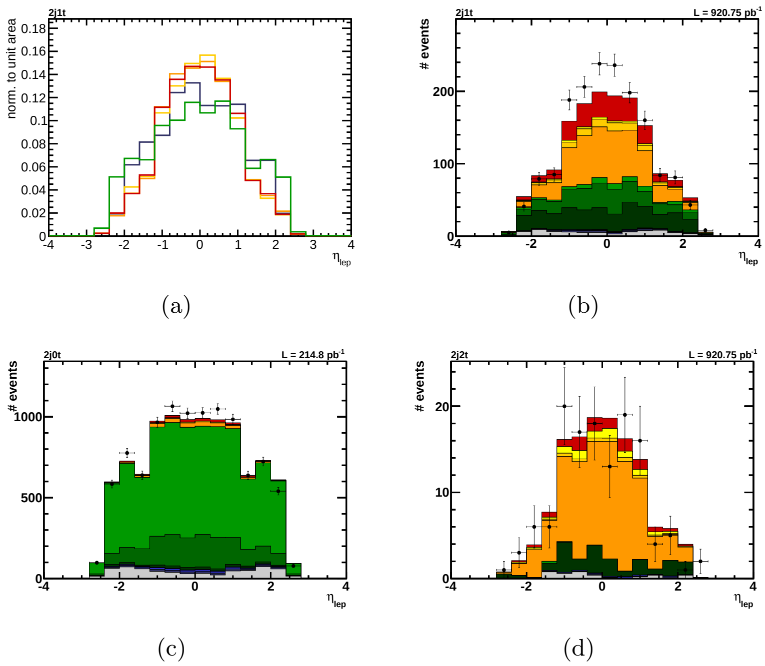

Figure A.11.: The η distribution for the selected electron.

B. Input Variables 3-Jet Network

This appendix contains the diagrams from all input variables for the 3 jet channel. For this network the signal and both control regions are shown. Additionally, a shape comparison for the signal and the most important background MC samples is presented (a). This diagrams can demonstrate the separation power for each variable. All data MC comparison diagrams for the signal region (b) are normalized to the prediction ($\mathcal{L} = 920.7\,\mathrm{pb}$). For this channel $\sim 21\%$ more data than expected has been collected. All control region plots (c) and (d) are normalized to data in order to compare the shape of the variables. The color code for all diagrams is shown in figreflegendapp2.

Figure B.1.: All diagrams are made with this color code.

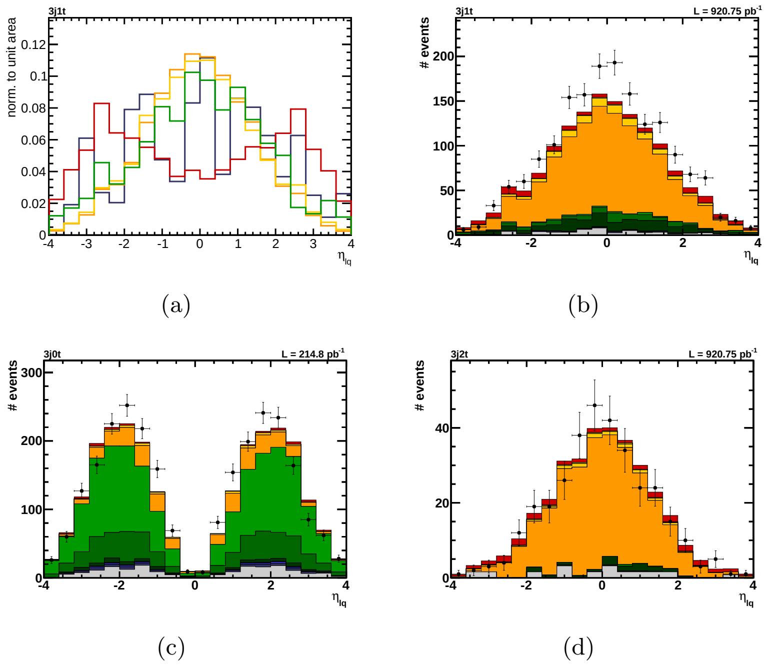

Figure B.2.: η for the recoiling light quark jet. It is the most important variable for both neural networks.

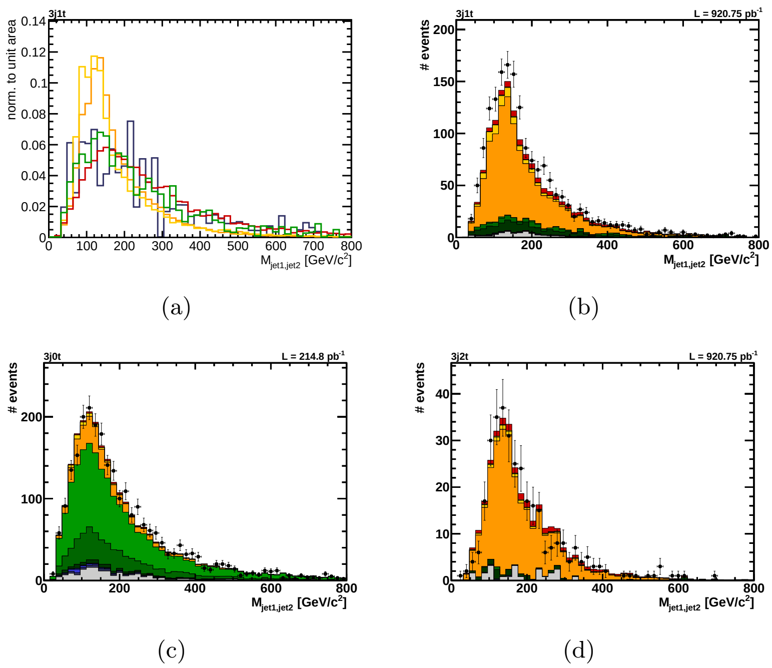

Figure B.3.: The invariant mass of the two hardest jets.

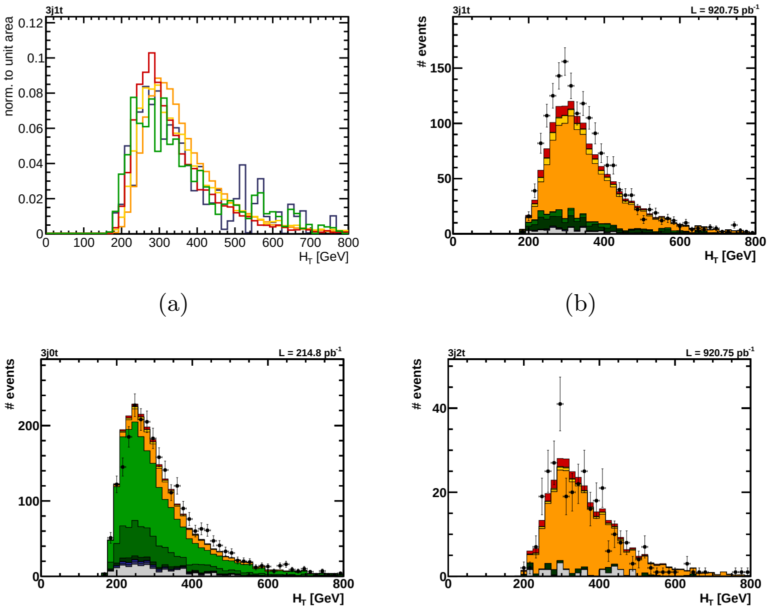

(a) (b)

(c) (d)

Figure B.4.: The sum of all transverse energies.

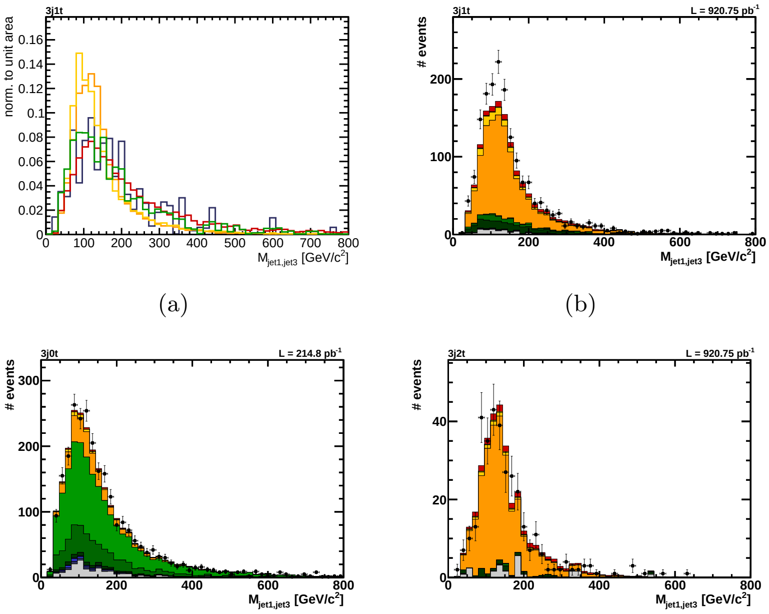

(a) (b)

(c) (d)

Figure B.5.: The invariant mass of the hardest and the third hardest jets.

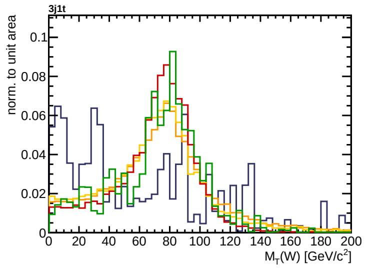

(a)

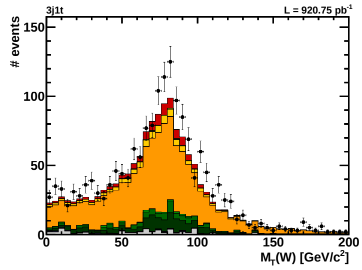

(b)

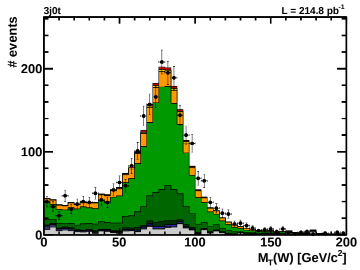

(c)

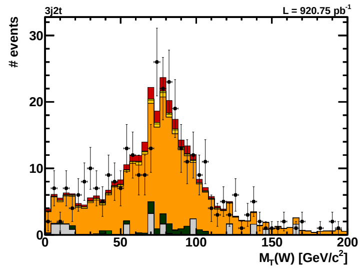

(d)

Figure B.6.: The transverse W boson mass. The distribution of processes with a W boson mass shows a Jacobian peak around 80 GeV/c^2.

j

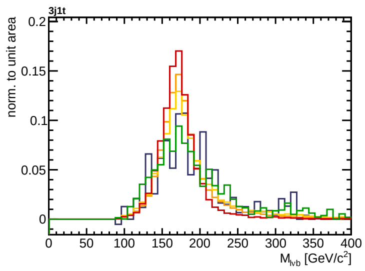

(a)

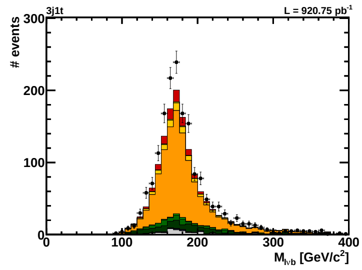

(b)

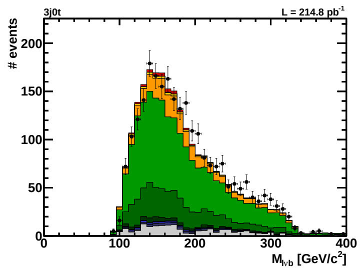

(c)

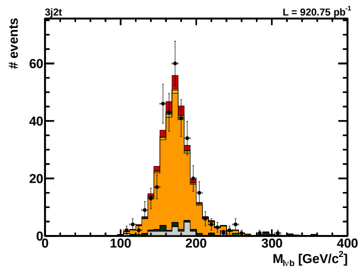

(d)

Figure B.7.: The reconstructed top quark mass.

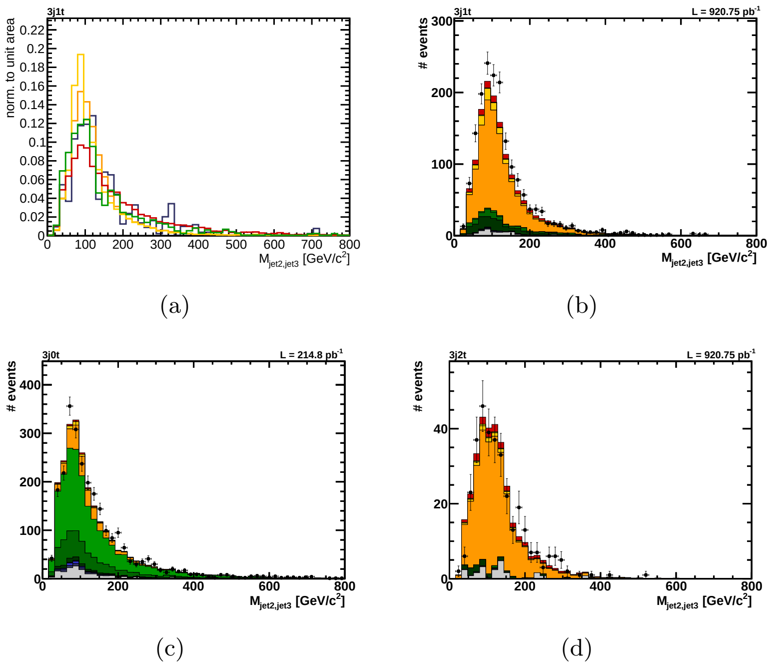

Figure B.8.: The invariant mass of the second hardest and the third hardest jets.

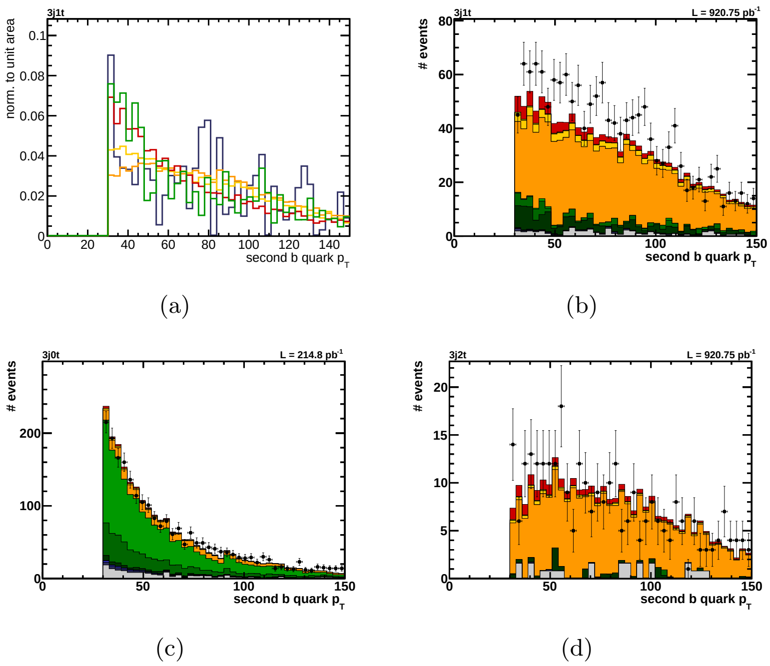

Figure B.9.: The transverse momentum of the second b quark

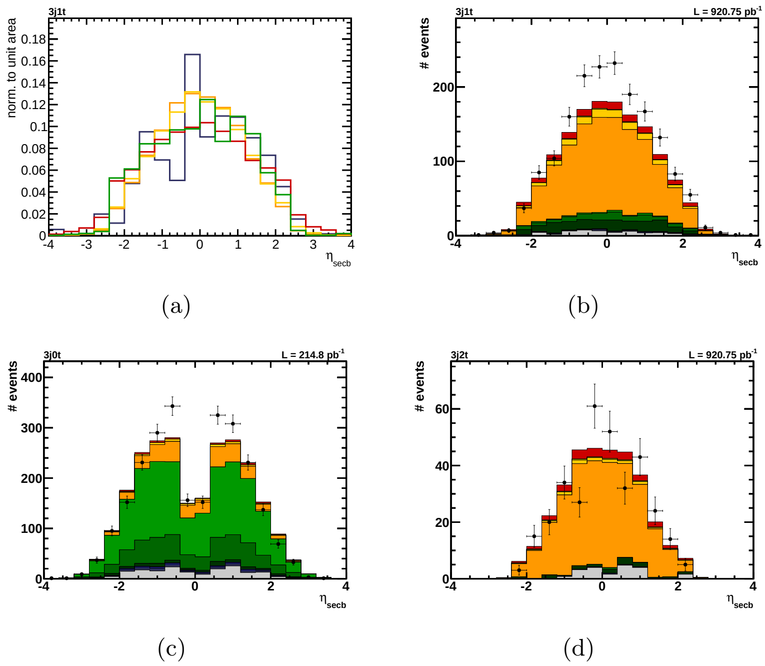

Figure B.10.: The η distribution for the second b quark

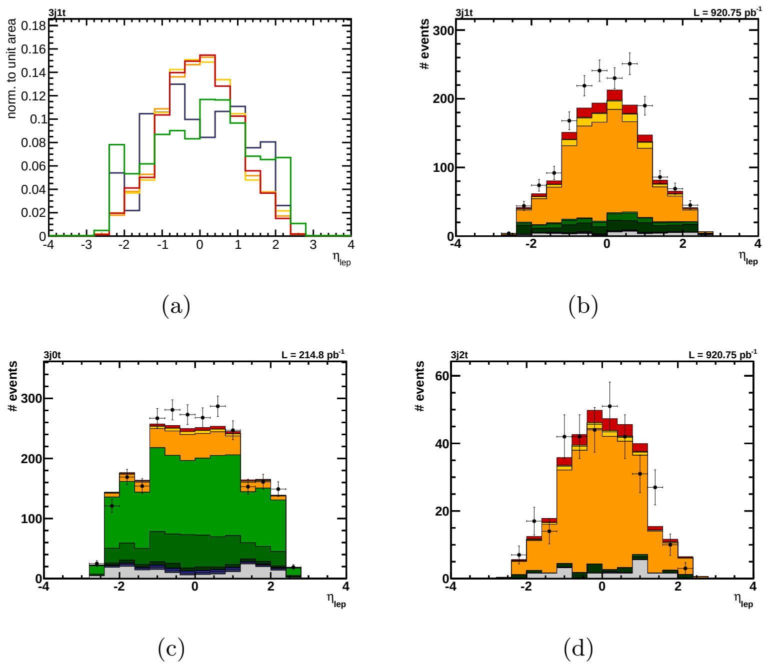

Figure B.11.: The η distribution for the selected electron.

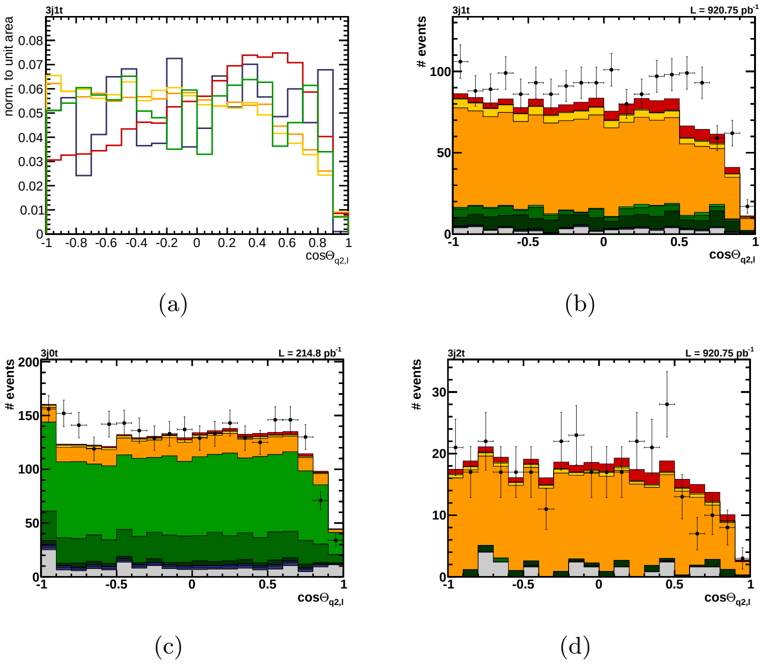

(a) (b)

(c) (d)

Figure B.12.: The cosine of the angle between light quark jet and the electron in the top quark rest frame.

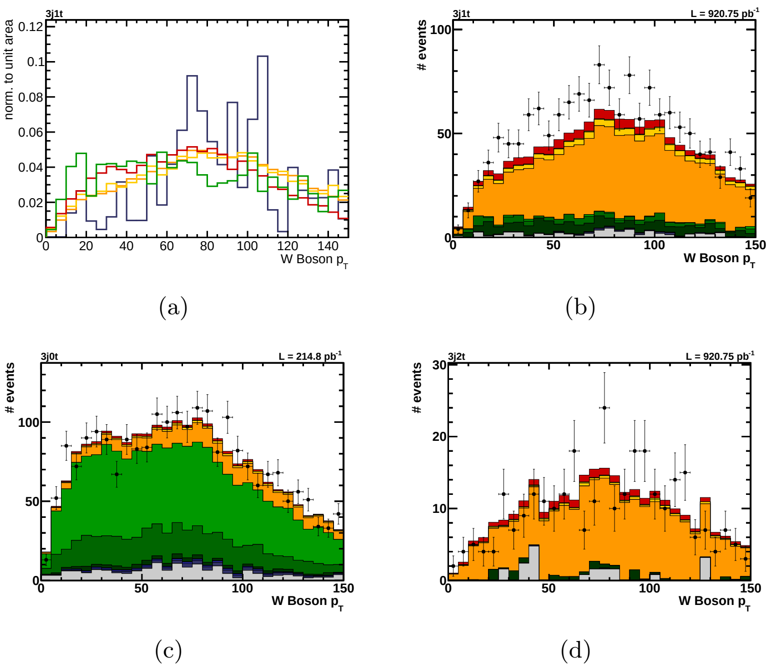

(a) (b)

(c) (d)

Figure B.13.: The transverse momentum distribution of the W boson.

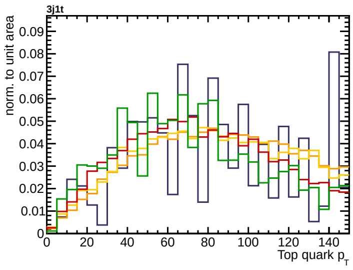

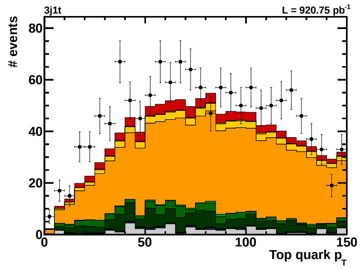

(a) (b)

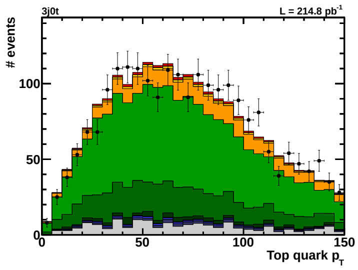

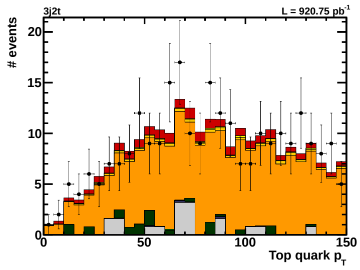

(c) (d)

Figure B.14.: The transverse momentum distribution of the top quark.

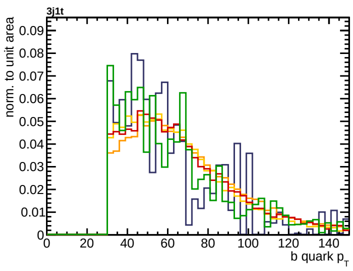

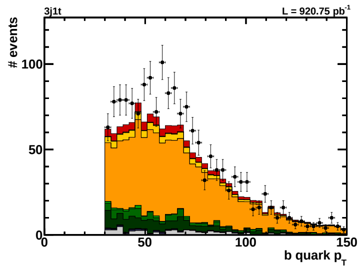

(a) (b)

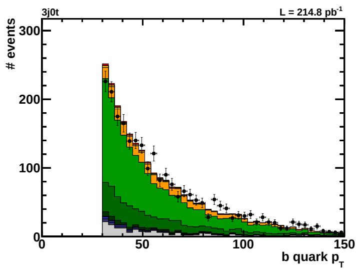

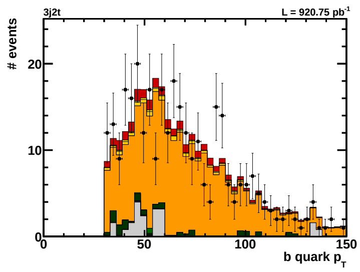

(c) (d)

Figure B.15.: The transverse momentum distribution of the b quark stemming from the top quark decay.

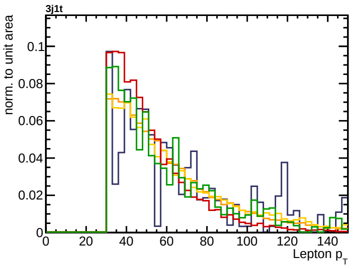

(a)

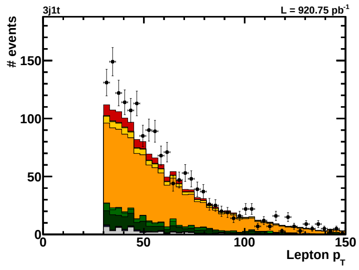

(b)

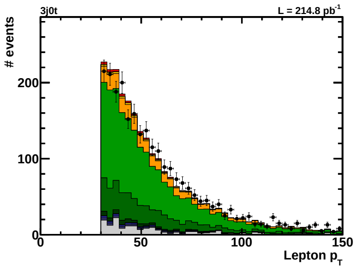

(c)

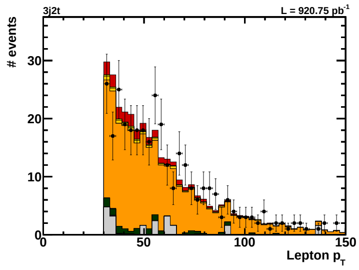

(d)

Figure B.16.: The transverse momentum distribution of the selected electron.

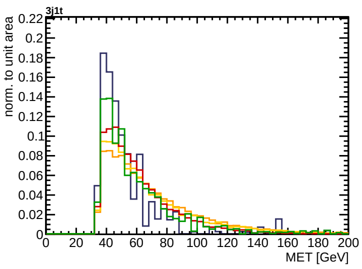

(a)

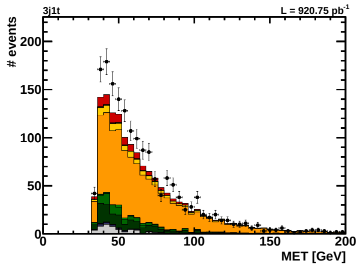

(b)

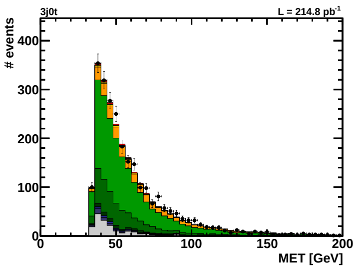

(c)

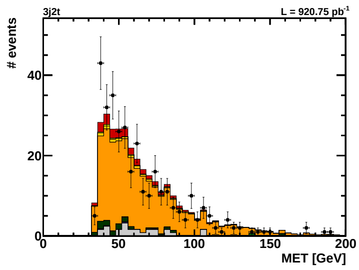

(d)

Figure B.17.: The missing transverse energy distribution.

List of Figures

0.1. Ausgabe des Neuronalen Netzwerkes iii
0.2. Posterior-Verteilung iv

1.1. LO Feynman diagrams for different interactions 10
1.2. An example of a Parton Distribution Function 11
1.3. LO Feynman diagrams for top quark pair production 13
1.4. LO Feynman diagrams for single top quark production 13
1.5. NLO Feynman diagrams for single top t-channel 14
1.6. NLO Feynman diagrams for single top tW-channel 15
1.7. NLO Feynman diagrams for single top s-channel 16
1.8. Spin polarization of Single Top Quarks 17

2.1. LHC overview 20
2.2. LHC preaccelerator 21
2.3. CMS detector layout 23
2.4. CMS tracking system 24
2.5. CMS longitudinal view 26
2.6. CMS muon system 28
2.7. CMS trigger 29
2.8. CMS grid 30

3.1. Monte Carlo event generation processes 32
3.2. Jet evolution 38
3.3. Comparison of jet resolutions for calorimeter, JPT, and PFJets. . . . 41
3.4. b Tagging 42
3.5. Working points of the TCHP b tagging algorithm 43
3.6. MET with different input objects 45

4.1. Cross section for several processes 48
4.2. LO Feynman diagram for $t\bar{t}$ production 49
4.3. LO Feynman diagrams for single top quark production 50
4.4. Feynman diagrams for vector boson production 50
4.5. Feynman diagrams for diboson production 51
4.6. Feynman diagrams for QCD multijet production 51
4.7. MET distribution 58
4.8. MET distribution for different electron definitions 59
4.9. QCD template fits 60
4.10. Trigger turn-on curves of the CentralJet30 trigger. 63

5.1. Three layer Neural Network 68
5.2. Sigmoid function 69
5.3. Two most important input variables in the 2j1t channel 71
5.4. Two most important input variables in the 3j1t channel 71
5.5. Correlations of input variables in the 2j1t channel 75
5.6. Correlations of input variables in the 3j1t channel 77
5.7. Output of the NN trainings 78
5.8. Output of the trained NN for the 2j1t channel 80
5.9. Output of the trained NN for the 3j1t channel 81

6.1. Shape change of the NN output from JES/JER 85
6.2. Posterior density for σ_t 92

A.1. Legend for diagrams 99
A.2. Light quark η distribution (2j1t) 100
A.3. Reconstructed top quark mass distribution (2j1t) 100
A.4. Transverse W boson mass distribution (2j1t) 101
A.5. Dijet mass distribution (2j1t) 101
A.6. η of W boson distribution (2j1t) 102
A.7. $\cos\Theta$ distribution (2j1t) 102
A.8. H_{T} distribution (2j1t) 103
A.9. $\phi_{\mathrm{jet1}} - \phi_{\mathrm{MET}}$ distribution (2j1t) 103
A.10. η of the hardest jet distribution (2j1t) 104
A.11. η of selected electron distribution (2j1t) 104

B.1. Legend for Diagrams 105
B.2. Light quark η distribution (3j1t) 106
B.3. Dijet mass distribution (3j1t) 106
B.4. H_{T} distribution (3j1t) 107
B.5. Dijet mass distribution (3j1t) 107
B.6. Transverse W boson mass distribution (3j1t) 108
B.7. Reconstructed top quark mass distribution (3j1t) 108
B.8. Dijet mass distribution (3j1t) 109
B.9. p_{T} of the second b quark distribution (3j1t) 109
B.10. η of the second b quark distribution (3j1t) 110
B.11. η of selected electron distribution (3j1t) 110
B.12. $\cos\Theta$ distribution (3j1t) 111
B.13. p_{T} of W boson distribution (3j1t) 111
B.14. p_{T} of the top quark distribution (3j1t) 112
B.15. p_{T} of the b quark stemming from the top quark distribution (3j1t) . 112
B.16. p_{T} of the electron distribution (3j1t) 113
B.17. MET distribution (3j1t) 113

List of Tables

1.1. Fermions in the Standard Model 8
1.2. Bosons in the Standard Model 8

3.1. Working points of the TCHP b tagging algorithm 44

4.1. Details on MC samples 53
4.2. Overview of triggers and data sets 55
4.3. Fit results for β_{QCD} 61
4.4. Jet energy correction scale factors 62
4.5. Event yield 64
4.6. Jet assignment for all channels 66

5.1. Input variables and their significance in the 2j1t channel 74
5.2. Input variables and their significance in the 3j1t channel 76

6.1. Jet energy correction scale cactors with systematic uncertainties . . 87
6.2. b tagging scale factors with uncertainties 87
6.3. Variation of Gompertz function parameters for CentralJet30 88
6.4. Variation of Gompertz function parameters for BTagIP 89
6.5. Rate uncertainties for background processes 89
6.6. Summary of individual uncertainties 91

Bibliography

[1] E. Rutherford, "The Scattering of α and β Particles by Matter and the Structure of the Atom", Phil. Mag. 21, 669–688 (1911).

[2] F. Abe et al., "Observation of Top Quark Production in $p\bar{p}$ Collisions with the Collider Detector at Fermilab", Phys. Rev. Lett. 74, 2626–2631 (1995).

[3] S. Abachi et al., "Observation of the Top Quark", Phys. Rev. Lett. 74, 2632–2637 (1995).

[4] Tevatron Electroweak Working Group, "Combination of CDF and D0 results on the mass of the top quark using up to 5.8 fb-1 of data", FERMILAB-TM-2504-E, CDF-NOTE-10549, D0-NOTE-6222, (2011).

[5] V. M. Abazov et al., "Observation of Single Top Quark Production", Phys. Rev. Lett. 103, 092001 (2009).

[6] T. Aaltonen et al., "Observation of Electroweak Single Top Quark Production", Phys. Rev. Lett. 103, 092002 (2009).

[7] Th. Müller, J. Ott, and J. Wagner-Kuhr, "Theta - A Framework for Template Based Modelling and Inference", CMS Internal Note CMS-IN 2010/017 (2010).

[8] S. Chatrchyan et al., "Measurement of the $t\bar{t}$ production cross section and the top quark mass in the dilepton channel in pp collisions at $\sqrt(s) = 7\,\mathrm{TeV}$", JHEP 1107, 049 (2011).

[9] A. Einstein, "Grundlage der Allgemeinen Relativitätstheorie", Annalen Phys. 49, 769–822 (1916).

[10] E. Noether, "Invarianten beliebiger Differentialausdrücke", Nachr. Königl. Ges. Wiss. Göttingen 235–257 (1918).

[11] S. Khalil and E. Torrente-Lujan, "Neutrino Mass and Oscillation as Probes of Physics beyond the Standard Model", J. Egyptian Math. Soc. 9, 91–141 (2001).

[12] K. Nakamura et al., "Review of particle physics", J. Phys. G37, 075021 (2010).

[13] S. Chatrchyan et al., "Combined results of searches for the standard model Higgs boson in pp collisions at sqrt(s) = 7 TeV".

[14] N. Cabibbo, "Unitary Symmetry and Leptonic Decays", Phys. Rev. Lett. 10, 531–533 (1963).

[15] M. Kobayashi and T. Maskawa, "CP Violation in the Renormalizable Theory of Weak Interaction", Prog. Theor. Phys. 49, 652–657 (1973).

[16] D. Stump et al., "Inclusive jet production, parton distributions, and the search for new physics", JHEP 10, 046 (2003).

[17] CMS Collaboration, "Measurement of the Top Quark Mass in the Muon + Jets Channel", CMS Physics Analysis Summary TOP-11-015 (2012).

[18] ATLAS Collaboration, "Measurement of the Top-Quark Mass from 2011 ATLAS Data using the Template Method", ATLAS-CONF-2011-120 (2011).

[19] J. H. Kuhn, A. Scharf, and P. Uwer, "Electroweak effects in top-quark pair production at hadron colliders", Eur.Phys.J. C51, 37–53 (2007).

[20] N. Kidonakis, "Top quark pair and single top production at Tevatron and LHC energies", `arXiv:hep-ph/1008.2460` (2010).

[21] A. D. Martin, W. J. Stirling, R. S. Thorne, and G. Watt, "Parton distributions for the LHC", Eur. Phys. J. C63, 189–285 (2009).

[22] N. Kidonakis, "Next-to-next-to-leading-order collinear and soft gluon corrections for t-channel single top quark production", Phys. Rev. D 83, 091503 (May, 2011).

[23] C. D. White, S. Frixione, E. Laenen, and F. Maltoni, "Isolating Wt production at the LHC", JHEP 0911, 074 (2009).

[24] N. Kidonakis, "Two-loop soft anomalous dimensions for single top quark associated production with a W^- or H^-", Phys.Rev. D82, 054018 (2010).

[25] G. Mahlon and S. J. Parke, "Single top quark production at the LHC: Understanding spin", Phys. Lett. B476, 323–330 (2000).

[26] P. Motylinski, "Angular correlations in t-channel single top production at the LHC", Phys. Rev. D80, 074015 (2009).

[27] S. Röcker, "Prospects for the oberservation of single top quark production with the CMS experiment using neural networks.", Diploma Thesis, Karlsruhe Institute of Technology, IEKP-KA/2011-6 (2011).

[28] K. Desler and D. A. Edwards, "Accelerator Physics of Colliders", Phys. Rev. D66, 010001 (2002).

[29] S. van der Meer, "Calibration of the effective beam height in the ISR." Technical Report CERN-ISR-PO-68-31. ISR-PO-68-31, CERN, Geneva, 1968.

[30] C. Collaboration, "Absolute Luminosity Normalization", CMS DP 2011-002.

[31] L. Evans, (ed.) and P. Bryant, (ed.), "LHC Machine", JINST 3, S08001 (2008).

[32] K. Aamodt et al., "The ALICE Experiment at the LHC", JINST 3, S08002 (2008).

[33] A. A. Alves et al., "The LHCb Detector at the LHC", JINST 3, S08005 (2008).

[34] G. Aad et al., "The ATLAS Experiment at the LHC", JINST 3, S08003 (2008).

[35] R. Adolphi et al., "The CMS experiment at the CERN LHC", JINST 3, S08004 (2008).

[36] J. Gruschke, "Observation of Top Quarks and First Measurement of the $t\bar{t}$ Production Cross Section at a Centre-Of-Mass Energy of 7 TeV with the CMS Experiment at the LHC", PhD Thesis, Karlsruhe Institute of Technology, IEKP-KA/2011-04 (2011).

[37] M. Benedikt et al., "The LHC Design Report v.3: The LHC Injector Chain", CERN, Geneva, CERN-2004-003-V-3 (2004).

[38] CMS Outreach Group, "CMS Outreach Web Page." `http://cms.web.cern.ch`, (August, 2010).

[39] CMS Collaboration, "The CMS Tracker System Project: Technical Design Report", CMS TDR, CERN, Geneva, CERN-LHCC-98-06 (1997).

[40] CMS Collaboration, "The CMS Tracker: Addendum to the Technical Design Report", CMS TDR, CERN, Geneva, CERN-LHCC-2000-016 (2000).

[41] P. Adzic et al., "Energy Resolution of the Barrel of the CMS Electromagnetic Calorimeter", JINST 2, P04004 (2007).

[42] CMS Collaboration, "The CMS Muon Project: Technical Design Report", CMS TDR, CERN, Geneva, CERN-LHCC-97-32 (1997).

[43] CMS Collaboration, "Physics Technical Design Report, Volume I: Detector Performance and Software", CMS TDR, CERN, Geneva CERN-LHCC-2006-001 (2006).

[44] WLCG Collaboration, "LHC Computing Grid: Technical Design Report", LCG TDR, CERN, Geneva, CERN-LHCC-2002-024 (2005).

[45] J. Bauer, "Prospects for the Observation of Electroweak Top Quark Production with the CMS Experiment", PhD Thesis, Karlsruhe Institute of Technology, IEKP-KA/2010-8 (2010).

[46] M. Dobbs and J. B. Hansen, "The HepMC C++ Monte Carlo Event Record for High Energy Physics", Comput. Phys. Commun. 134, 41–46 (2001).

[47] V. N. Gribov and L. N. Lipatov, "Deep Inelastic *ep* Scattering in Perturbation Theory", Sov. J. Nucl. Phys. 15, 438–450 (1972).

[48] G. Altarelli and G. Parisi, "Asymptotic Freedom in Parton Language", Nucl. Phys. B126, 298 (1977).

[49] Y. L. Dokshitzer, "Calculation of the Structure Functions for Deep Inelastic Scattering and e^+e^- Annihilation by Perturbation Theory in Quantum Chromodynamics", Sov. Phys. JETP 46, 641–653 (1977).

[50] B. Andersson, G. Gustafson, G. Ingelman, and T. Sjöstrand, "Parton Fragmentation and String Dynamics", Phys. Rept. 97, 31–145 (1983).

[51] S. Riedel, "Integration of Cloud Resources into Workflows of Particle Physics Analyses and Measurement of the Underlying Event in Proton-Proton-Collisions at the LHC", Diploma Thesis, Karlsruhe Institute of Technology, IEKP-KA/2011-29 (2011).

[52] S. Catani, F. Krauss, R. Kühn, and B. R. Webber, "QCD Matrix Elements + Parton Showers", JHEP 11, 063 (2001).

[53] F. Krauss, "Matrix Elements and Parton Showers in Hadronic Interactions", JHEP 08, 015 (2002).

[54] M. L. Mangano, M. Moretti, F. Piccinini, and M. Treccani, "Matching Matrix Elements and Shower Evolution for Top-Quark Production in Hadronic Collisions", JHEP 01, 013 (2007).

[55] T. Sjöstrand et al., "High Energy Physics Event Generation with Pythia 6.1", Comput. Phys. Commun. 135, 238–259 (2001).

[56] G. Corcella et al., "Herwig 6: An Event Generator for Hadron Emission Reactions with Interfering Gluons (Including Supersymmetric Processes)", JHEP 01, 010 (2001).

[57] T. Stelzer and W. F. Long, "Automatic generation of tree level helicity amplitudes", Comput. Phys. Commun. 81, 357–371 (1994).

[58] F. Maltoni and T. Stelzer, "MadEvent: Automatic Event Generation with MadGraph", JHEP 02, 027 (2003).

[59] J. Alwall et al., "MadGraph/MadEvent v4: The New Web Generation", JHEP 09, 028 (2007).

[60] M. L. Mangano et al., "ALPGEN, a Generator for Hard Multiparton Processes in Hadronic Collisions", JHEP 07, 001 (2003).

[61] S. Agostinelli et al., "GEANT4: A Simulation Toolkit", Nucl. Instrum. Meth. A506, 250–303 (2003).

[62] J. Alwall et al., "A standard format for Les Houches event files", Comput. Phys. Commun. 176, 300–304 (2007).

[63] P. Nason, "A new method for combining NLO QCD with shower Monte Carlo algorithms", JHEP 11, 040 (2004).

[64] S. Frixione, P. Nason, and C. Oleari, "Matching NLO QCD computations with Parton Shower simulations: the POWHEG method", JHEP 11, 070 (2007).

[65] S. Alioli, P. Nason, C. Oleari, and E. Re, "A general framework for implementing NLO calculations in shower Monte Carlo programs: the POWHEG BOX", JHEP 06, 043 (2010).

[66] CMS Collaboration, "Fast Simulation of the CMS Detector at the LHC", CERN-CMS-CR-2010-297 (2010).

[67] S. Alioli, P. Nason, C. Oleari, and E. Re, "NLO single-top production matched with shower in POWHEG: s- and t-channel contributions", JHEP 09, 111 (2009).

[68] T. Speer et al., "Track Reconstruction in the CMS Tracker", Nucl. Instrum. Meth. A559, 143–147 (2006).

[69] R. Frühwirth, "Application of Kalman Filtering to Track and Vertex Fitting", Nucl. Instrum. Meth. A262, 444–450 (1987).

[70] CMS Collaboration, "Particle-Flow Event Reconstruction in CMS and Performance for Jets, $\not{E}_{\mathrm{T}}$, and Taus", CMS Physics Analysis Summary PFT-09-001 (2009).

[71] CMS Collaboration, "Commissioning of the particle-flow event reconstruction with leptons from J/Psi and W decays at 7 TeV", CMS Physics Analysis Summary PFT-10-003 (2010).

[72] CMS Collaboration, "Performance of muon identification in pp collisions at $\sqrt{s} = 7$ TeV", CMS Physics Analysis Summary MUO-10-002 (2010).

[73] G. P. Salam and G. Soyez, "A Practical Seedless Infrared-Safe Cone Jet Algorithm", JHEP 05, 086 (2007).

[74] S. Catani, Y. L. Dokshitzer, M. H. Seymour, and B. R. Webber, "Longitudinally Invariant k_{T} Clustering Algorithms for Hadron Hadron Collisions", Nucl. Phys. B406, 187–224 (1993).

[75] Y. L. Dokshitzer, G. D. Leder, S. Moretti, and B. R. Webber, "Better Jet Clustering Algorithms", JHEP 08, 001 (1997).

[76] M. Wobisch and T. Wengler, "Hadronization Corrections to Jet Cross Sections in Deep-Inelastic Scattering", arXiv:hep-ph/9907280 (1998).

[77] M. Cacciari, G. P. Salam, and G. Soyez, "The Anti-k_T Jet Clustering Algorithm", JHEP 04, 063 (2008).

[78] CMS Collaboration, "Jet Plus Tracks Algorithm for Calorimeter Jet Energy Corrections in CMS", CMS Physics Analysis Summary JME-09-002 (2009).

[79] CMS Collaboration, "Jet Performance in pp Collisions at $\sqrt{s} = 7$ TeV", CMS Physics Analysis Summary JME-10-003 (2010).

[80] CMS Collaboration, "Plans for Jet Energy Corrections at CMS", CMS Physics Analysis Summary JME-07-002 (2007).

[81] CMS Collaboration, "Determination of jet energy calibration and transverse momentum resolution in CMS", Journal of Instrumentation 6, 11002 (2011).

[82] DØ Collaboration, "B Jet Identification." http://www-d0.fnal.gov/Run2Physics/top/singletop_observation/b_tagging_graphic.png (November 2011).

[83] CMS Collaboration, "Algorithms for b-jet identification in CMS", CMS Physics Analysis Summary BTV-09-001 (2009).

[84] CMS Collaboration, "Commissioning of b-Jet Identification with pp Collisions at $\sqrt{s} = 7$ TeV", CMS Physics Analysis Summary BTV-10-001 (2010).

[85] CMS Collaboration, "$\vec{\not{E}}_\mathrm{T}$ Performance in CMS", CMS Physics Analysis Summary JME-07-001 (2007).

[86] CMS Collaboration, "Track-Corrected Missing Transverse Energy in CMS", CMS Physics Analysis Summary JME-09-010 (2009).

[87] CMS Collaboration, "Missing Transverse Energy Performance in Minimum-Bias and Jet Events from Proton-Proton Collisions at $\sqrt{s} = 7$ TeV", CMS Physics Analysis Summary JME-10-004 (2010).

[88] J. M. Campbell, J. W. Huston, and W. J. Stirling, "Hard Interactions of Quarks and Gluons: A Primer for LHC Physics", Reports on Progress in Physics 70, 89 (2007).

[89] S. Mandelstam, "Determination of the Pion-Nucleon Scattering Amplitude from Dispersion Relations and Unitarity. General Theory", Phys. Rev. 112, 1344–1360 (1958).

[90] N. Kidonakis, "NNLL resummation for s-channel single top quark production", Phys.Rev. D81, 054028 (2010).

[91] K. Melnikov and F. Petriello, "Electroweak gauge boson production at hadron colliders through $\mathcal{O}(\alpha_s^2)$", Phys.Rev. D74, 114017 (2006).

[92] J. M. Campbell and Ellis, "MCFM - Monte Carlo for FeMtobarn processes.".

[93] L. Tuura, A. Meyer, I. Segoni, and G. Della Ricca, "CMS Data Quality Monitoring: Systems and Experiences", J. Phys. Conf. Ser. 219, 072020 (2010).

[94] CMS Collaboration, "Data Quality Monitoring (DQM): JSON File." https://cms-service-dqm.web.cern.ch/cms-service-dqm/CAF/certification/Collisions11/7TeV/Prompt/Cert_160404-167913_7TeV_PromptReco_Collisions11_JSON.txt (internal), (November 2011).

[95] CMS Collaboration, "Electron Identification Based on Simple Cuts." https://twiki.cern.ch/twiki/bin/viewauth/CMS/SimpleCutBasedEleIDanalysis (internal), (November 2011).

[96] CMS Collaboration, "Conversion Rejection." https://twiki.cern.ch/twiki/bin/viewauth/CMS/ConversionBackgroundRejection (November 2011).

[97] D. Barge et al., "Study of Photon Conversion Rejection at CMS", CMS Analysis Note AN 2009/159 (2009).

[98] CMS Collaboration, "Pileup Reweighting." https://twiki.cern.ch/twiki/bin/view/CMS/PileupReweighting (November 2011).

[99] CMS Collaboration, "Jet Resolution Determination at $\sqrt{s} = 7$ TeV", CMS Physics Analysis Summary JME-10-014 (2011).

[100] CMS Collaboration, "Measurement of b-tagging efficiency using $t\bar{t}$ events", CMS Physics Analysis Summary BTV-11-003 (2011).

[101] T. Chwalek, "Measurement of the W-Boson Helicity-Fractions in Top-Quark Decays with the CDF II Experiment and Prospects for an Early $t\bar{t}$ Cross-Section Measurement with the CMS Experiment", PhD Thesis, Karlsruhe Institute of Technology, IEKP-KA/2010-5 (2010).

[102] M. Feindt, "A Neural Bayesian Estimator for Conditional Probability Densities", arXiv:physics/0402093 (2004).

[103] M. Feindt and U. Kerzel, "The NeuroBayes neural network package", Nucl. Instrum. Meth. A559, 190–194 (2006).

[104] J. Lück, “Observation of Electroweak Single Top-Quark Production with the CDF II Experiment”, PhD Thesis, Karlsruhe Institute of Technology, IEKP-KA/2009-22 (2009).

[105] CMS Collaboration, “Jet Calibration and Resolution”, CMS Physics Analysis Summary JME-10-011 (2011).

[106] C. Böser, “Measurement of the charge asymmetry in top quark pair production at the CMS detector.”, Diploma Thesis, Karlsruhe Institute of Technology, IEKP-KA/2011-33 (2011).

Danksagung

Mein besonderer Dank gilt Prof. Dr. Thomas Müller für die Aufnahme in seine Arbeitsgruppe und die Möglichkeit schon während dieser Arbeit an Konferenzen teilnehmen zu können.

Für die Übernahme des Korreferats danke ich Prof. Dr. Michael Feindt.

Dr. Jeannine Wagner-Kuhr gilt mein besonderer Dank für die hervorragende Betreuung, die vielfältige Unterstützung und das Korrekturlesen dieser Arbeit.

Mein Dank gilt darüber hinaus meinem Kollegen Steffen Röcker, der sich viel Zeit genommen und mich in das Thema eingearbeitet hat. Dr. Thorsten Chwalek sowie Dr. Thomas Peiffer sei hiermit ein herzliches "Dankeschön" gewidmet für das intensive Korrekturlesen.

Ich möchte mich ebenfalls bei allen Mitgliedern der Top-Gruppe und des EKP bedanken, die jeden Tag dafür sorgen das die Arbeit so viel Spaß macht und so produktiv ist.

Meinen Eltern danke ich für ihre großzügige Unterstützung und ihr Vertrauen in mich. Sie haben mir das Studium ermöglicht und immer dafür gesorgt, dass ich mich ganz darauf konzentrieren konnte.

An alle Freunde, Bekannte, Studienkollegen und ganz besonders an meine Freundin: DANKE! Mit euch hat das Studieren erst so richtig Spaß gemacht.

Hiermit versichere ich, die vorliegende Arbeit selbstständig verfasst und nur die angegebenen Hilfsmittel verwendet zu haben.

Jens Hansen

Karlsruhe, den 15. März 2012